Three Dimensional Inverse Synthetic Aperture Radar Imaging

THESIS

Jack D. Pullis
Captain, USAF

AFIT/GE/ENG/95D-21

DEPARTMENT OF THE AIR FORCE

AIR UNIVERSITY

AIR FORCE INSTITUTE OF TECHNOLOGY

Wright-Patterson Air Force Base, Ohio

DTIC QUALITY INSPECTED 4

AFIT/GE/ENG/95D-21

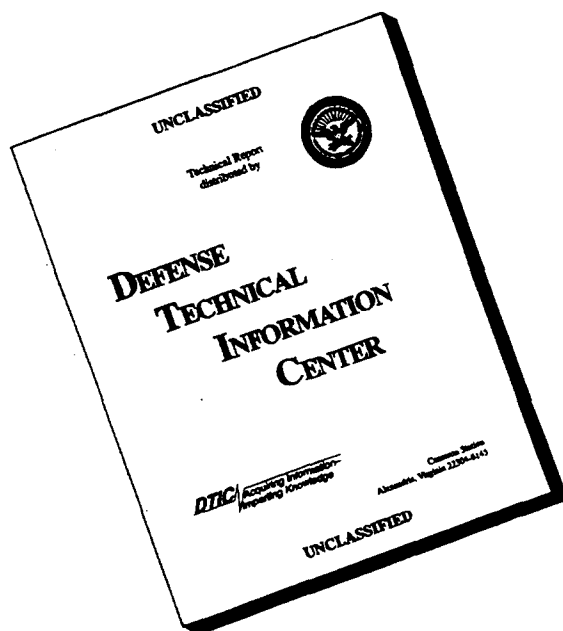Three Dimensional Inverse Synthetic Aperture Radar Imaging

THESIS

Jack D. Pullis
Captain, USAF

AFIT/GE/ENG/95D-21

19960617 010

DISCLAIMER NOTICE

UNCLASSIFIED

Technical Report
distributed by

DEFENSE
TECHNICAL
INFORMATION
CENTER

DTIC Acquiring Information-
Imparting Knowledge

Cameron Station
Alexandria, Virginia 22304-6145

UNCLASSIFIED

THIS DOCUMENT IS BEST
QUALITY AVAILABLE. THE
COPY FURNISHED TO DTIC
CONTAINED A SIGNIFICANT
NUMBER OF PAGES WHICH DO
NOT REPRODUCE LEGIBLY.

Three Dimensional Inverse Synthetic Aperture Radar Imaging

THESIS

Presented to the Faculty of the School of Engineering

of the Air Force Institute of Technology

Air University

In Partial Fulfillment of the

Requirements for the Degree of

Master of Science in Electrical Engineering

Jack D. Pullis, B.E. Electrical Engineering

Captain, USAF

December 1995

Acknowledgments

Table of Contents

List of Figures

List of Tables

Abstract

This research investigates the generation, display, and interpretation of three-dimensional (3-D) Synthetic Aperture Radar images. Three-dimensional assumes that the data collected consists of one temporal dimension and two orthogonal angular dimensions. From this data, a three dimensional reflectivity map, or 3-D image, of a target can be constructed. This reflectivity map can then be compared to the known structure of a target to gain more insight into the scattering mechanisms of the target. Until now research in this area has been limited to two-dimensional imaging. With the added third dimension, a more detailed target scattering map is possible.

First, a detailed review of radar imaging theory is conducted. This review starts with basic one-dimensional down-range profiles and Synthetic Aperture Radar theory. Two-dimensional imaging theory is then presented and developed through two-dimensional Filtered Back-Projection. This two-dimensional theory discussion is used as a stepping stone for the derivation of the three-dimensional Filtered Back-Projection algorithm. Finally, this algorithm is converted to a discretized algorithm for use on a computer.

This thesis effort applies this three-dimensional algorithm on actual radar data measured on an $\frac{1}{3}$ scale model of a C-29 aircraft. In the process of implementing this algorithm a few problems were encountered. Mainly, due to the vast quantity of data to be processed, the amount of memory available in terms of hard drive space as well as RAM became a limitation. Problems arose from the need to upsample the projection data in order to get sufficient image quality. Working within these memory constraints, three-dimensional images were produced.

The results demonstrate the ability to produce three-dimensional images given three-dimensional radar data. Two-dimensional slices of the three-dimensional image as well as three-dimensional isosurfaces are compared to the physical properties of the target.

Three Dimensional Inverse Synthetic Aperture Radar Imaging

I. Introduction

1.1 Problem

The United States Air Force is actively trying to develop technology to produce high resolution spatial maps from radar data taken on various targets. These maps can then be analyzed for target identification purposes. A couple of recent incidents reinforce the USAF's interest in this technology. Several years ago, the United States Navy accidently shot down an Iranian 747, mistaking it for a hostile fighter aircraft. More recently, the USAF shot down two United States Army Blackhawk helicopters mistaking them for much larger Iraqi Hind helicopters. The obvious structural differences between these mistaken identities and the actual targets could have been discerned had this radar technology been operationally available.

To this point, SAR imaging research has been limited to two-dimensions. With the added third-dimension, more information can be obtained about a target, ultimately allowing a more accurate target identification.

This research investigates the generation, display, and interpretation of three-dimension (3-D) Synthetic Aperture Radar images. Three-dimension assumes that the data collected consists of one temporal dimension and two orthogonal angular dimensions. From this data, a three dimensional reflectivity map, or 3-D image, of a target can be constructed.

Advanced radar ranges can collect and process data of this type efficiently. This research develops an efficient imaging algorithm to process this data. Also, since the resulting image is a function of three dimensions, methods to properly display the images, or slices of the images, will also be developed.

1.2 Radar Imaging Background

A thorough knowledge of the current two-dimensional (2-D) research is required in order to the develop an extension to 3-D. This summary provides an overview of past research done in this area.

1.2.1 Parametric Reconstruction Methods.

In many applications of computerized imaging, such as in electron microscopy, astronomy, geophysical exploration, non-destructive evaluation, and others, it is not possible to collect a complete set of angular-projections. Standard Fourier based reconstruction methods perform poorly in the case of limited projection data due to poor resolution. Parametric or iterative algorithms, on the other hand, are capable of producing high-quality images with limited data sets since they automatically take into account the missing data, as well as use a-priori information about the target (3).

The maximum likelihood method (MLM) of spectral estimation is one parametric method applied to the tomographic problem. This method has been found to provide high resolution, but does not exist for all data sets (11). Two-dimensional auto-regressive (AR) modeling algorithms also exist but have proved to be computationally expensive (6). The Prony method coupled with total least squares (TLS) has been used successfully to estimate frequencies from noisy data in one-dimension. This method was also extended to 2-D (11).

Delaney and Bressler (3) develop a series-expansion approach that is used in a fast and iterative tomographic reconstruction algorithm. This algorithm is applicable for parallel-ray projections that have been collected at a finite number of view angles. A conjugate gradient algorithm is used to minimize a regularized least-squares criterion. The main step in each iteration is equivalent to a 2-D discrete convolution, which can be cheaply and exactly implemented via the Fast Fourier Transform (FFT) (3).

These iterative or parametric techniques have been shown to have superior resolution capabilities but have also shown to be computationally expensive (2). This computational

2

cost is a major drawback since just one iteration typically requires more computation than an entire typical Fourier based method (3).

1.2.2   Fourier Reconstruction Methods.

In Fourier based methods, the radar returns from a target can be considered as a sample of the 2-D Fourier spectrum of the target's reflectivity. The imaging problem becomes one of reconstructing the spatial reflectivity of the target given these discrete samples of its Fourier spectrum (1).

One problem that arises in the use of Fourier based methods is that radar data is not usually collected in a uniform rectangular grid in the spectral domain since the rotation of the radar around the target introduces polar aspects. This property causes distortion if the standard 2-D Inverse Fast Fourier Transform (IFFT) is used to approximate the Fourier Transform, especially when data is obtained over large look angles. The 2-D IFFT is considered to yield the poorest results in terms of image quality, but is extremely fast computationally (1). In order to eliminate the distortion a focusing procedure must be used (8). A few focusing methods are now described.

1.2.2.1   Direct Focused Imaging.

Focused imaging utilizes a process which applies exact phase corrections to the sampled reflectivity data. Two direct focused methods are studied in (1); the first is simply an inverse Fourier transform from polar coordinates to rectangular coordinates. The second, originally derived by Mensa (8), is a similar method, but the phase correcting data points are not properly weighted in the final sum (1). This method still gives very accurate results, especially as the ratio of center frequency to bandwidth increases. The fact that an FFT algorithm cannot be used causes these direct focusing methods to be computationally expensive but provides the most accurate image possible.

3

Technique	Time (seconds)
Focused (both types)	552
Unfocused	1.74
Focused via Interpolation	2044
Filtered Back-projection	217

Table 1. Computational Speed of Imaging Techniques.

1.2.2.2 Focused Imaging via Interpolation.

In order to use the FFT to increase computational speed, the polar data is mapped onto a rectangular grid. This mapping is done by up-sampling the data set and then picking the closest data point to the required rectangular coordinates. This process obviously produces some inaccuracies and has been shown to be very computationally expensive (1).

1.2.2.3 Filtered Back-Projection.

An estimated image can be constructed by summing, or superimposing, 1-D projections from all available angles. This method unfortunately produces a blurred image. To correct this problem, a deblurring filter must be applied to the data. It is preferred in some applications to filter the projections prior to superimposing (8), but the filtering can be done on the spectral data prior to transforming it. Since both the frequency and spatial domain data are discrete in nature, the location of each individual image pixel may lie between available data points. This brings up the requirement for interpolation to produce a more accurate image. The filtered back-projection method has been shown to produce very accurate results while also being reasonable computationally (1). Table 1, taken from (1), compares computational speed of the focusing methods described above.

1.3 Approach/Methodology

Lewitt clearly explains the development of two-dimensional direct focus and filtered back-projection reconstruction algorithms in (7). In this research a three-dimensional reconstruction algorithm is developed using the same type of mathematical development. Due

4

to its computational efficiency This algorithm is a three-dimensional extension of the two-dimensional Filtered Back-Projection algorithm due to its computational efficiency . This algorithm is then applied to compact range data taken on a $\frac{1}{3}$ scale model of a C-29 aircraft, measured by Wright Laboratory. A suitable method for displaying the reconstructed three-dimensional data is then developed so that it can be visually compared to the actual physical properties of the aircraft.

1.4 Summary of Chapters

Chapter 2 covers imaging theory from its fundamentals through a detailed development of three-dimensional imaging. Finally a discretized algorithm is developed. The actual application of the theory is discussed in Chapter 3. The target used is described as well as the measured data sets. The methodology of producing the actual images found in this research is also discussed. Three dimensional images as well as two-dimensional slices are included in Chapter 4. These results are explained and compared to the actual target. Chapter 5 contains conclusions drawn from the research and recommendations for future work.

II. Radar Imaging Theory

2.1 Introduction

In this chapter radar imaging is presented, starting with its basic principles through two-dimensional Filtered Back-Projection. This two-dimensional mathematical basis is then extended to a three-dimensional Filtered Back-Projection algorithm. Finally, this three-dimensional algorithm is then discretized for use on a computer.

2.2 Two Dimensional Radar Imaging

Radar sensors respond to electro-magnetic waves which are scattered when the propagation of incident waves is disturbed by the presence of an object (8). When an object such as an aircraft is interrogated by a radar, certain features such as wing tips and engines produce "hot spots" or scattering centers where most of the return energy is radiated from. A spatial map of these scattering centers would reveal the physical properties of the object. This spatial distribution of reflectivity corresponding to an object is known as a radar image (8).

In order to produce a good quality radar image, a high degree of both downrange and crossrange or azimuthal resolution must be achieved. Figure 1 illustrates the definitions of downrange and crossrange. Downrange location is determined by measuring the time delay between time markers in the transmitted waveform and the received waveform. In pulse radar systems, these time markers are the leading and trailing edges of the pulse. The round trip delay , τ, for a target at range, R, where c is the propagation velocity is

$$\tau = \frac{2R}{c}.$$
(1)

So in order to distinguish between two points separated by a distance ΔR, you will need a pulse width of less than T such that

$$T = \frac{2\Delta R}{c}.$$
(2)
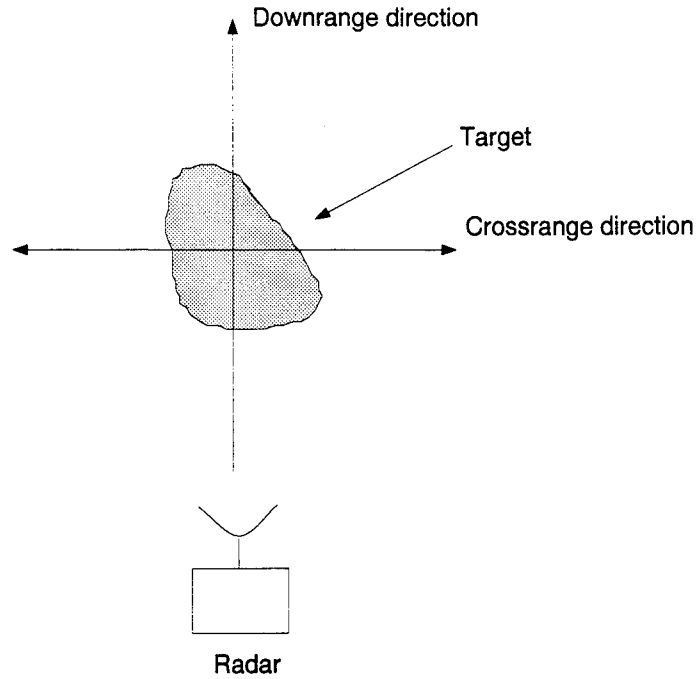
Figure 1. Definition of Crossrange and Downrange.

This Equation can also be written as

$$\Delta R = \frac{cT}{2} \qquad (3)$$

or

$$\Delta R = \frac{c}{2B} \qquad (4)$$

where, $B = \frac{1}{T}$, is the system bandwidth as defined in Figure 2. It can be seen that as the system bandwidth increases, the resolution becomes finer, with the best resolution occurring at infinite bandwidth or when the pulse is an impulse in time. So in order to get a high degree of downrange resolution directly it would be necessary to transmit the entire bandwidth of frequencies simultaneously such as in an Impulse Radar. This would prove to be extremely difficult if not impossible. Luckily, the same results can be achieved synthetically by making several narrowband measurements at discrete frequency increments, as shown in Figure 2.
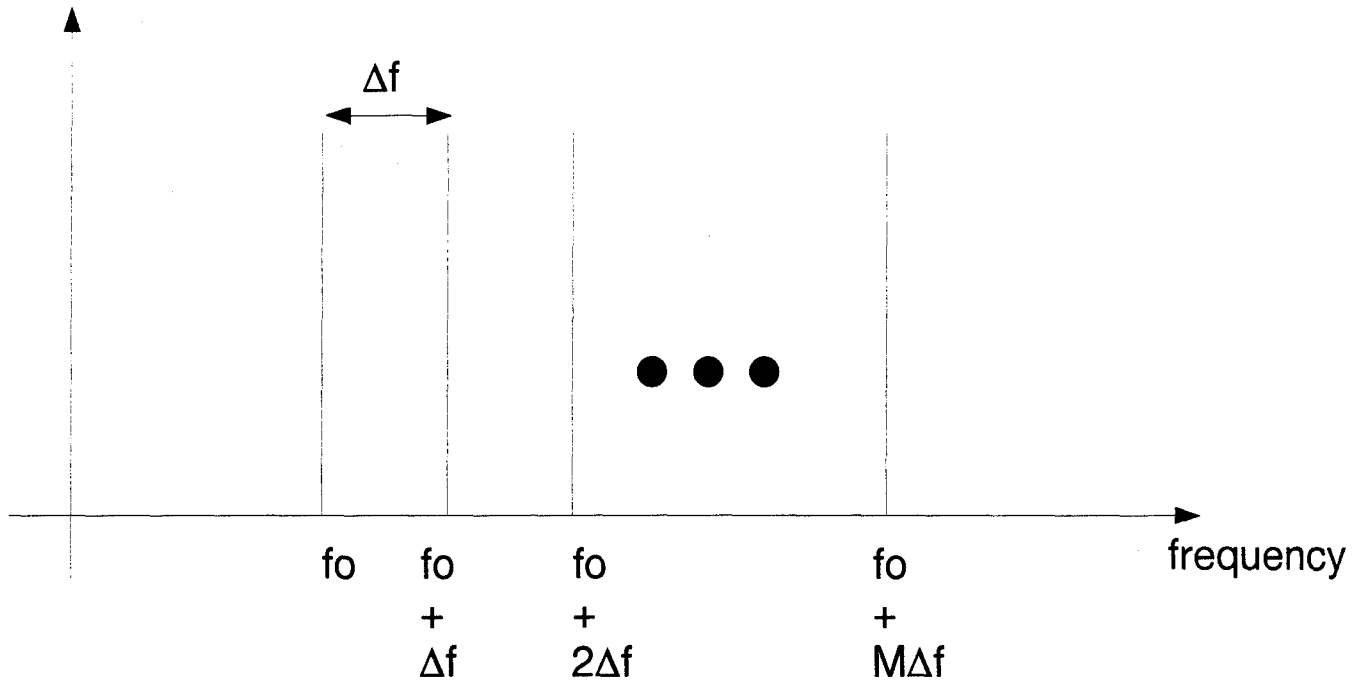
Figure 2. Sampled Frequency Spectrum, $B = M\Delta f$, 1-D imaging.

Combining all these narrowband responses will provide the same range resolution as if the entire frequency band was transmitted simultaneously (8).

Next, considering the crossrange dimension, the radar aperture must be increased in size in order to improve azimuth resolution, Δx, as shown in Equation 5,

$$\Delta x \simeq \frac{\lambda}{2\Theta} = \frac{c}{2 f_c \Theta} \tag{5}$$

where Θ is the total radian angular aperture and $f_c = f_0 + \frac{M}{2} \delta f$ as defined in Figure 2.

Physically increasing aperture size can lead to the need for extremely large antennas. A more favorable method for our purposes is to develop a synthetic aperture by sequentially transmitting and receiving at discrete points along a circular path to vary the viewing angle. The received signals are coherently summed together to produce signals equivalent to those that would be received by the physical aperture as shown in Figure 3 (8).

8
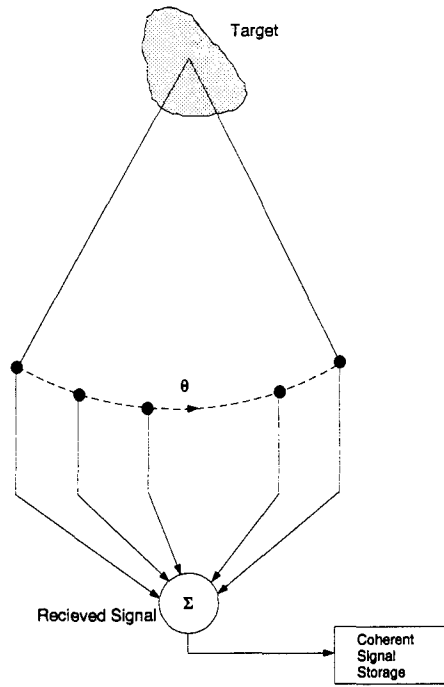
Figure 3. Synthetic Aperture Formation, spotlight mode SAR.

Synthetic Aperture Radar (SAR) utilizes both a synthetically expanded bandwidth as well as the synthetic aperture process explained above. SAR is utilized in many ways but this research is focused on spotlight Inverse Synthetic Aperture Radar (ISAR), in which the radar is stationary with the antenna fixed on the target, while the viewing angle is changed by rotating the target on a pedestal. It is also assumed that the radar sensor uniformly irradiates the entire object as shown in Figure 4.

As stated earlier, a radar image can be looked at as the sum of the target's scattering centers which can be represented by the function $f(x, y)$. Our goal is to determine the locations of these scattering centers from our reflected radar signals by producing an image.

First we will define our geometry. As can be seen in Figure 4, the x and y axis are fixed with respect to the target while the u and v axis are the cross range and down range respectively with respect to the radar. For a fixed Θ, the received signal for a certain down range point v will be the integral of the reflectivity density over u, assuming that all reflection
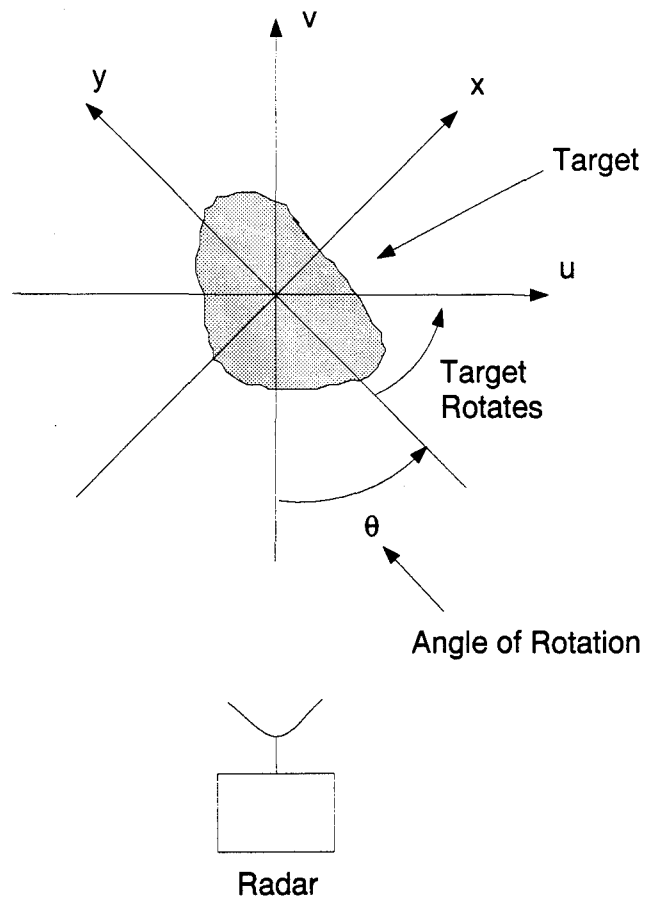
Figure 4. ISAR geometry.

coefficients have equal phase components. Note that $p(v; \Theta)$ in Equation 6 can be looked upon as a projection of the reflectivity on the v axis at the look angle Θ.

$$p(v; \Theta) \propto \int_{-\infty}^{\infty} f_\Theta(u, v) du \qquad (6)$$

where

$$f_\Theta(u, v) = f(x, y)$$

and

$$\begin{bmatrix} u \\ v \end{bmatrix} = \begin{bmatrix} cos\Theta & -sin\Theta \\ sin\Theta & cos\Theta \end{bmatrix} \begin{bmatrix} x \\ y \end{bmatrix} \qquad (7)$$

10
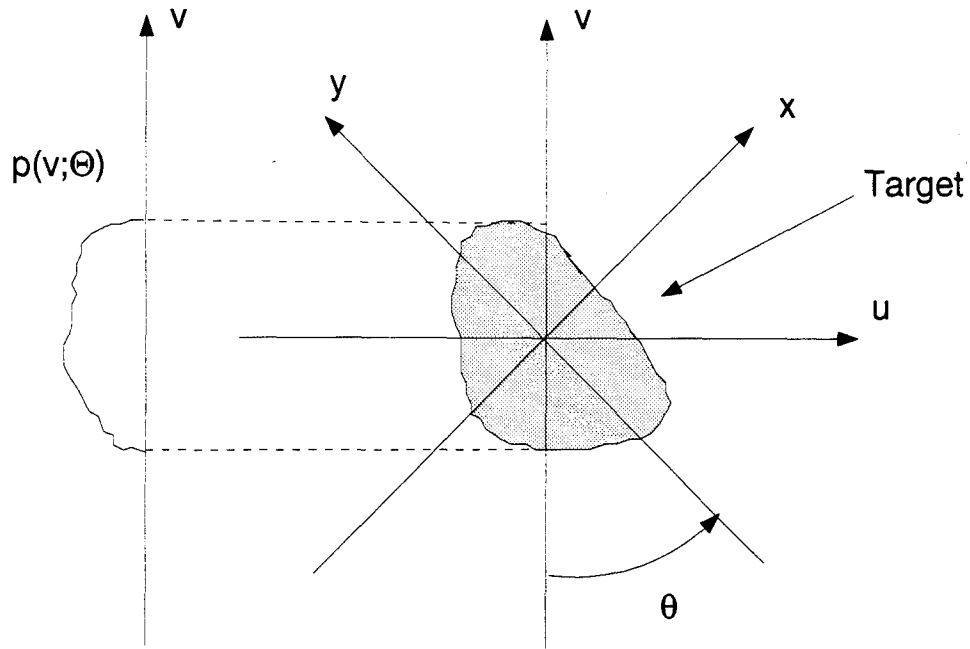
Figure 5. Radar projection.

The total received signal at a certain look angle and frequency, $F(f, \Theta)$, will be the line integral of $p(v; \Theta)$ along v with a correcting round trip phase factor. Thus

$$F(f, \Theta) = \int_{-\infty}^{\infty} p(v; \Theta) e^{-\frac{i4\pi v}{\lambda}} dv = \int_{-\infty}^{\infty} p(v; \Theta) e^{-\frac{i4\pi v f}{c}} dv. \tag{8}$$

Substituting Equation 6 into Equation 8 we obtain

$$F(f, \Theta) = \int_{-\infty}^{\infty} \int_{-\infty}^{\infty} f_{\Theta}(u, v) e^{-\frac{i4\pi v f}{c}} du dv \tag{9}$$

Since from Equation 7, $v = x \sin \Theta + y \cos \Theta$, $F(f, \Theta)$ can be expressed as

$$F(f, \Theta) = \int_{-\infty}^{\infty} \int_{-\infty}^{\infty} f(x, y) e^{-\frac{i4\pi f}{c}(x \sin \Theta + y \cos \Theta)} dx dy \tag{10}$$

now defining

$$f_x \stackrel{\triangle}{=} f \sin \Theta \tag{11}$$

11

and

$$f_y \stackrel{\triangle}{=} f \cos \Theta \tag{12}$$

$F(f, \Theta)$ can be rewritten as

$$F_r(f_x, f_y) = \int_{-\infty}^{\infty} \int_{-\infty}^{\infty} f(x, y) e^{-\frac{i4\pi}{c}(f_x x + f_y y)} dx dy \tag{13}$$

where $F_r(f_x, f_y)$ is $F(f, \Theta)$ expressed in rectangular coordinates. Equation 13 is recognized as the two-dimensional Fourier transform. Due to the properties of the 2-D Fourier transform we can write (4)

$$f(x, y) \stackrel{\substack{2\text{-D} \\ \text{F.T.}}}{\Longleftrightarrow} F_r(f_x, f_y) \tag{14}$$

where $\stackrel{\substack{2\text{-D} \\ \text{F.T.}}}{\Longleftrightarrow}$ denotes a 2-D Fourier transform pair. The inverse 2-D Fourier transform of Equation 13 is given by

$$f(x, y) = \int_{-\infty}^{\infty} \int_{-\infty}^{\infty} F_r(f_x, f_y) e^{\frac{i4\pi}{c}(f_x x + f_y y)} df_x df_y \tag{15}$$

Thus, this equation establishes how a 2-D image is formed.

In ISAR, as we defined it in Figure 4, the radar data is not collected on a uniform rectangular grid since the rotation of the target introduces polar aspects. This property would result in a distorted or "unfocused" image if the standard Inverse Fourier Transform is used, especially when data is collected over large look angles. In order to eliminate this distortion we must convert the frequency domain into polar coordinates as shown in Figure 6. This conversion is implemented by substituting Equations 11 and 12 into Equation 15 as well as letting

$$df_x df_y = f df d\Theta \tag{16}$$

we obtain

$$f(x, y) = \int_0^{2\pi} \int_0^{\infty} F(f, \Theta) e^{\frac{i4\pi f}{c}(x \sin \Theta + y \cos \Theta)} f df d\Theta. \tag{17}$$

12

Figure 6. Spatial frequency coordinates.

This can also be written as

$$f(x, y) = \int_0^\pi \int_0^\infty F(f, \Theta) e^{\frac{i4\pi f}{c}(x \sin \Theta + y \cos \Theta)} f \, df \, d\Theta +$$
$$\int_0^\pi \int_0^\infty F(f, \Theta + \pi) e^{\frac{i4\pi f}{c}(x \sin(\Theta + \pi) + y \cos(\Theta + \pi))} f \, df \, d\Theta \qquad (18)$$

and since for isotropic scatterers

$$F(f, \Theta + \pi) = F(-f, \Theta)$$
$$\cos(\Theta + \pi) = -\cos(\Theta) \qquad (19)$$
$$\sin(\Theta + \pi) = -\sin(\Theta)$$

Equation 17 can be rewritten as

$$f(x, y) = \int_0^\pi \int_{-\infty}^\infty F(f, \Theta) e^{\frac{i4\pi f}{c}(x \sin \Theta + y \cos \Theta)} |f| \, df \, d\Theta. \qquad (20)$$
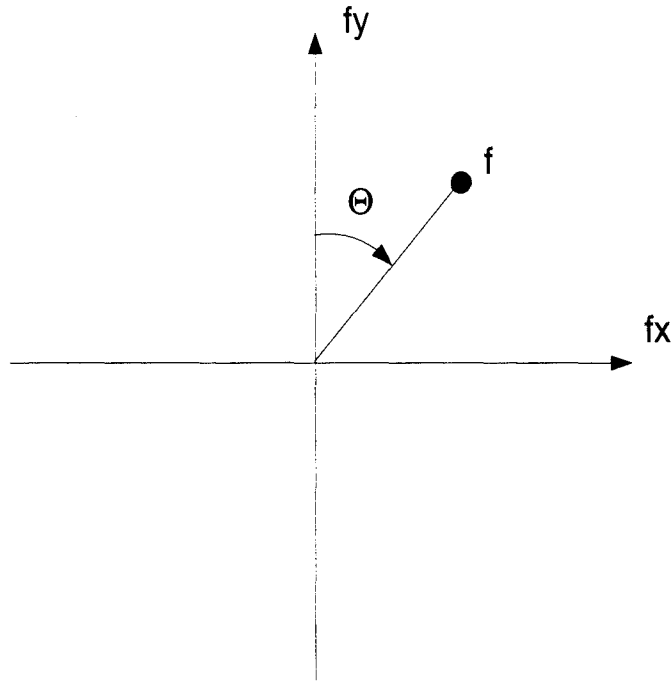
13

Equation 20 produces a "focused" reconstruction of the target. However since the standard rectangular coordinate system is not used the data is not compatible with a 2-D Fast Fourier Transform (FFT) algorithm. This makes computing a "focused" image as shown in Equation 20 much more computationally expensive than producing an "unfocused" image (1).

In order to increase computational speed it is also possible to construct a "focused" image by summing, or superimposing one dimensional projections from all available angles (8). This allows the use of the one dimensional Inverse Fourier Transform as follows. It can be seen in Equation 6 that the total received signal at a certain look angle is also the one-dimensional Fourier Transform of the projection $p(v; \Theta)$ at that look angle. So, rewriting Equation 20 as

$$f(x,y) = \int_0^\pi \left[\int_{-\infty}^\infty F(f,\Theta)e^{\frac{i4\pi f}{c}(x\sin\Theta + y\cos\Theta)}|f|df \right] d\Theta \qquad (21)$$

it can be seen that the bracketed expression is a one dimensional Fourier transform of the total received signal at a fixed look angle Θ, multiplied by a filtering term $|f|$. Let's now call this the filtered projection $\tilde{p}(v, \Theta)$,

$$\tilde{p}(v,\Theta) = \int_{-\infty}^\infty F(f,\Theta)e^{\frac{i4\pi v f}{c}}|f|df \qquad (22)$$

where $v = x\sin\Theta + y\cos\Theta$. Substituting Equation 22 into Equation 21 we obtain

$$f(x,y) = \int_0^\pi \tilde{p}(v,\Theta)d\Theta. \qquad (23)$$

Equation 23 is known as the Filtered Back-Projection method of imaging and can utilize a one dimensional IFFT algorithm to compute the projections. This greatly increases computational speed (1) while also produces a "focused" image.

14

2.3 Three Dimensional Radar Imaging

Up to this point all discussion has been confined to two dimensions in an effort to develop a mathematical basis for three dimensional imaging. In order to obtain elevation resolution the target must also be rotated in a plane orthogonal to the azimuthal rotation as shown in Figure 7.
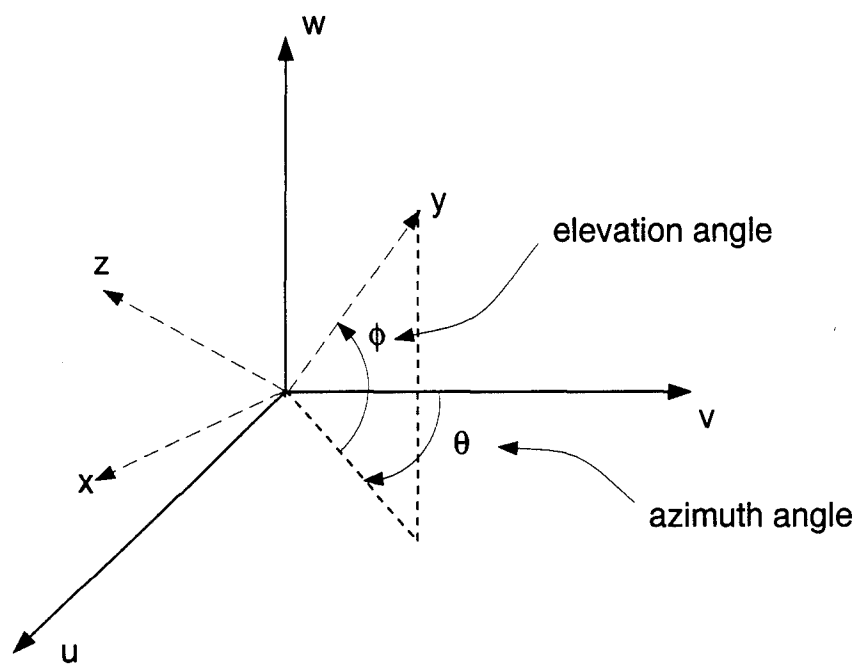
Figure 7. Three dimensional geometry.

Again the u, v, and w axes are fixed in relation to the radar while the x, y, and z axes are fixed in relation to the target such that when $\Theta = \phi = 0$ the x axis is equivalent to the u axis, the y axis is equivalent to the v axis, and the z axis is equivalent to the w axis. Figure 8 shows the radar configuration at the $\Theta = \phi = 0$ look angle.

Assuming that the Fourier transform relation holds in three dimensions

$$f(x, y, z) \overset{\underset{\mathrm{3\text{-}D}}{\mathrm{F.T.}}}{\Longleftrightarrow} F_r(f_x, f_y, f_z) \tag{24}$$

we can say

15
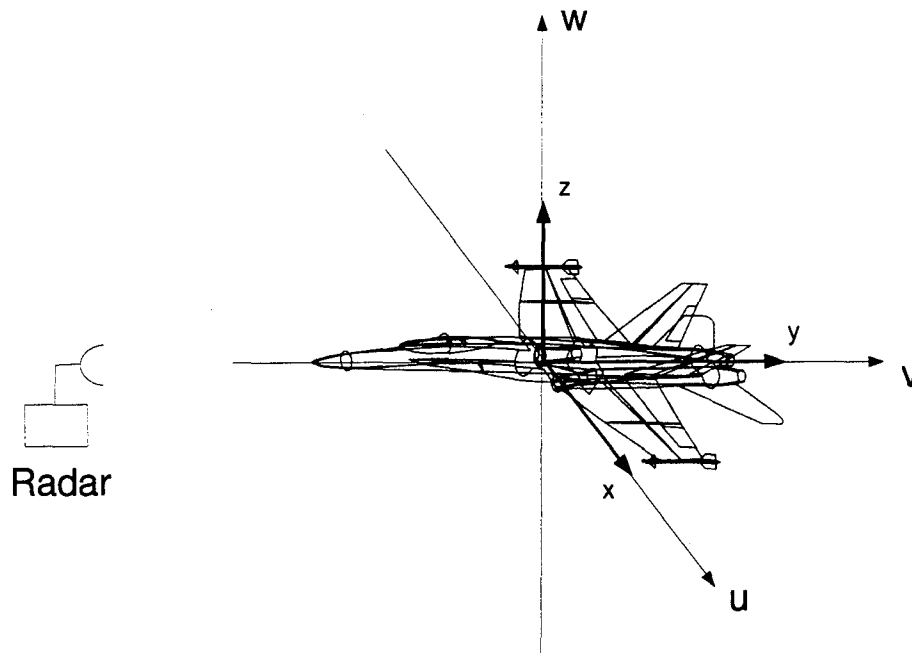
Figure 8. ISAR configuration at $\Theta = \phi = 0$.

$$f(x, y, z) = \int_{-\infty}^{\infty} \int_{-\infty}^{\infty} \int_{-\infty}^{\infty} F_r(f_x, f_y, f_z) e^{\frac{i4\pi}{c}(f_x x + f_y y + f_z z)} df_x df_y df_z. \qquad (25)$$

Again as can be seen in Figure 7, the spherical coordinate system is more suitable than rectangular coordinates for this geometry. Converting Equation 25 to spherical coordinates by the following relations obtained from Figures 9 and 10

$$
\begin{aligned}
f_x &= f \sin \Theta \cos \phi \\
f_y &= f \cos \Theta \cos \phi \\
f_z &= f \sin \phi \\
df_x df_y df_z &= f^2 \cos \phi \, df \, d\Theta \, d\phi
\end{aligned}
\qquad (26)
$$

yields

16

Figure 9. Spatial frequency coordinates in three dimensions.
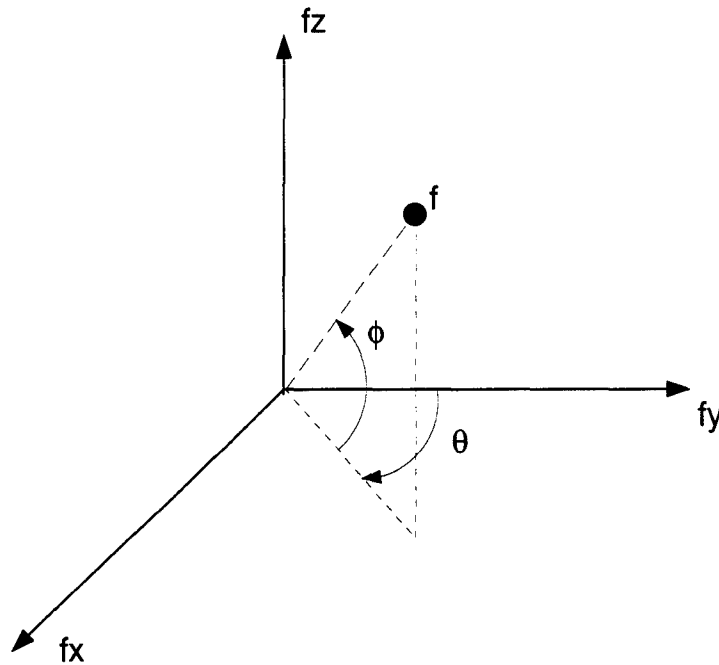
$$f(x,y,z) = \int_{-\pi}^{\pi} \int_{0}^{2\pi} \int_{0}^{\infty} F(f,\Theta,\phi) e^{\frac{i4\pi f}{c}(x\sin\Theta\cos\phi + y\cos\Theta\cos\phi + z\sin\phi)} f^2 \cos\phi \, df \, d\Theta \, d\phi.$$

(27)

A similar process used to transform Equation 17 into 20 will transform Equation 27 into

$$f(x,y,z) = \int_{-\pi}^{\pi} \int_{0}^{\pi} \int_{-\infty}^{\infty} F(f,\Theta,\phi) e^{\frac{i4\pi f}{c}(x\sin\Theta\cos\phi + y\cos\Theta\cos\phi + z\sin\phi)} f^2 \cos\phi \, df \, d\Theta \, d\phi.$$

(28)

Again, to obtain the Filtered Back-Projection Equation we rewrite Equation 28 as

$$f(x,y,z) = \int_{-\pi}^{\pi} \int_{0}^{\pi} \left[\int_{-\infty}^{\infty} F(f,\Theta,\phi) e^{\frac{i4\pi f}{c}(x\sin\Theta\cos\phi + y\cos\Theta\cos\phi + z\sin\phi)} f^2 \cos\phi \, df \right] d\Theta \, d\phi.$$

(29)

In this case the bracketed expression is also a one dimensional Fourier transform at a fixed azimuth angle Θ and elevation angle ϕ, multiplied by a filtering term, $f^2 \cos\phi$. This will be
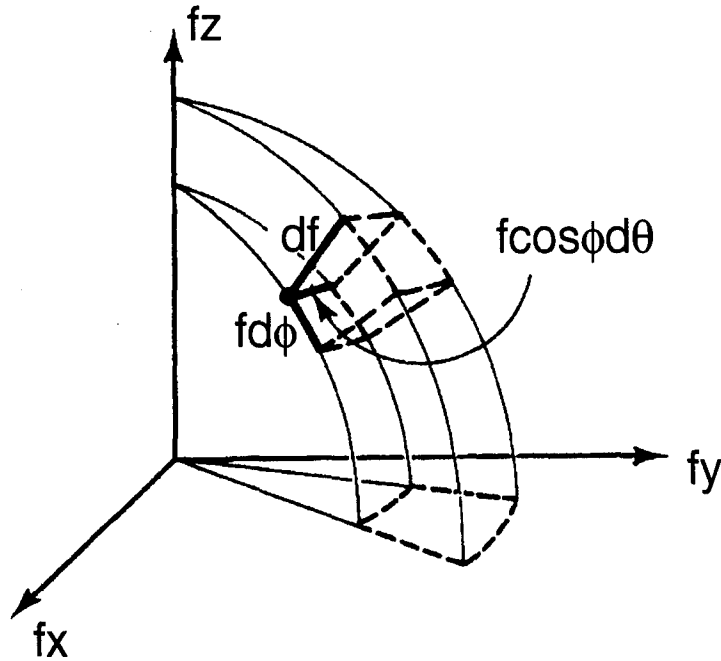
17

Figure 10. $df_x df_y df_z = f^2 \cos \phi df d\Theta d\phi$.

called a filtered projection

$$\tilde{p}(v, \Theta, \phi) = \int_{-\infty}^{\infty} F(f, \Theta, \phi) e^{\frac{i4\pi vf}{c}} f^2 \cos \phi df \qquad (30)$$

where $v = x \sin \Theta \cos \phi + y \cos \Theta \cos \phi + z \sin \phi$. Substituting Equation 30 into Equation 29 yields

$$f(x, y, z) = \int_{-\pi}^{\pi} \int_{0}^{\pi} \tilde{p}(v, \Theta, \phi) d\Theta d\phi. \qquad (31)$$

Equation 31 is known as Filtered Back-Projection in three dimensions. It is this equation that will be utilized in the formation of three dimensional images in this research. But in practical applications is is impossible to obtain an infinite bandwidth. Therefore, a band limited version of Equation 30 with frequencies ranging from f_0 through f_M is

18

$$\tilde{p}_{bl}(v, \Theta, \phi) = \int_{f_0}^{f_M} F(f, \Theta, \phi) e^{\frac{i4\pi vf}{c}} f^2 \cos \phi \, df. \tag{32}$$

It is also uncommon to have a complete set of projections from every angle so limiting Equation 31 to azimuth angles from Θ_0 through Θ_N and elevation angles from ϕ_0 through ϕ_L gives

$$f_{bl}(x, y, z) = \int_{\phi_0}^{\phi_L} \int_{\Theta_0}^{\Theta_N} \tilde{p}_{bl}(v, \Theta, \phi) \, d\Theta \, d\phi. \tag{33}$$

2.4 Discretized Three-Dimensional Algorithm

In order to implement this algorithm on a computer, a discrete version must be developed. The continuous time version already derived can be sampled at discrete angles Θ_n, $0 \le n \le N$ and ϕ_m, $0 \le m \le M$ as well as using a sampled frequency spectrum as shown in Figure 2. But inherently, when a signal is sampled in the frequency domain, aliasing occurs in the time domain (9). In the downrange direction Δf must be chosen such that the downrange unambiguous range, R_{ux},

$$R_{ux} = \frac{c}{2\Delta f} \tag{34}$$

is at least as large as the downrange extent of the target. The angular steps, $\Delta \Theta$ and $\Delta \phi$ must also be chosen such that the unambiguous range in the crossrange, R_{uy}, and vertical direction, R_{uz},

$$R_{uy} = \frac{c}{2f_c \Delta \Theta} \tag{35}$$

$$R_{uz} = \frac{c}{2f_c \Delta \phi} \tag{36}$$

are also greater than the size of the target in those directions.

19

Using the trapezoidal rule (5) to discretize the filtered projection from Equation 32 we obtain

$$\tilde{p}_d(v_k, \Theta_n, \phi_m) = \Delta f \sum_{l=0}^{L} F(f_l, \Theta_n, \phi_m) e^{\frac{j4\pi v_k f_l}{c}} f_l^2 \cos \phi_m. \tag{37}$$

Equation 37 can be recognized as an IFFT which can be easily implemented using available software.

In a discretized version of Equation 33, values must be computed for each for each x_q, y_r, z_s pixel such that $0 \leq q \leq Q$, $0 \leq r \leq R$, and $0 \leq s \leq S$. Since v_k is also discrete it is unlikely that the required equation

$$v_k = x_q \sin \Theta_n \cos \phi_m + y_r \cos \Theta_n \cos \phi_m + z_r \sin \phi_m \tag{38}$$

will hold exactly, but rather the value will fall between two values such as v_k and v_{k+1}. Therefore, in order to obtain a value for $\tilde{p}_d$ a linear interpolation scheme must be used. The method used in this research is as follows. Letting

$$v_a = x_q \sin \Theta_n \cos \phi_m + y_r \cos \Theta_n \cos \phi_m + z_r \sin \phi_m \tag{39}$$

then,

$$\tilde{p}_i(v_a, \Theta_n, \phi_m) = \frac{|v_a - v_k|}{|v_{k+1} - v_k|} \tilde{p}_d(v_k, \Theta_n, \phi_m) + \frac{|v_{k+1} - v_a|}{|v_{k+1} - v_k|} \tilde{p}_d(v_{k+1}, \Theta_n, \phi_m) \tag{40}$$

so each x_q, y_r, z_s pixel is computed as

$$\tilde{f}_{bl}(x_q, y_r, z_s) = \Delta\Theta\Delta\phi \sum_{n=0}^{N} \sum_{l=0}^{M} \tilde{p}_i(v_a, \Theta_n, \phi_m). \tag{41}$$

2.5 Conclusion

In this chapter radar imaging was presented from its basic principles through two-dimensional Filtered Back-Projection. This two-dimensional mathematical basis was then extended to a three-dimensional Filtered Back-Projection algorithm. Then, the three-dimensional

algorithm was discretized for use on a computer. The algorithm derived in this chapter is applied to actual radar data in the next chapter.

III. Application and Methodology

3.1   Introduction

In this chapter the target and radar data used to test the algorithm of Chapter 2 is presented. Then, the methods used to generate results are explained as are the obstacles encountered during the implementation of these methods.

3.2   The Target

In order to test the algorithm developed in Chapter 2, three-dimensional radar measurements were made on an $\frac{1}{3}$ scale model of a C-29 aircraft in a Wright Laboratory compact range. This model was accurate in every detail when compared to the actual aircraft except they put a reflective metallic film on the windscreen in order to block reflections from the cockpit. Photographs and scale drawings of the model are shown in Figures 11 and 12.

3.3   The Data

Two series of radar measurements were taken on this target. One series was taken with azimuth angles equaling $-5° \leq \Theta \leq 5°$ with step size $\Delta\Theta = 0.04°$, elevation angles equaling $3° \leq \phi \leq 7°$ with step size $\Delta\phi = 0.04°$, and frequencies equaling $26\ \text{Ghz} \leq f \leq 36\ \text{Ghz}$ with step size $\Delta f = 10\ \text{Mhz}$. The transmit and receive polarizations were both vertical for these measurements. This data set will be referred to as " the nose data". Figure 13 illustrates this geometry.

The second series used the same elevation angles and frequencies as the first series, but the azimuth angles equaled $-19° \leq \Theta \leq 29°$ with step size $\Delta\Theta = 0.04°$. The transmit and receive polarizations were both horizontal for these measurements. This data set will be referred to as " the wing data". Figure 14 illustrates this geometry.

Both data sets have the same unambiguous ranges as follows;

$$R_{ux} = \frac{c}{2f_c\Delta\Theta} = \frac{3\times10^8}{2(31\times10^9)(0.04\times\frac{\pi}{180})} = 6.93 \text{ meters}$$

$$R_{uy} = \frac{c}{2\Delta f} = \frac{3\times10^8}{2(10\times10^6)} = 15 \text{ meters} \tag{42}$$

$$R_{uz} = \frac{c}{2f_c\Delta\phi} = \frac{3\times10^8}{2(31\times10^9)(0.04\times\frac{\pi}{180})} = 6.93 \text{ meters}$$

and theoretically provide resolutions of,

$$\Delta R_x = \frac{c}{2f_c\Delta\Theta} = \frac{3\times10^8}{2(31\times10^9)(10.0\times\frac{\pi}{180})} = 0.0277 \text{ meters}$$

$$\Delta R_y = \frac{c}{2B} = \frac{3\times10^8}{2(10\times10^9)} = 0.015 \text{ meters} \tag{43}$$

$$\Delta R_z = \frac{c}{2f_c\Delta\phi} = \frac{3\times10^8}{2(31\times10^9)(4.0\times\frac{\pi}{180})} = 0.0693 \text{ meters.}$$

3.4 The Approach

The measured data or "raw data" is the $F_p(f_l, \Theta_n, \phi_m)$ in Equation 37 and as expected the data files are very large at 203.6 megabytes each. The first step in making an image is computing the filtered projections, $\tilde{p}_d$. This was accomplished using the Matlab programming language developed by Math Works Inc., due to its ability to quickly perform matrix computations.

Unfortunately, in spite of Equation 43, it was found to be necessary to up sample the data when computing the IFFT in order to get sufficient resolution in the resulting image. This is a result of accumulated error from summing the numerous projections. This caused a large increase in data size which required a trade-off between image resolution and usable disk space. The process of up sampling essentially provides additional interpolated projection values between the originals, providing more accurate approximations when summing the projections to compute a pixel value. It was determined, by trial and error, that a six times up sample for the nose data and a seven times up sample for the wing data proved sufficient to provide an accurate image. In order to demonstrate the importance of up sampling Figure 15 shows no up sampling, 6 times up sampling, and 20 times up sampling on one elevation two-dimensional images using the nose data. It is seen that image quality decreases radically as the up sampling factor drops with the case of no up sampling resulting in a useless image.

However, the limited hard drive space available for this research resulted in the need for additional data reduction. Since the target is only 5.2 meters in length and the unambiguous range, R_{uy}, is 15 meters, a 50% data reduction is allowed by only requiring the use of every other frequency sample. Similarly, since the target is 1.79 meters long in the z direction a $\Delta\phi = 0.08°$ still allows an unambiguous range greater than the extent of the target in that direction as shown in Equation 44.

$$R_{uz} = \frac{3 \times 10^8}{2(31 \times 10^9)(0.08 \times \frac{\pi}{180})} = 3.47 \text{ meters} \tag{44}$$

This fact permits an additional 50% data reduction by making it necessary to only use the data from every other elevation angle. The 50 filtered projection files, one for each of the elevation angles between $\phi = 3°$ and $\phi = 7°$ would take up approximately 605 megabytes of storage space for the nose data and 705 megabytes for the wing data. These figures are still beyond that which was available for the generation of this research, so only 37 of the elevation angles between $\phi = 3°$ and $\phi = 5.88°$ were used. This resulted in an acceptable new z direction resolution of,

$$\Delta R_z = \frac{3 \times 10^8}{2(31 \times 10^9)(2.88 \times \frac{\pi}{180})} = 0.0963 \text{ meters}. \tag{45}$$

Once the filtered projection files were produced, this data was transformed, using Fortran 77 code, to one large three-dimensional array according to f, Θ, and ϕ and restored as an unformatted binary 223.3 megabyte file for the nose data and a 260.6 megabyte file for the wing data. The use of one large file enables a great increase in computational speed by allowing all the data to be loaded into resident memory under one variable, so the calculations of summing and interpolation in equations 40 and 41 can be done efficiently. If enough resident memory is available to hold the filtered projection data as well as the additional variables to perform the calculations, an individual x,y,z pixel can be computed in 0.15 seconds on a Sun Microsystems SPARC 2 workstation. This number greatly suffers if insufficient resident memory is available.

After all the pixels are computed a method of displaying the image is needed. Two methods were used in this research. Two-dimensional slices were made from the three-dimensional data set using Matlab to show the locations of the major scatterers and compare them to the actual target. Also, IDL, developed by Research Systems, Inc., has a useful volume visualization tool called SLICER. This application was used to produce iso-surfaces or three-dimensional contour plots of a volume at a given density level. For example, in medical imaging applications, a series of two-dimensional images can be created by computed tomography or magnetic resonance imaging. When stacked, these images create a grid of density measurements that can be contoured to display the surface of anatomical structures (10). IDL also was used to visualize slices of the the volume data set.

3.5 Conclusion

In this chapter the $\frac{1}{3}$ scale model of the C-29 and the two series of radar measurements used to test the algorithm of Chapter 2 were presented. Then, the methods used to generate results were explained as was the obstacles encountered during the implementation of those methods.
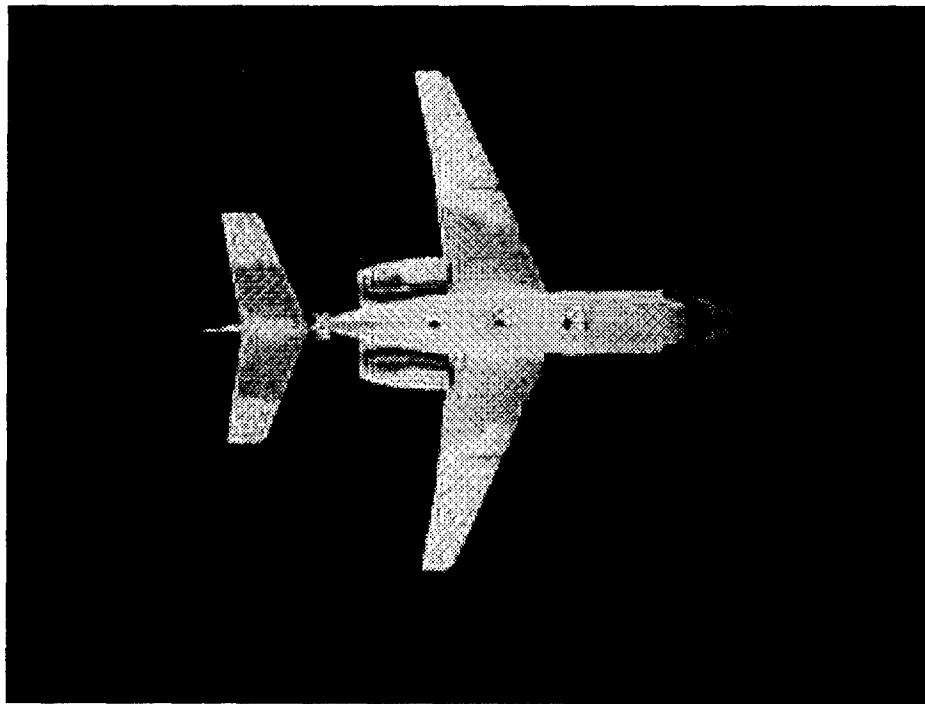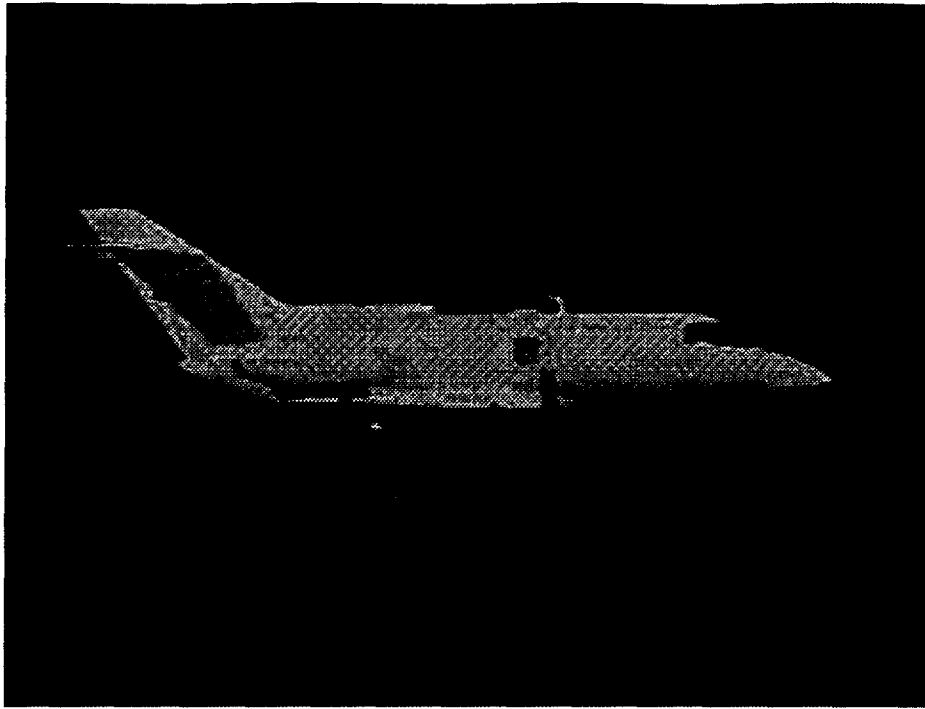
Figure 11. Photographs of C-29 $\frac{1}{3}$ Scale Model.

26

5.2 meters

5.2 meters

1.79 meters
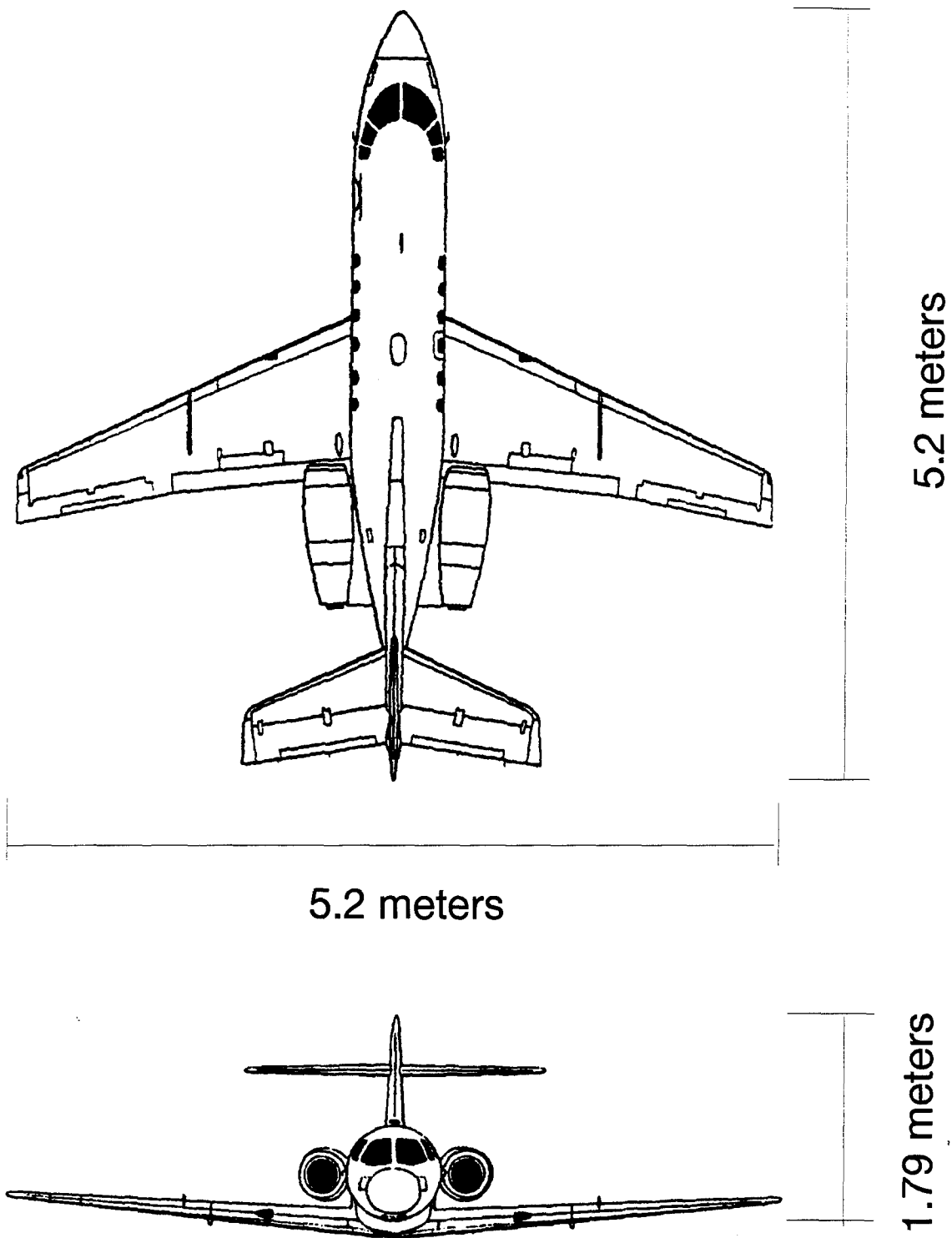
Figure 12. $\frac{1}{3}$ Scale Dimensions of a C-29.

VV Polarization		
Azimuth Angle	$-5° \leq \Theta \leq 5°$	$\Delta\Theta = 0.04°$
Elevation Angle	$3° \leq \phi \leq 7°$	$\Delta\phi = 0.04°$
Frequencies	26×10^9 hertz $\leq f \leq 36 \times 10^9$ hertz	$\Delta f = 10 \times 10^6$ hertz
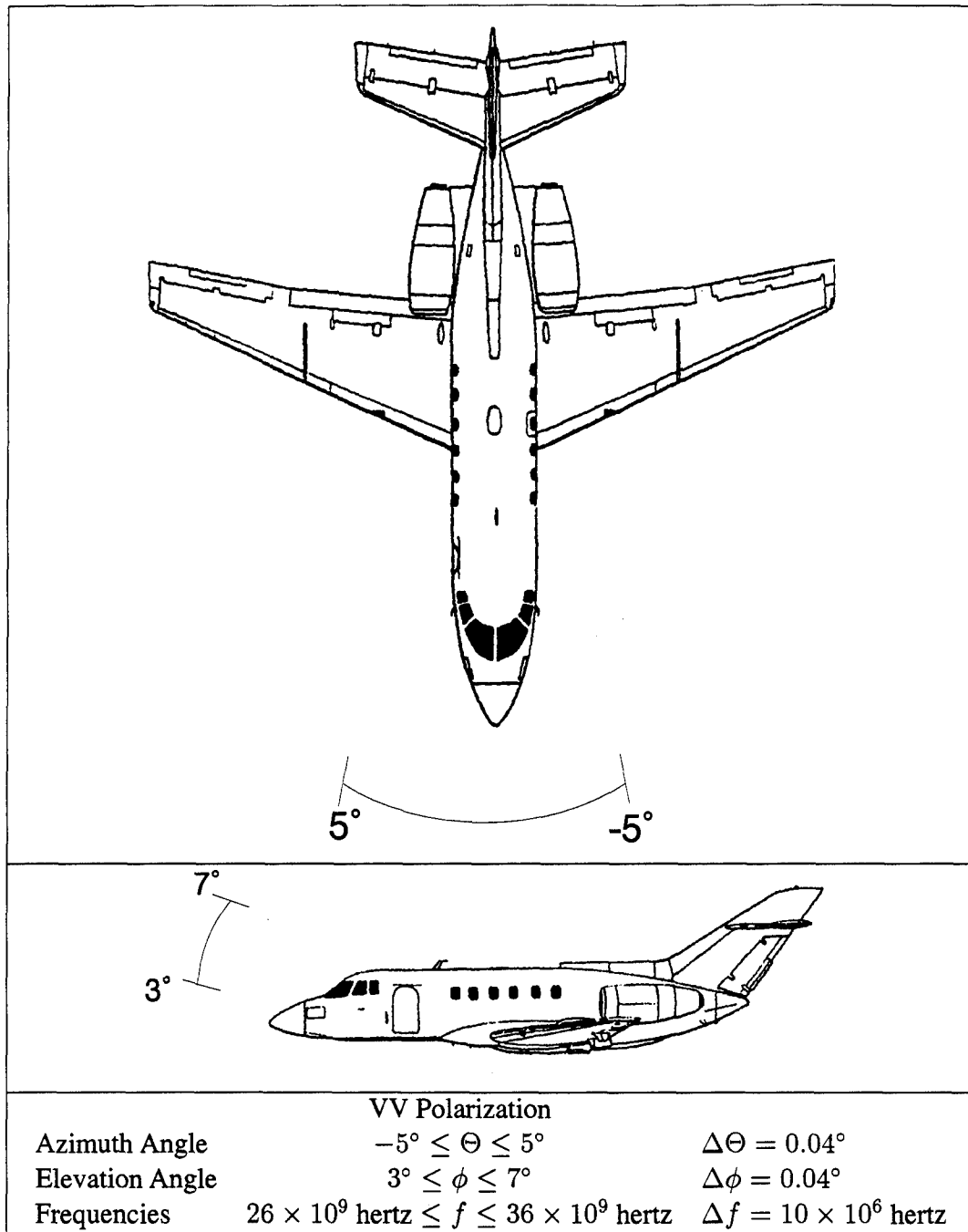
Figure 13. Geometry for Nose Data Series.

HH Polarization		
Azimuth Angle	$19° \leq \Theta \leq 29°$	$\Delta\Theta = 0.04°$
Elevation Angle	$3° \leq \phi \leq 7°$	$\Delta\phi = 0.04°$
Frequencies	26×10^9 hertz $\leq f \leq 36 \times 10^9$ hertz	$\Delta f = 10 \times 10^6$ hertz
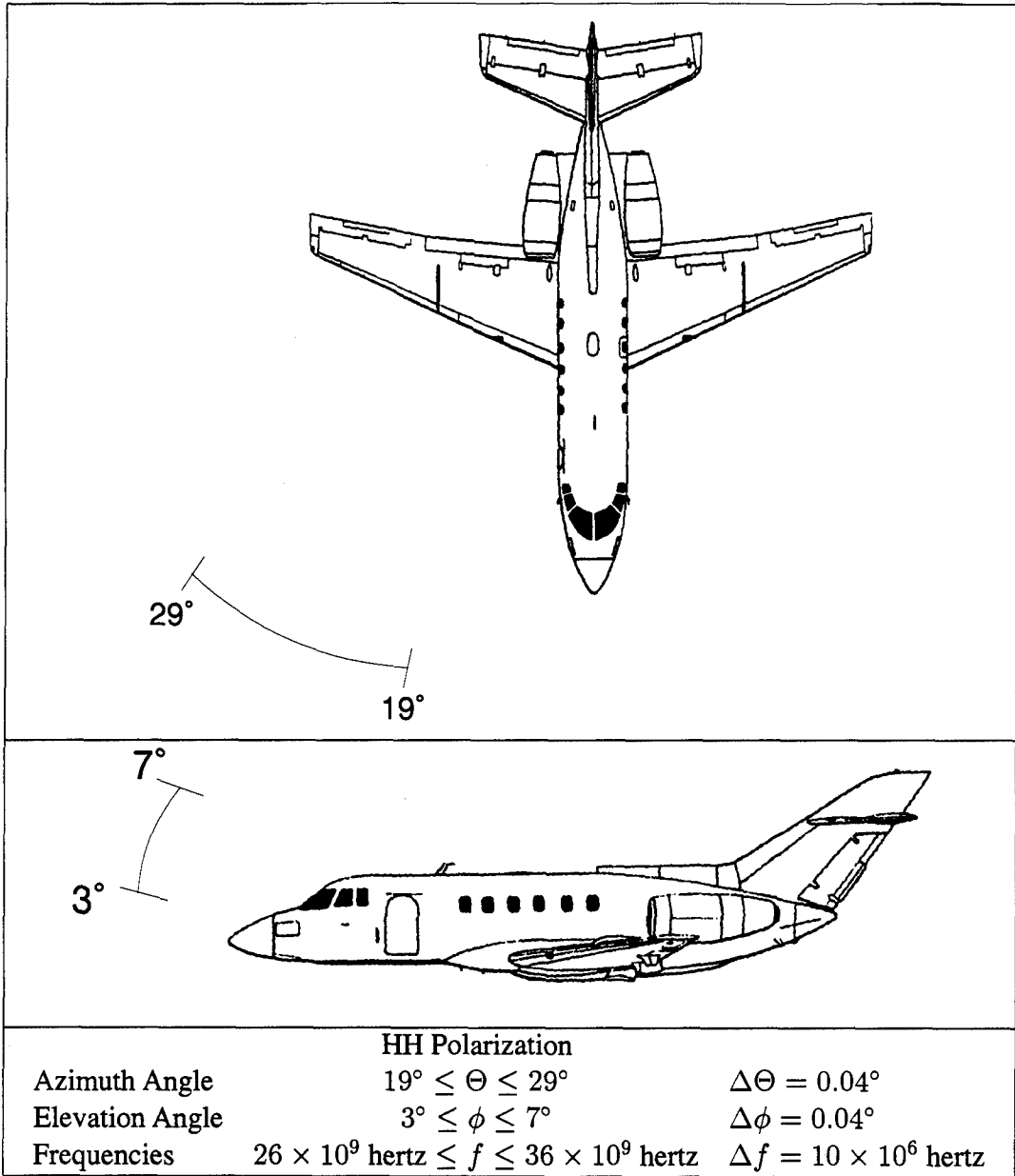
Figure 14. Geometry for Wing Data Series.
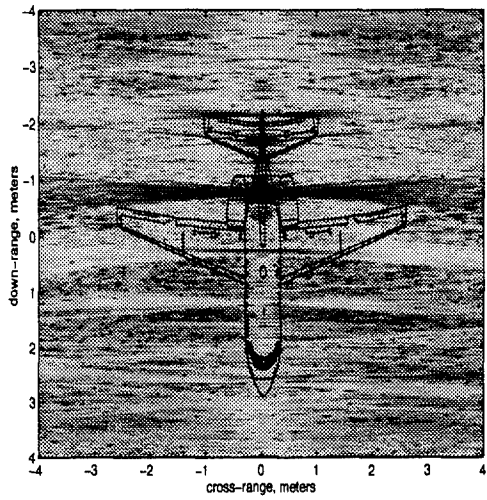
(a)
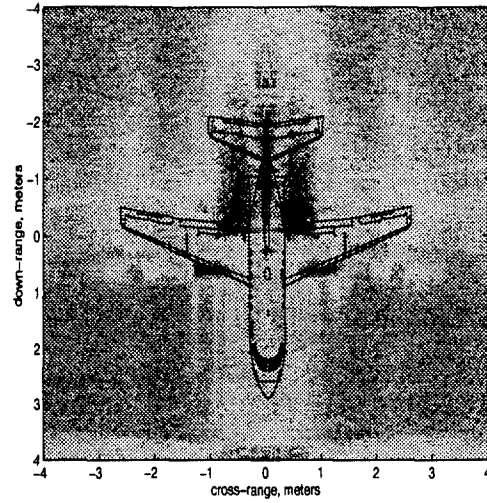
(b)
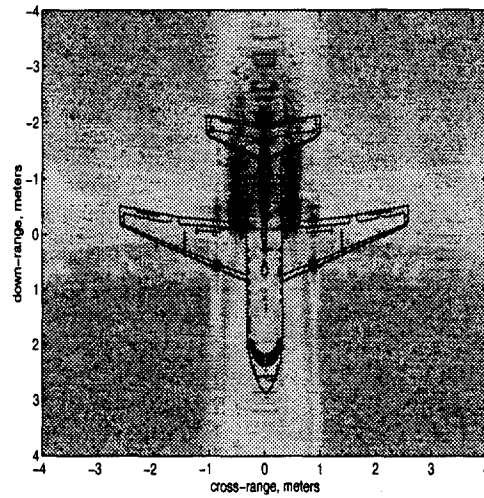
(c)

Figure 15.   Illustration of effect of up sampling on image quality. (a) no up sampling; (b) 6
              times up sampling; (c) 20 times up sampling.

IV. Results

4.1 Introduction

This chapter presents the three-dimensional images of the C-29 aircraft. These images are in the form of iso-surface images as well as two-dimensional slices. The images are discussed and compared to the physical properties of the target.

4.2 Nose Data

Three-dimensional pixel values were computed using the nose data set described in Figure 13 and the algorithm developed in Section 2.4. The volume consists of 720,000 pixels and has the following dimensions,

$$-3.0 \text{ meters} \leq x \leq 3.0 \text{ meters} \quad \text{stepsize } \Delta x = 0.05 \text{ meters}$$

$$-3.0 \text{ meters} \leq y \leq 3.0 \text{ meters} \quad \text{stepsize } \Delta y = 0.05 \text{ meters}$$

$$-0.5 \text{ meters} \leq z \leq 2.0 \text{ meters} \quad \text{stepsize } \Delta z = 0.05 \text{ meters}.$$

Figure 16 shows the top view of the iso-surface for this volume. The silhouette of the actual target is overlayed on the image. The returns of the engines and landing lights on the leading edge of the wings are readily visible. Figure 17 is the same iso-surface observed from the front. The vertical separation of the engines and landing lights is evident and shows the true three-dimensionality of these results. The pedestal exhibits large returns due to the fact that VV polarization was used and the pedestal was not subtracted out of the measurements. Sidelobes from the engines are also seen from this view.

By looking at two-dimensional slices taken at the major scatterers it is easy to see that they line up with the physical characteristics of the target. Figure 18 shows a contour plot in the xz plane at the leading edge of the engines. An image of this same slice is shown in Figure 19 from a different aspect. Figure 20 is a contour plot in the xz plane showing the reflections from the APU intake and Figure 21 is a slice taken of the same area. Figures 22 and 23 shows reflections from the landing lights.

31
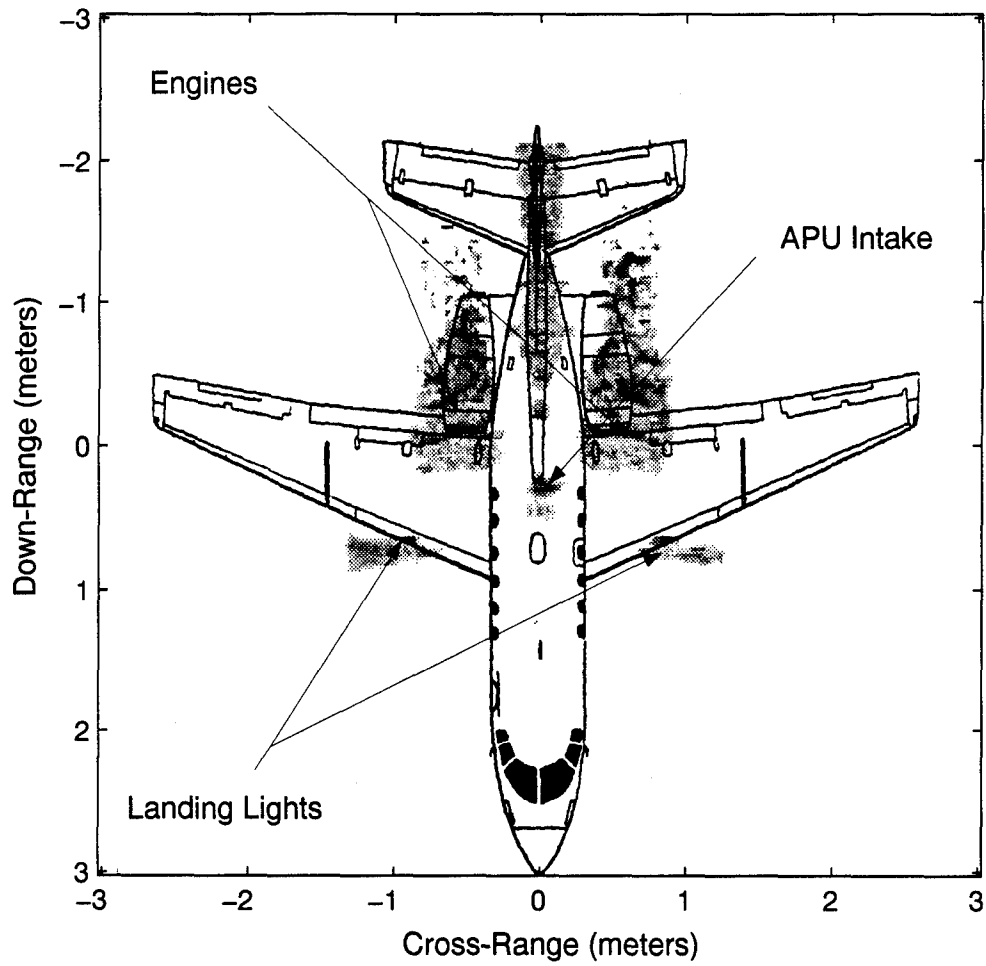
Figure 16. Top view of iso-surface from nose data.
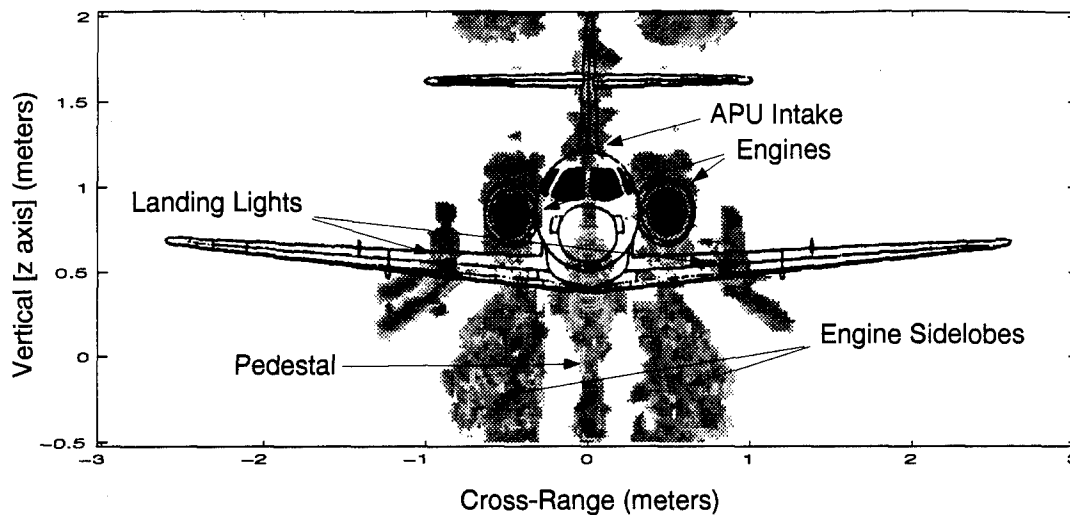
Figure 17. Front view of iso-surface from nose data.

Two-dimensional slices were also made in the xy plane to verify the precision of the return's locations in the z dimension when compared to the target. Figure 24 is a slice through the engines in the xy plane and clearly shows the engine's reflections. Figure 25 is a slice through the location of the APU intake in the xy plane and Figure 26 shows a slice through the landing lights.

Figures 27 through 33 are slices taken in the xz plane of the whole volume computed from the nose data. These slices are taken every 0.1513 meters going from front to back. Figures 34 through 36 are slices taken in the xy plane of the same volume. These slices are taken every 0.1530 meters from top to bottom. Figures 37 through 42 are expanded views of some of the slices taken at critical areas. They are also presented with the outline of the plane overlayed on them.
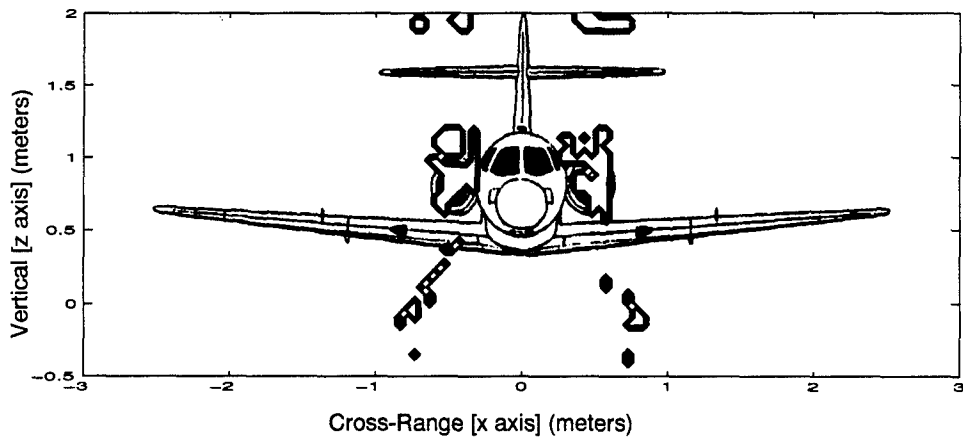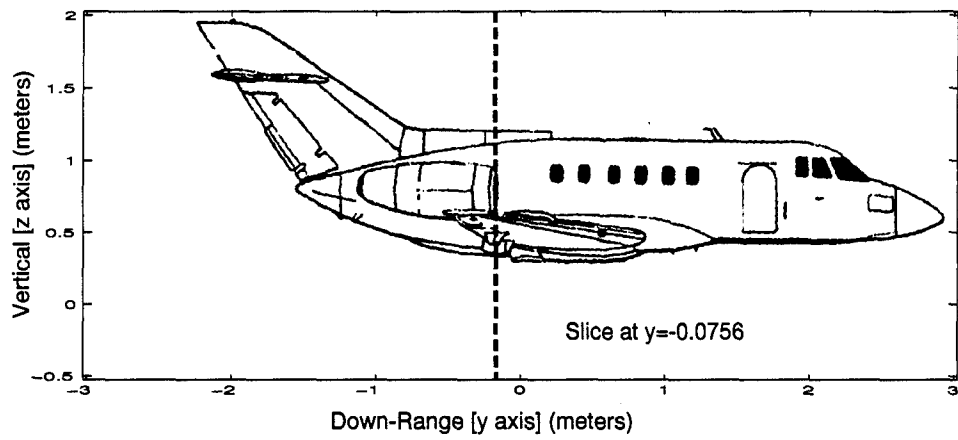
Figure 18. Contour plot in xz plane of engine returns.
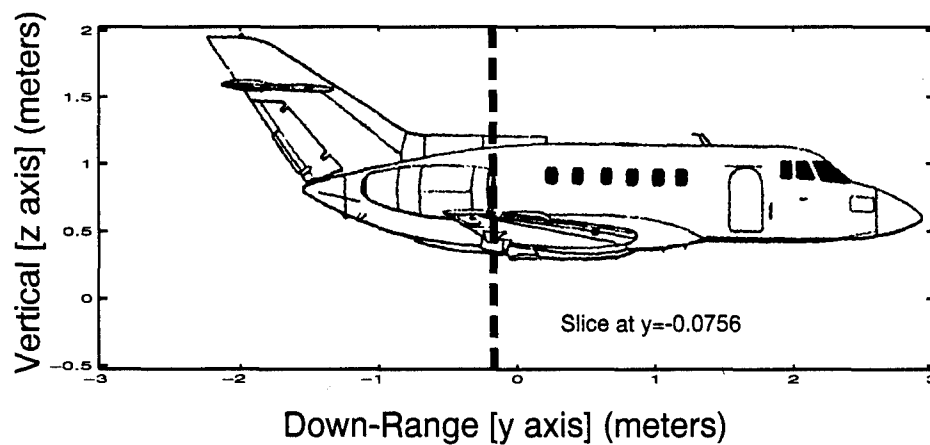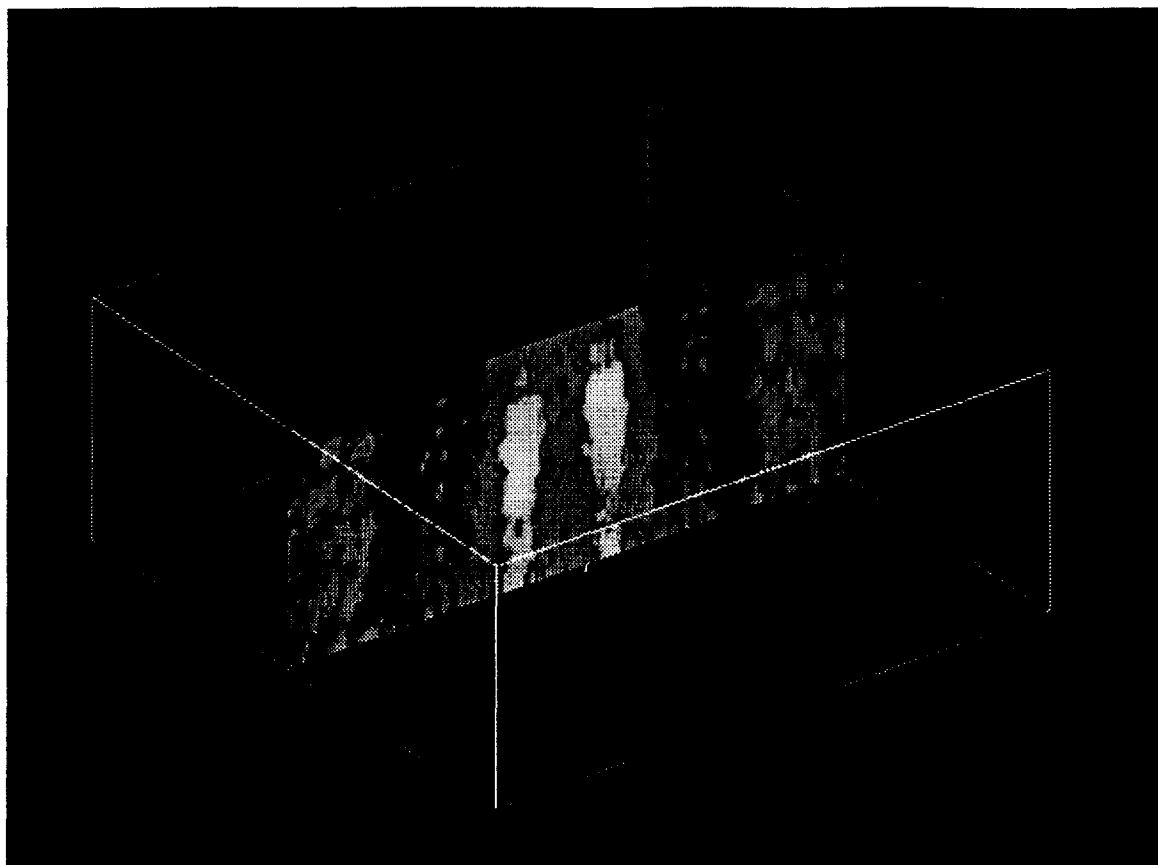
Figure 19. Slice in xz plane of engine returns.
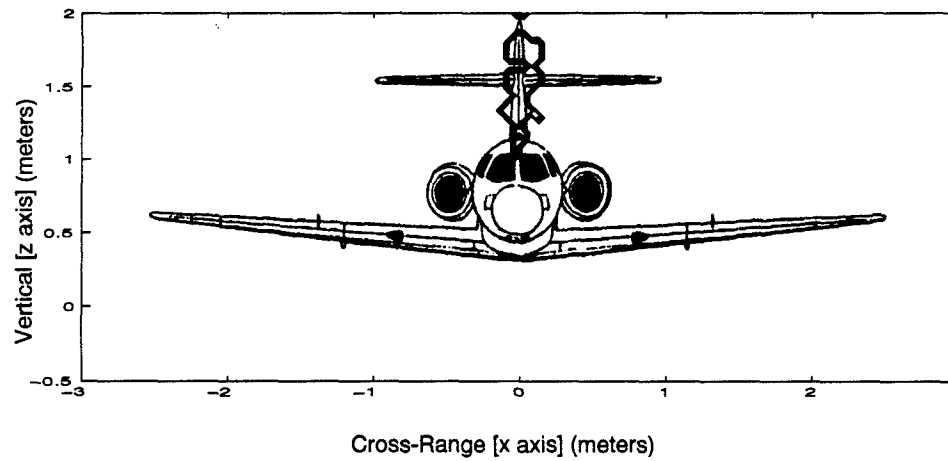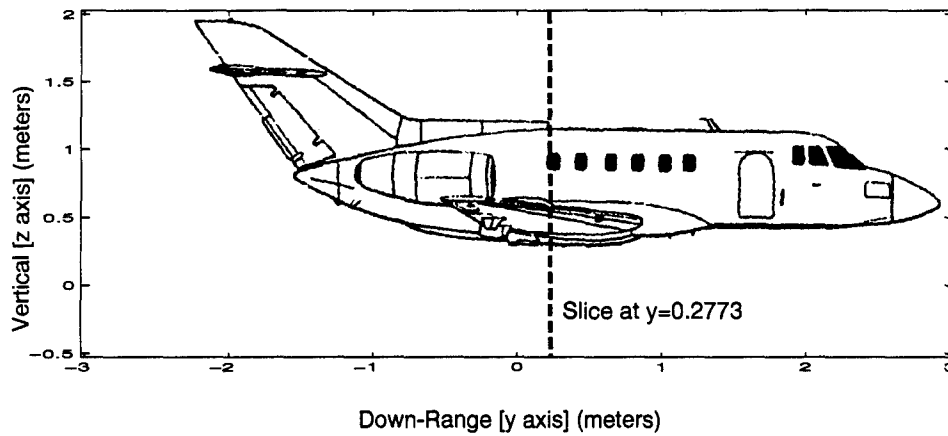
Figure 20. Contour plot in xz plane of intake returns.
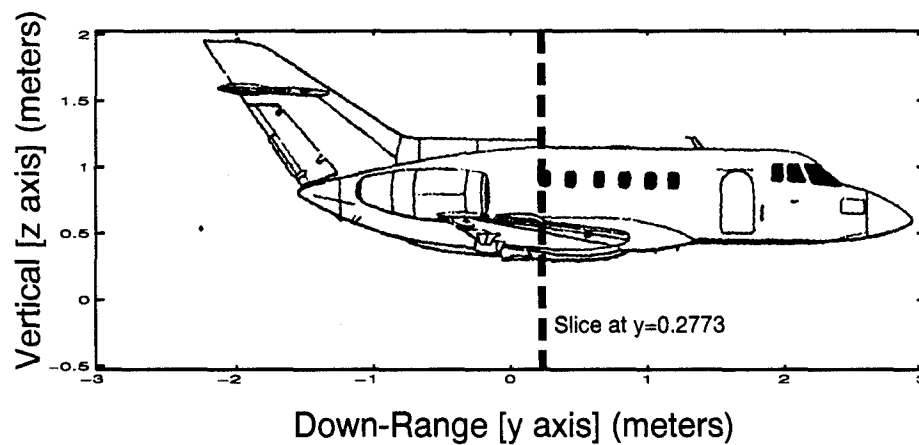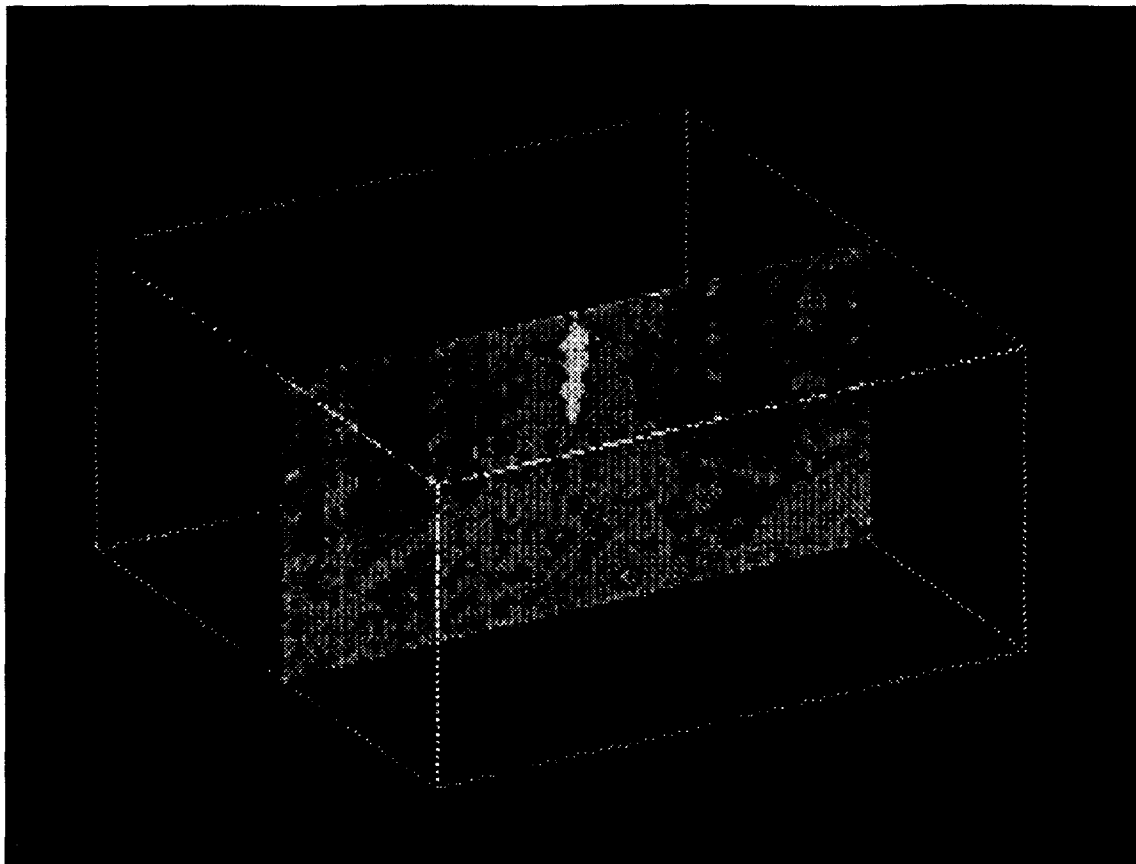
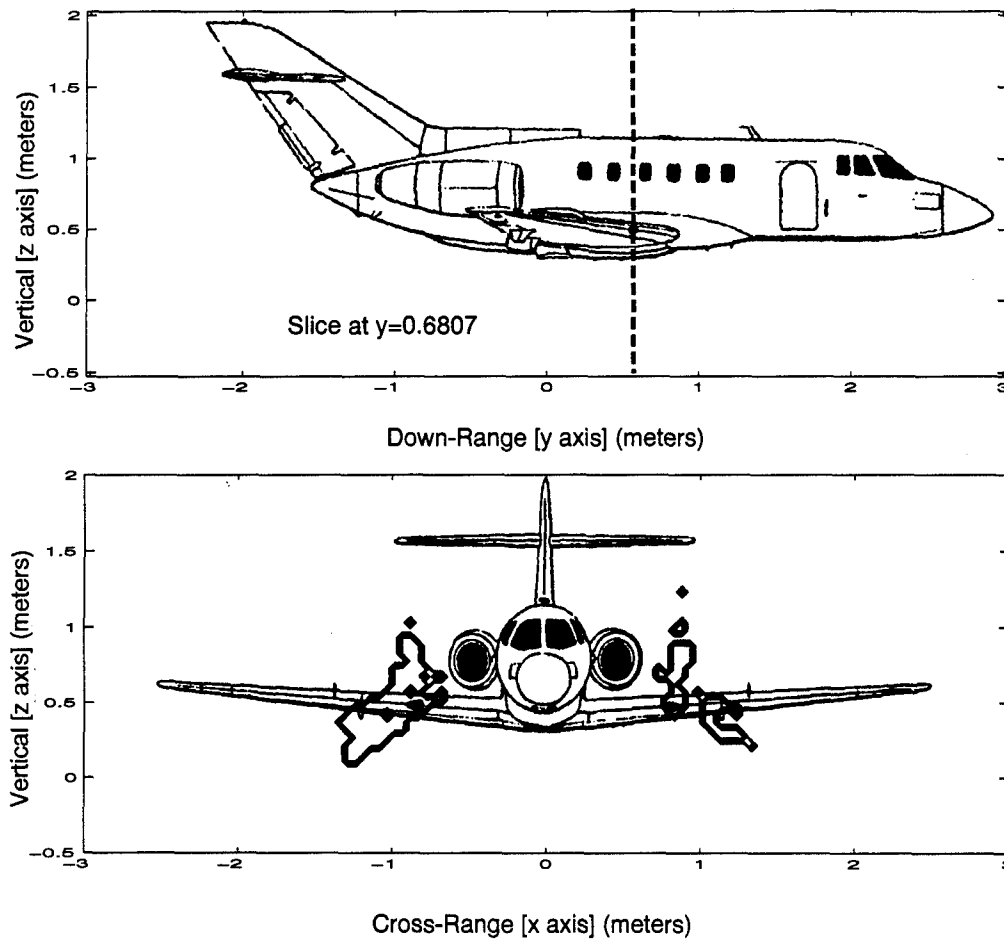Figure 21. Slice in xz plane of intake returns.

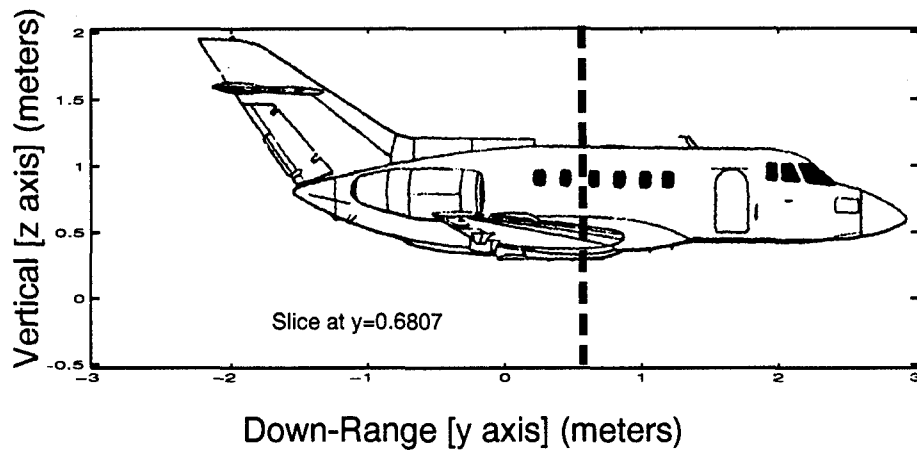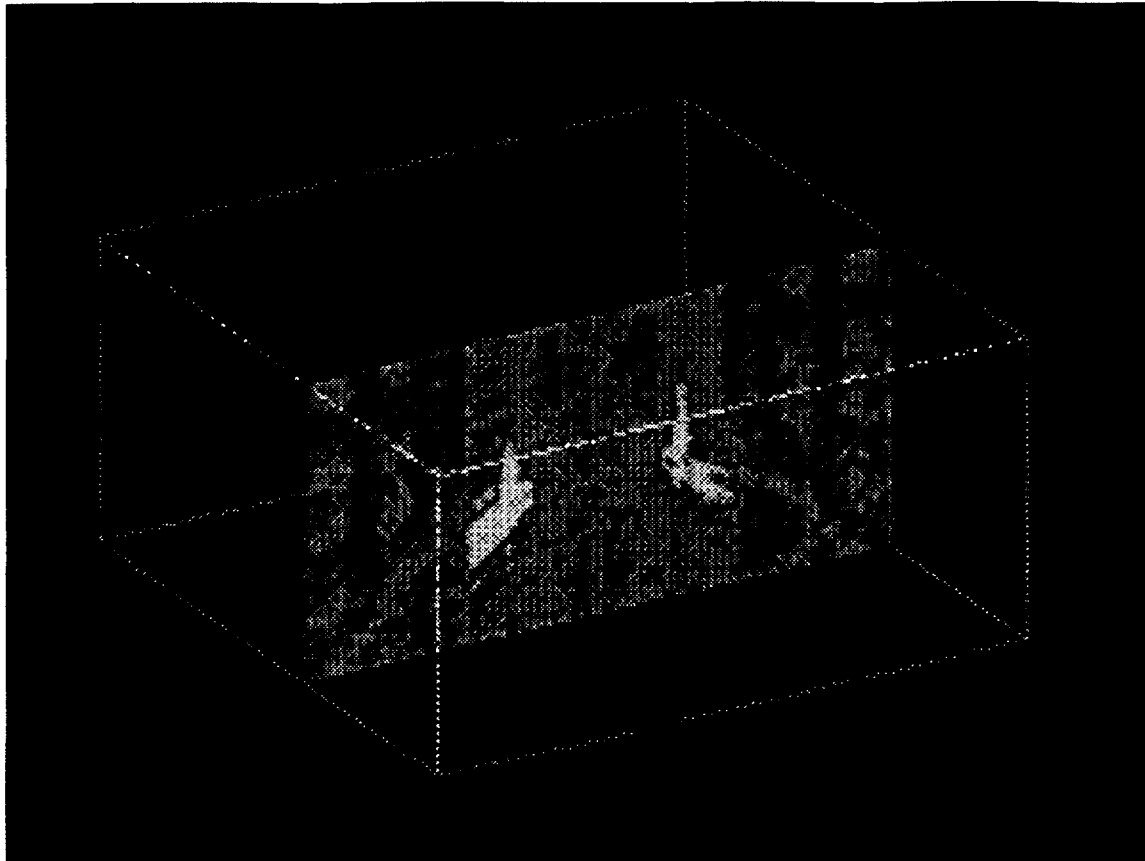Figure 22. Contour plot in xz plane of landing lights returns.

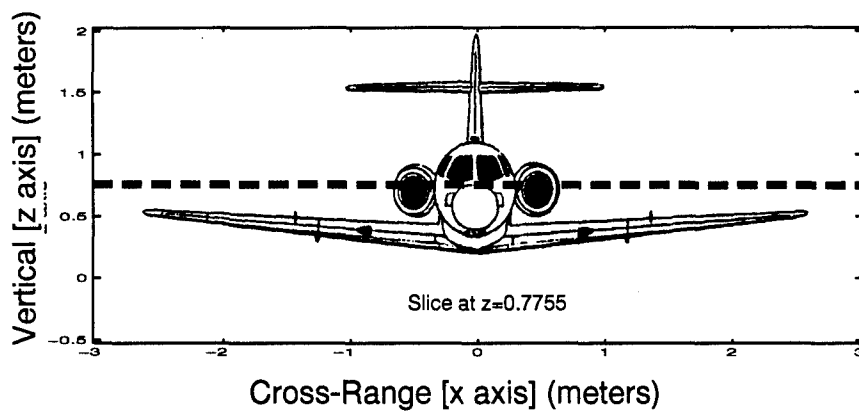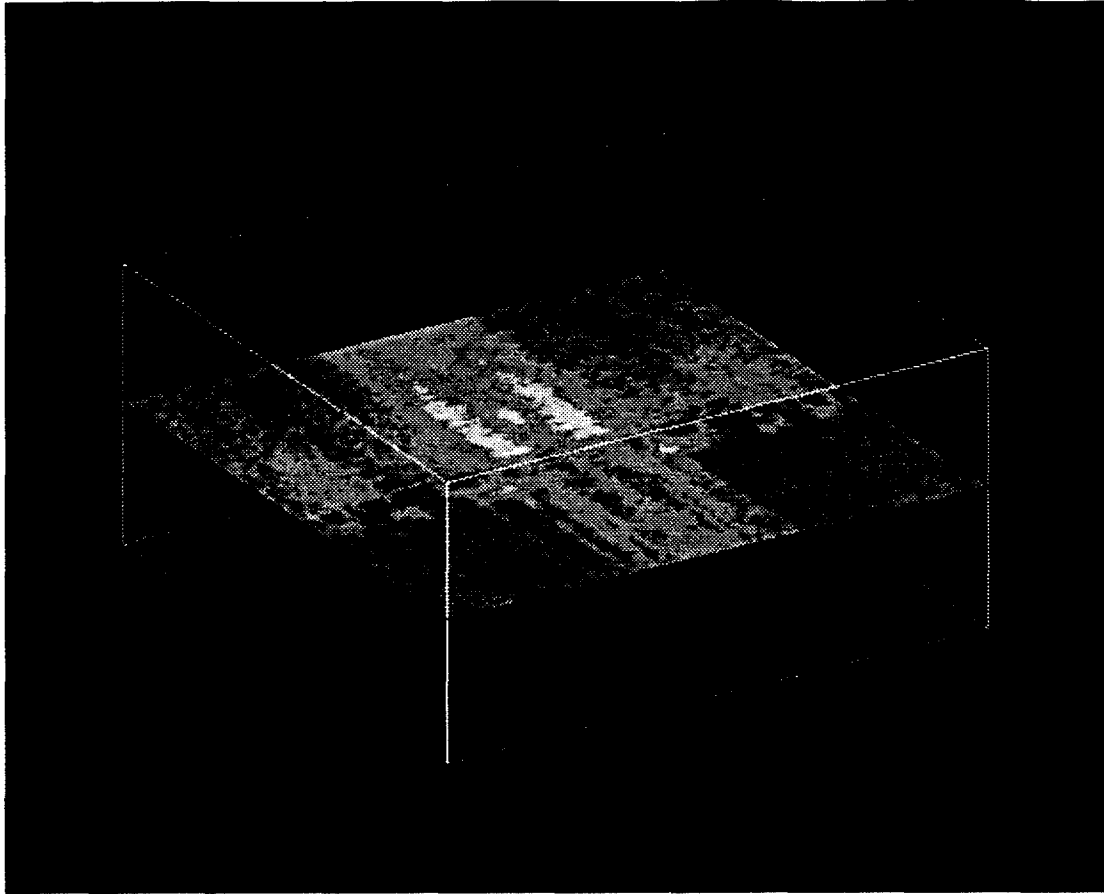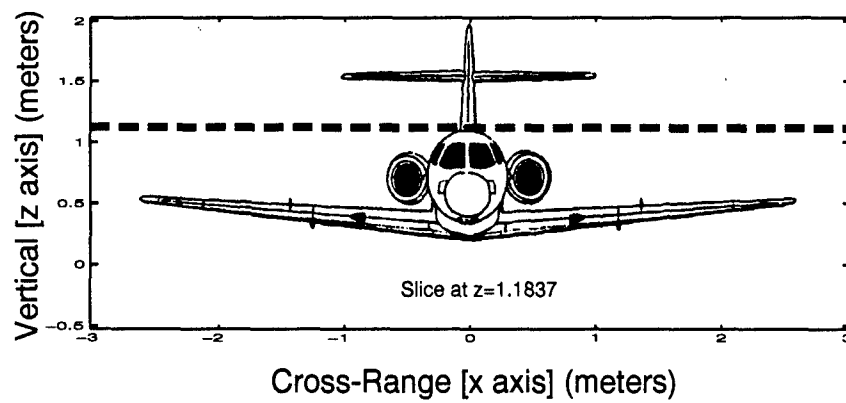Figure 23. Slice in xz plane of landing lights returns.

39

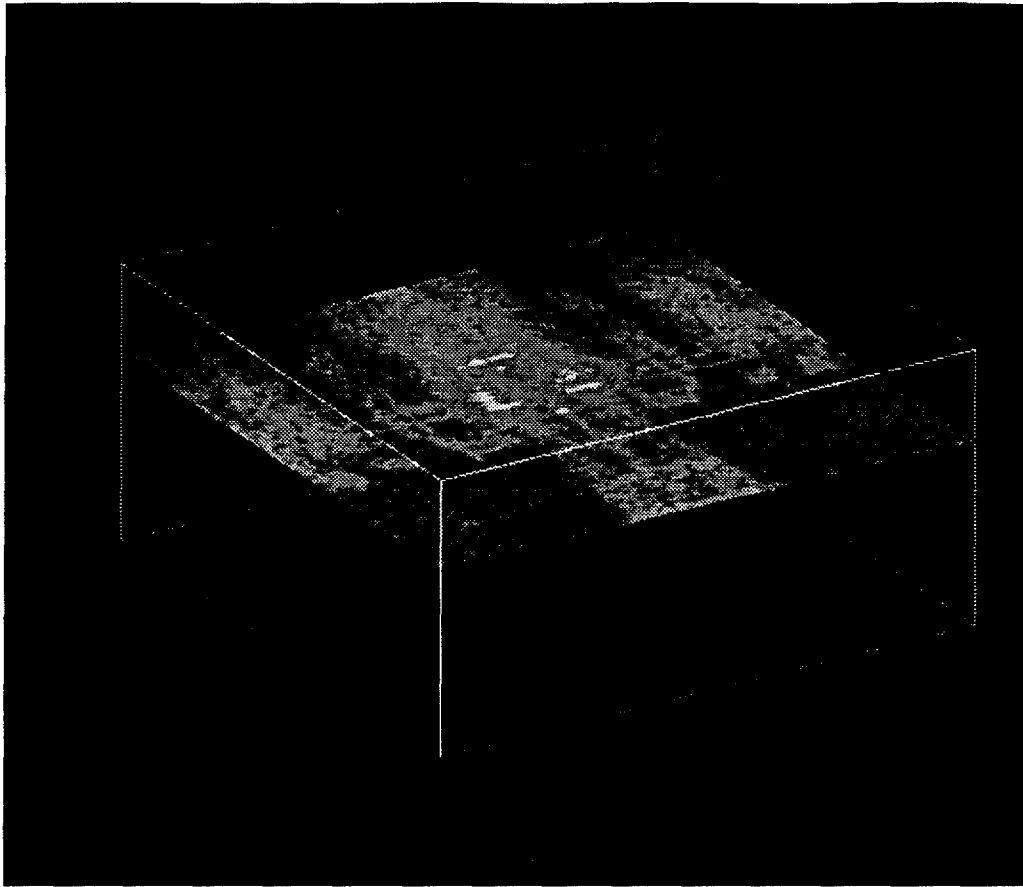Figure 24. Slice in xy plane of engine returns.

40

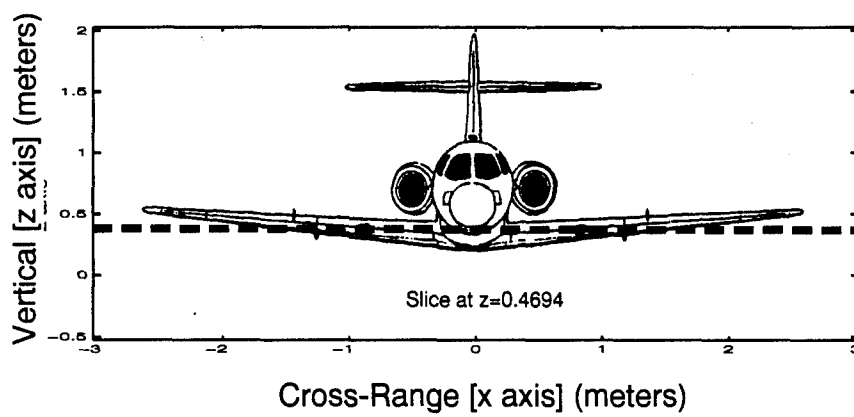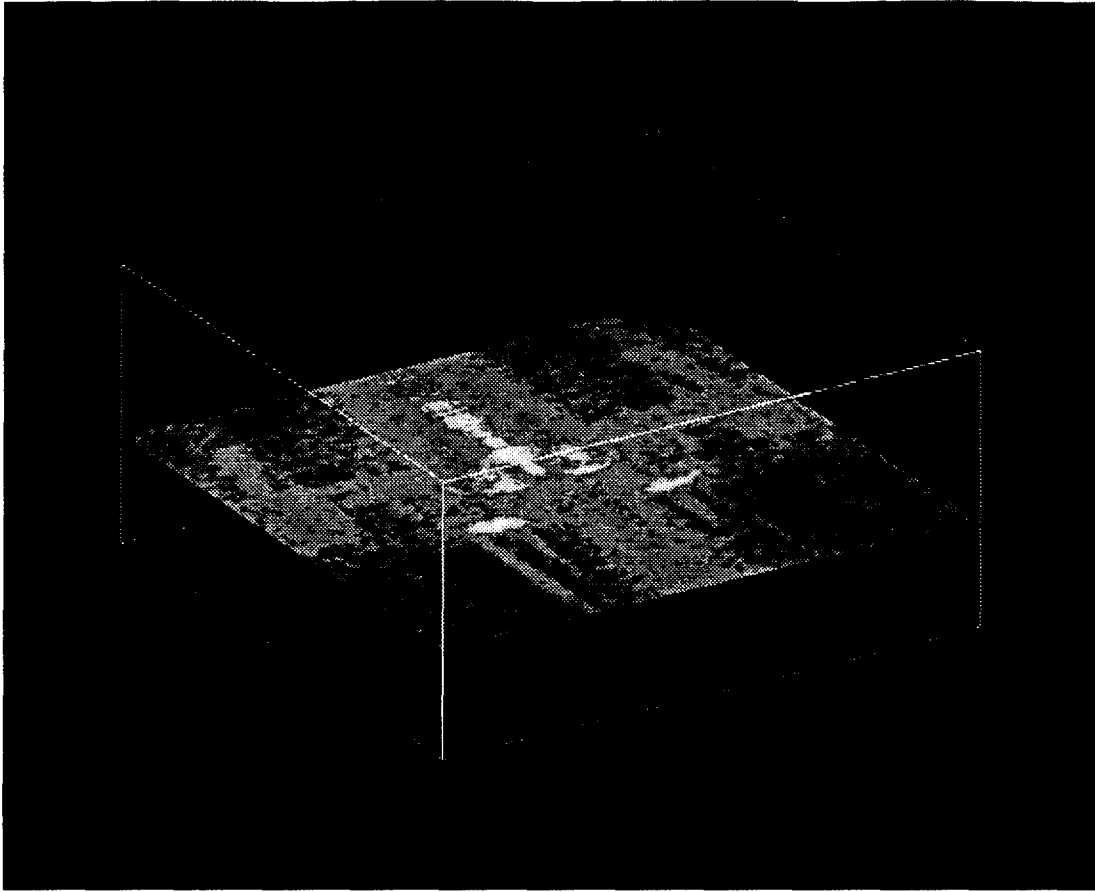Figure 25. Slice in xy plane of APU intake returns.

41

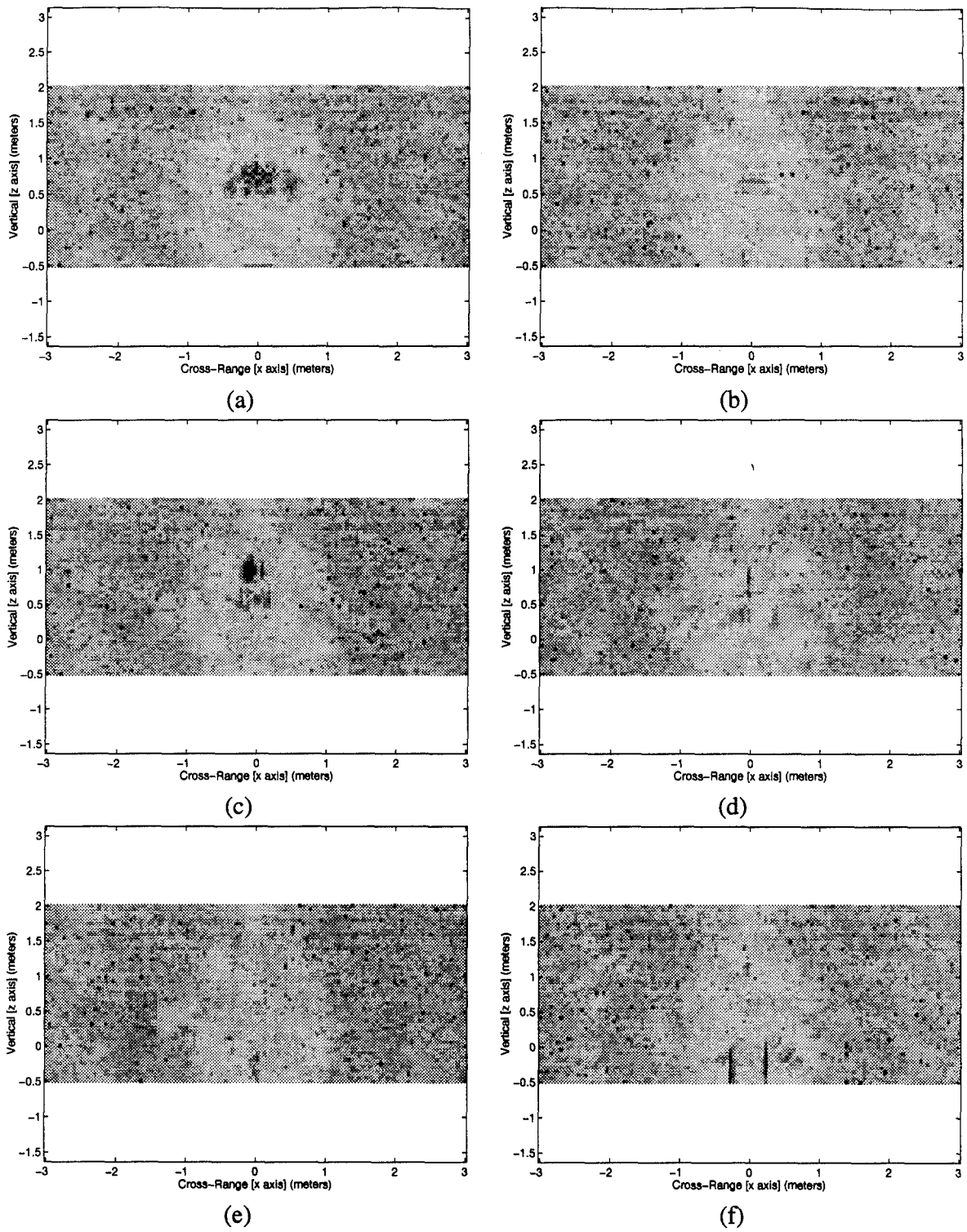Figure 26. Slice in xy plane of landing lights returns.

Figure 27.   Nose Data: xz plane slices at (a) $y = 3.0000$ meters (b) $y = 2.8487$ meters (c) $y = 2.6975$ meters (d) $y = 2.5462$ meters (e) $y = 2.3950$ meters (f) $y = 2.2437$ meters.
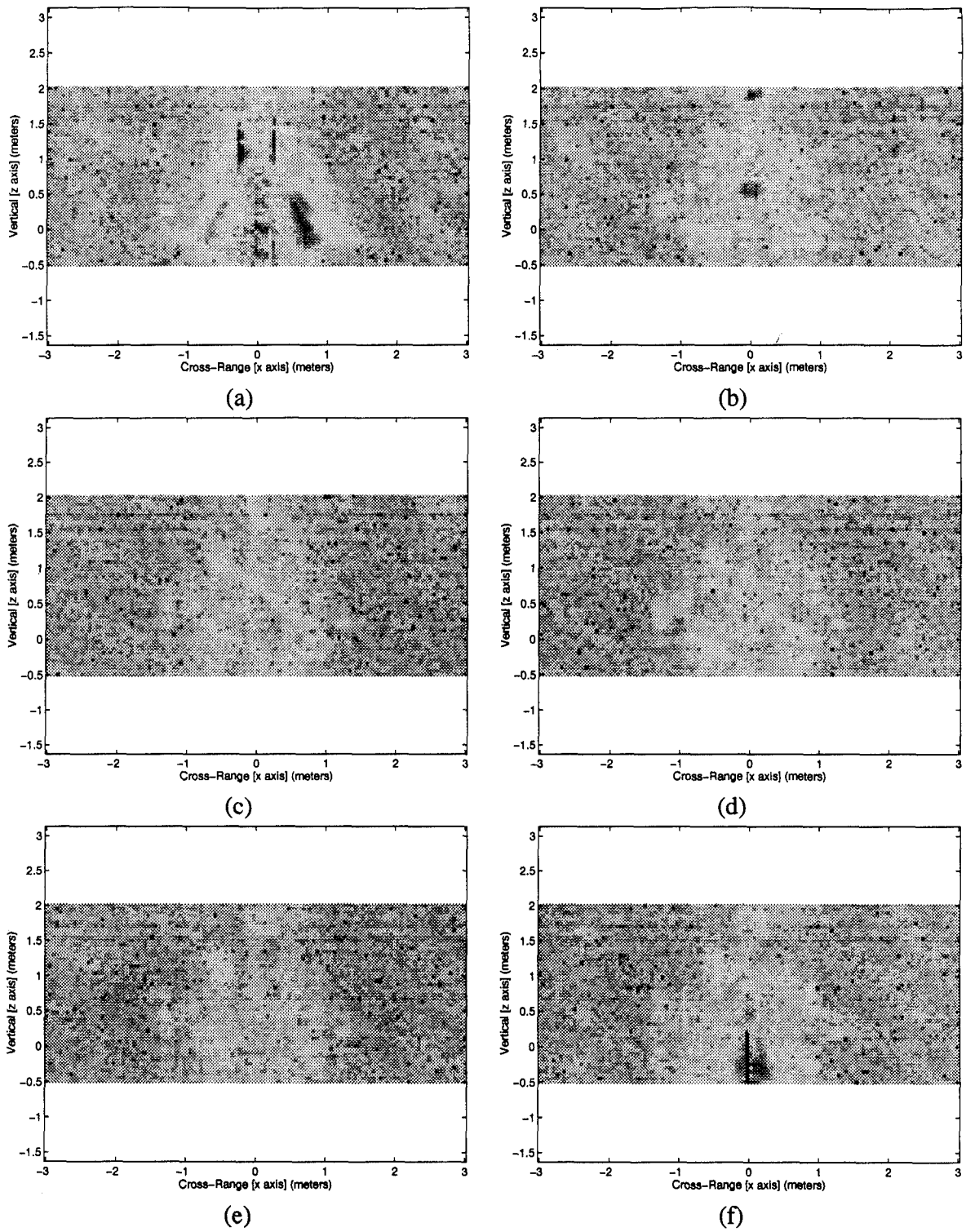
43

Figure 28.   Nose Data: xz plane slices at (a) $y = 2.0924$ meters (b) $y = 1.9412$ meters (c) $y = 1.7899$ meters (d) $y = 1.6387$ meters (e) $y = 1.4874$ meters (f) $y = 1.3361$ meters.
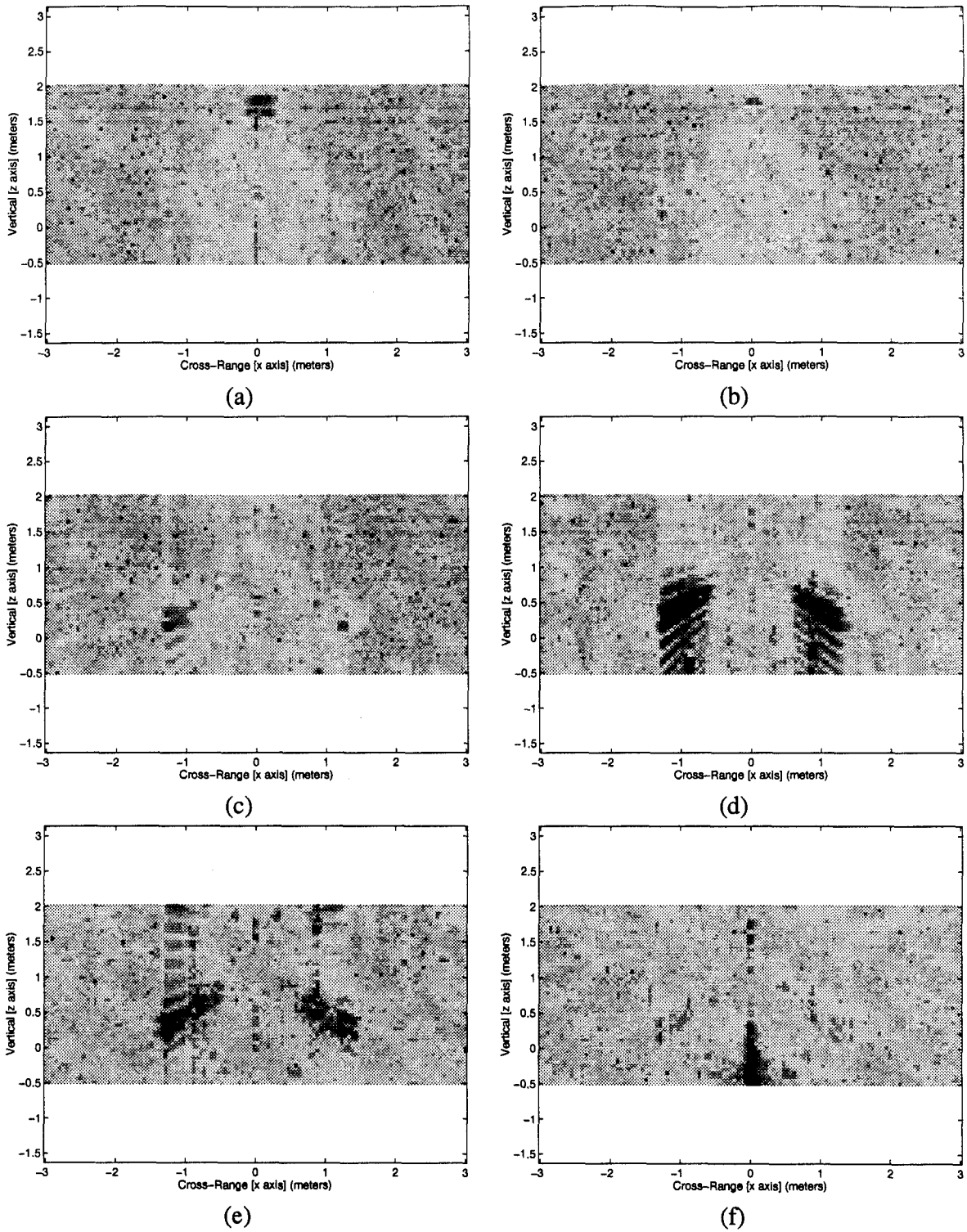
44

Figure 29. Nose Data: xz plane slices at (a) $y = 1.1849$ meters (b) $y = 1.0336$ meters (c) $y = 0.8824$ meters (d) $y = 0.7311$ meters (e) $y = 0.5798$ meters (f) $y = 0.4286$ meters.
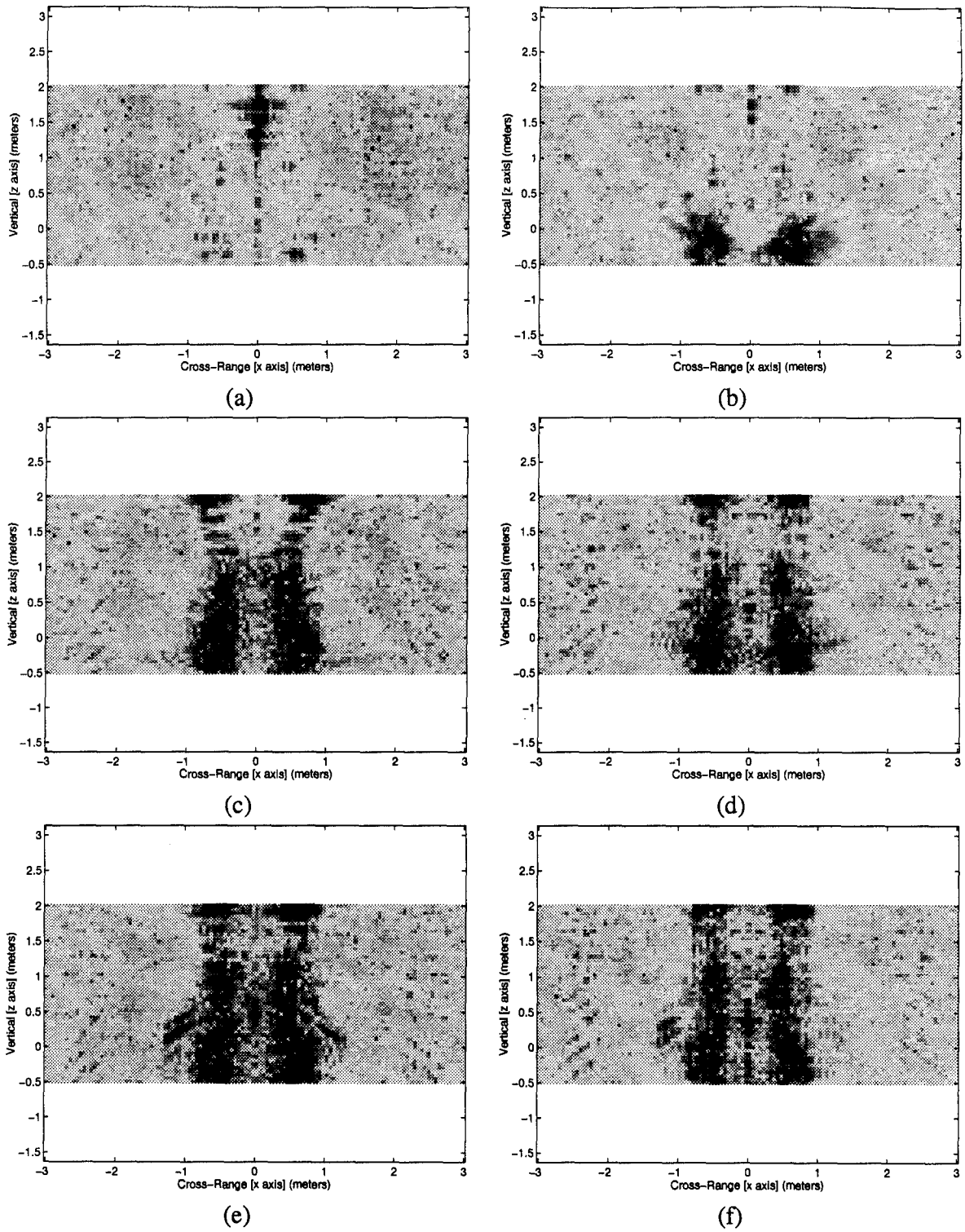
Figure 30.   Nose Data: xz plane slices at (a) $y = 0.2773$ meters (b) $y = 0.1261$ meters (c) $y = -0.0252$ meters (d) $y = -0.1765$ meters (e) $y = -0.3277$ meters (f) $y = -0.4790$ meters.
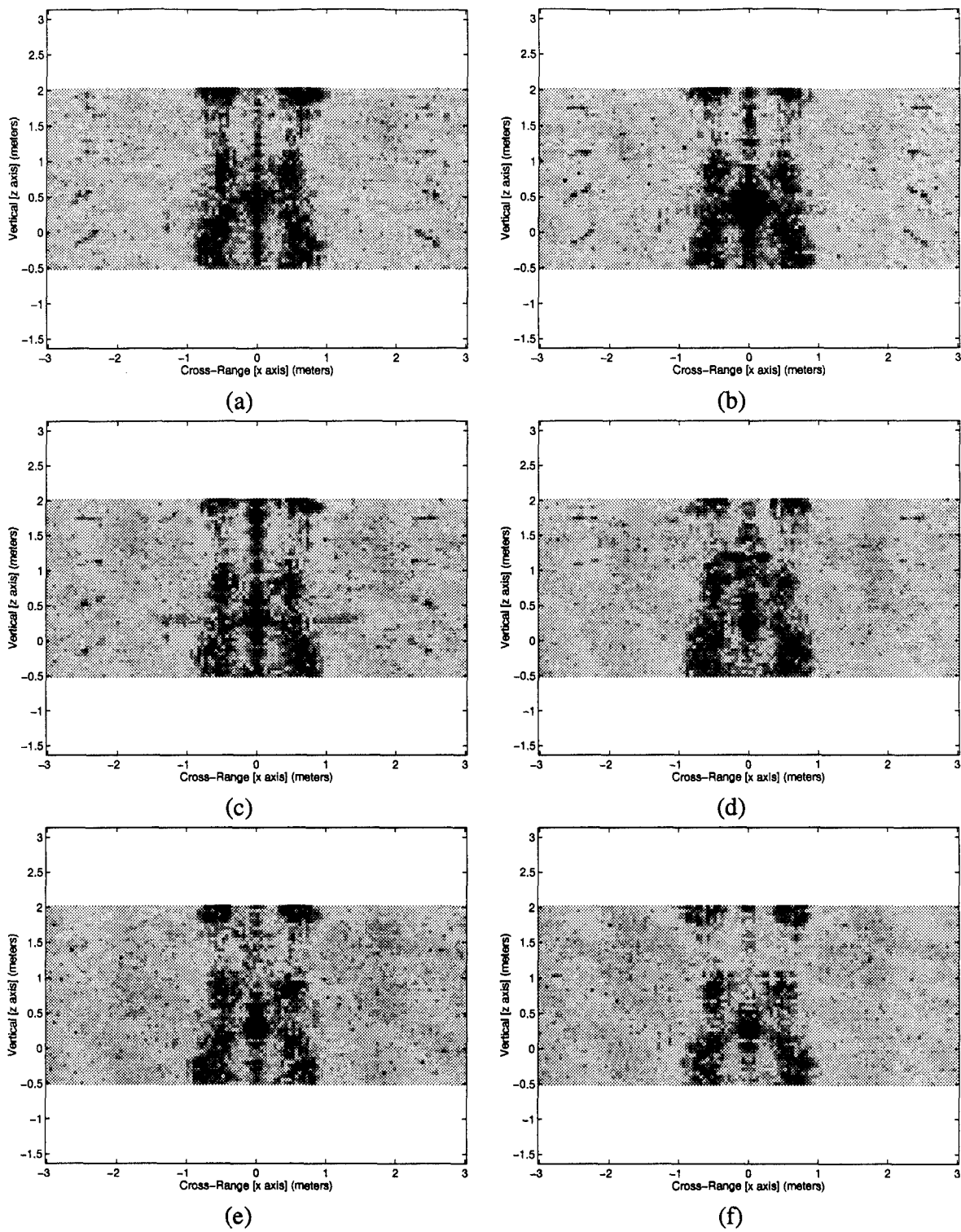
46

Figure 31.   Nose Data: xz plane slices at (a) $y = -0.6303$ meters (b) $y = -0.7815$ meters (c) $y = -0.9328$ meters (d) $y = -1.0840$ meters (e) $y = -1.2353$ meters (f) $y = -1.3866$ meters.
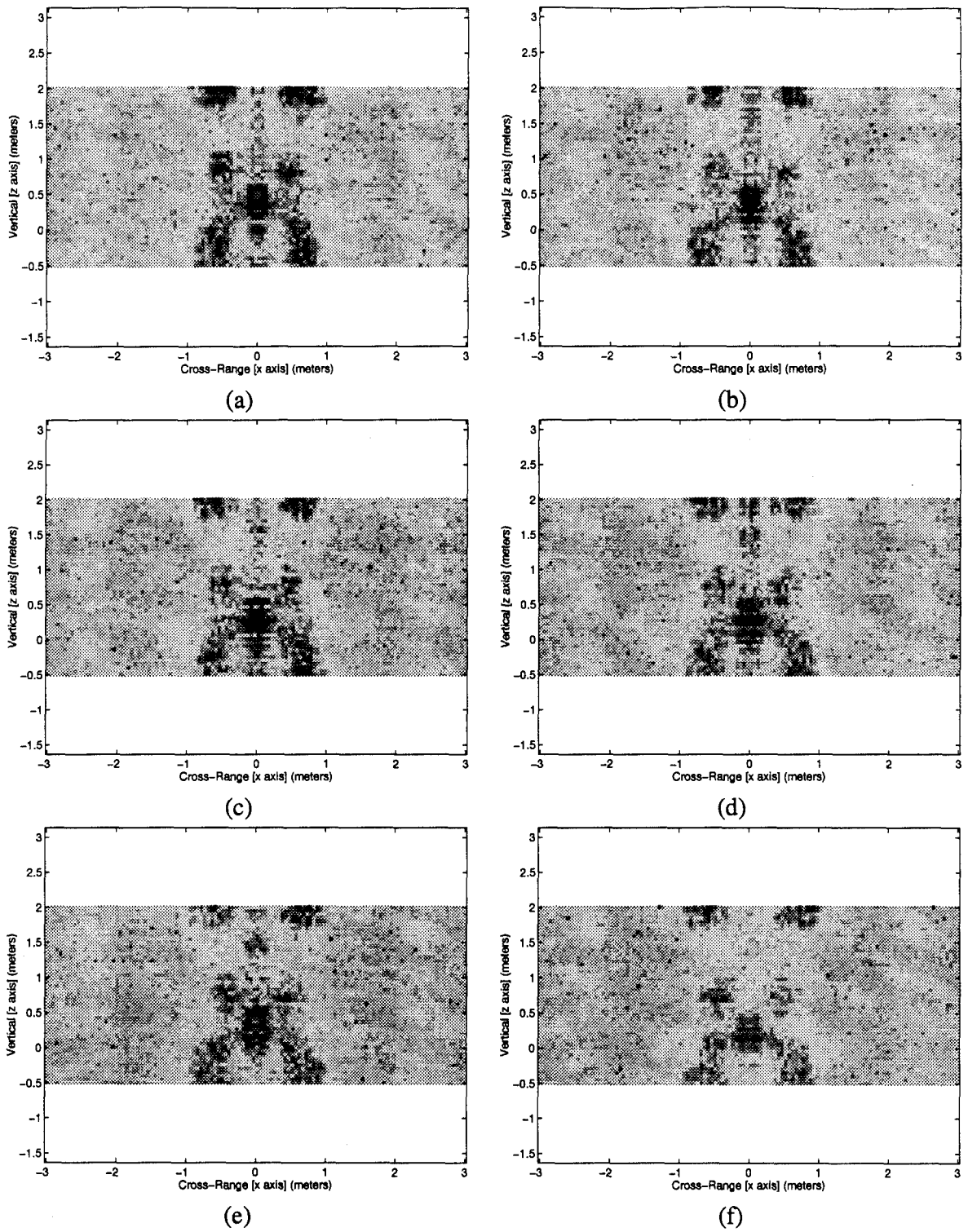
Figure 32. Nose Data: xz plane slices at (a) $y = -1.5378$ meters (b) $y = -1.6891$ meters (c) $y = -1.8403$ meters (d) $y = -1.9916$ meters (e) $y = -2.1429$ meters (f) $y = -2.2941$ meters.
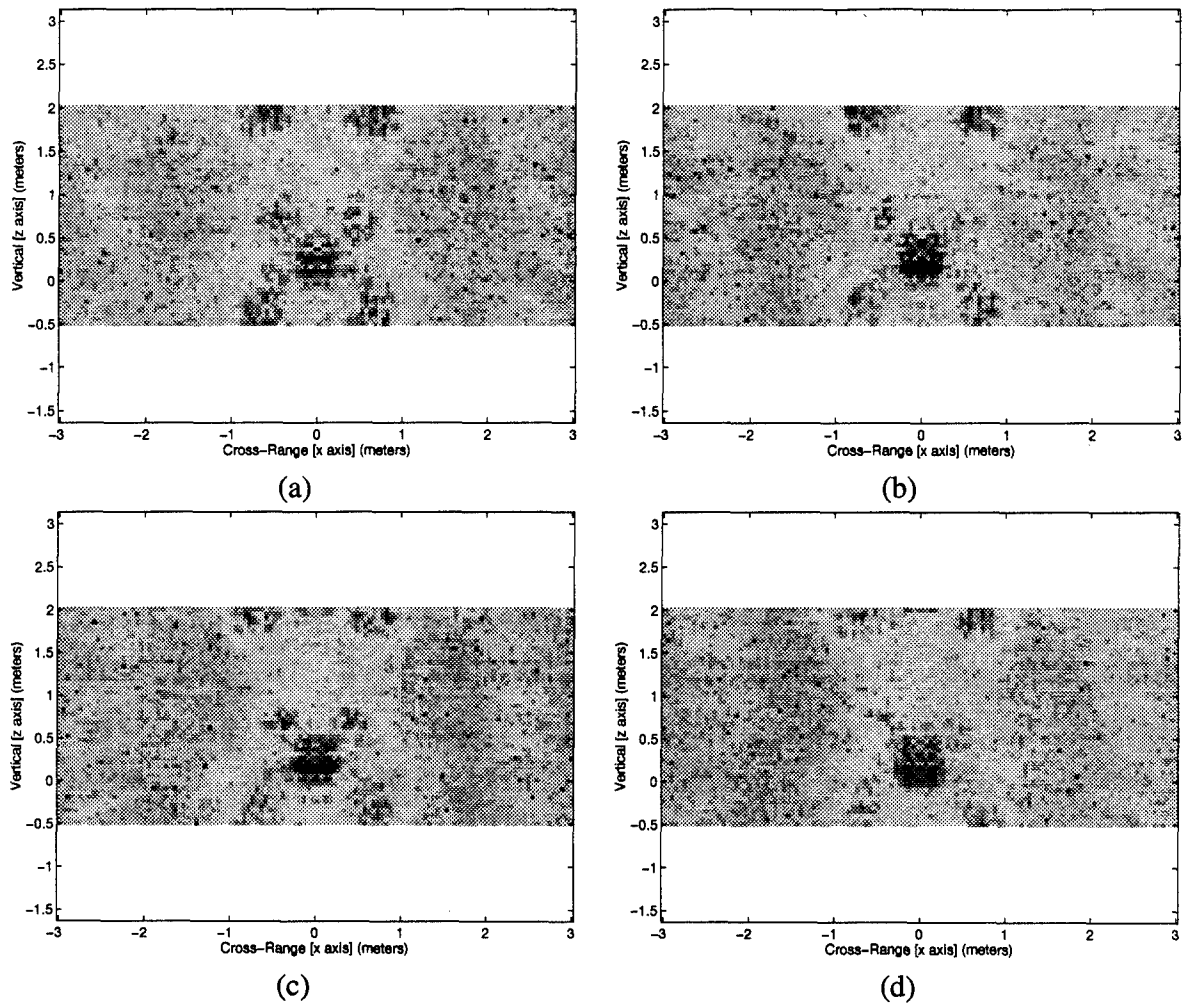
48

Figure 33. Nose Data: xz plane slices at (a) $y = -2.4454$ meters (b) $y = -2.5966$ meters (c) $y = -2.7479$ meters (d) $y = -2.8992$ meters.
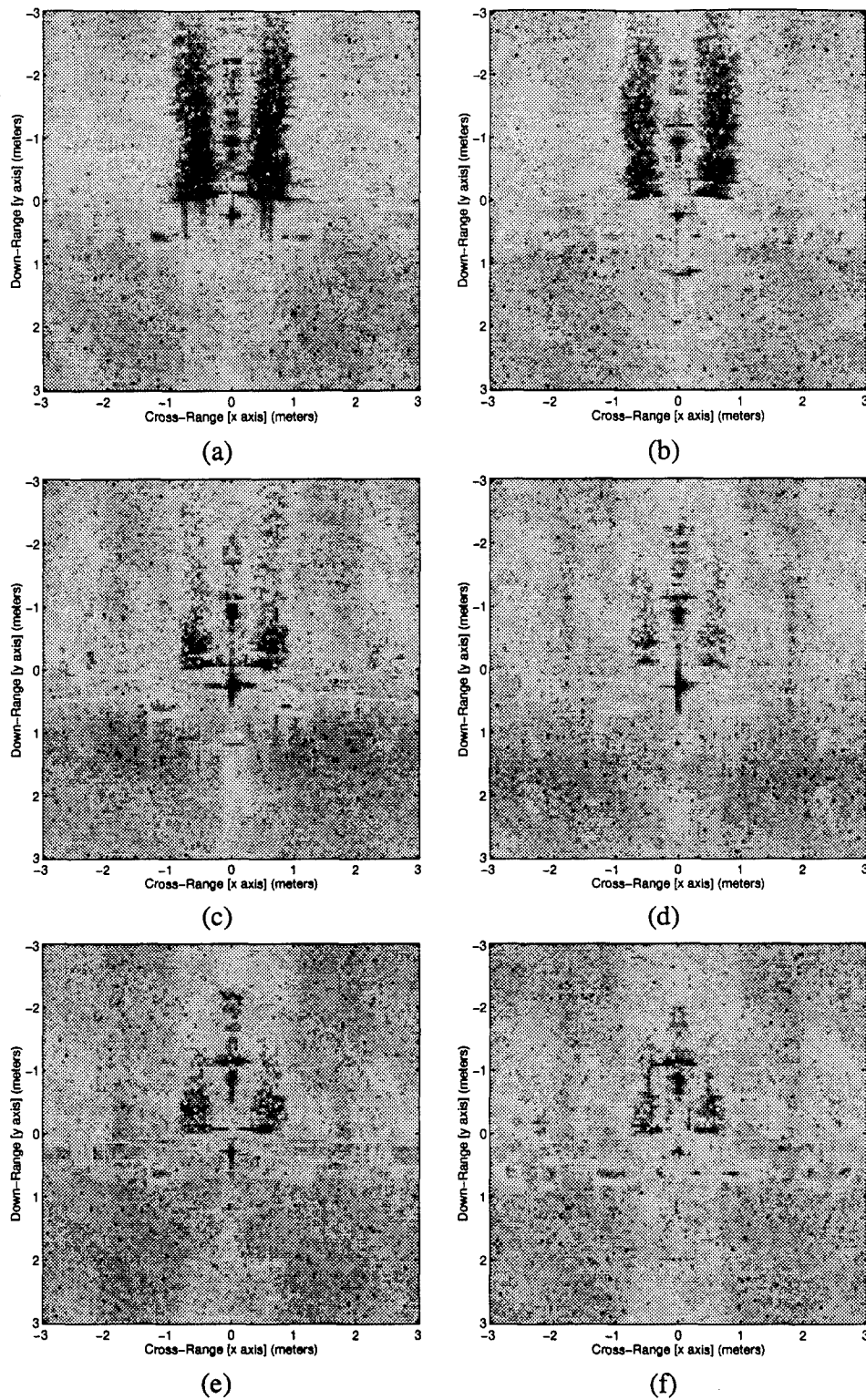
Figure 34.   Nose Data: xy plane slices at (a) $z = 2.0000$ meters (b) $z = 1.8469$ meters (c) $z = 1.6939$ meters (d) $z = 1.5408$ meters (e) $z = 1.3878$ meters (f) $z = 1.2347$ meters.
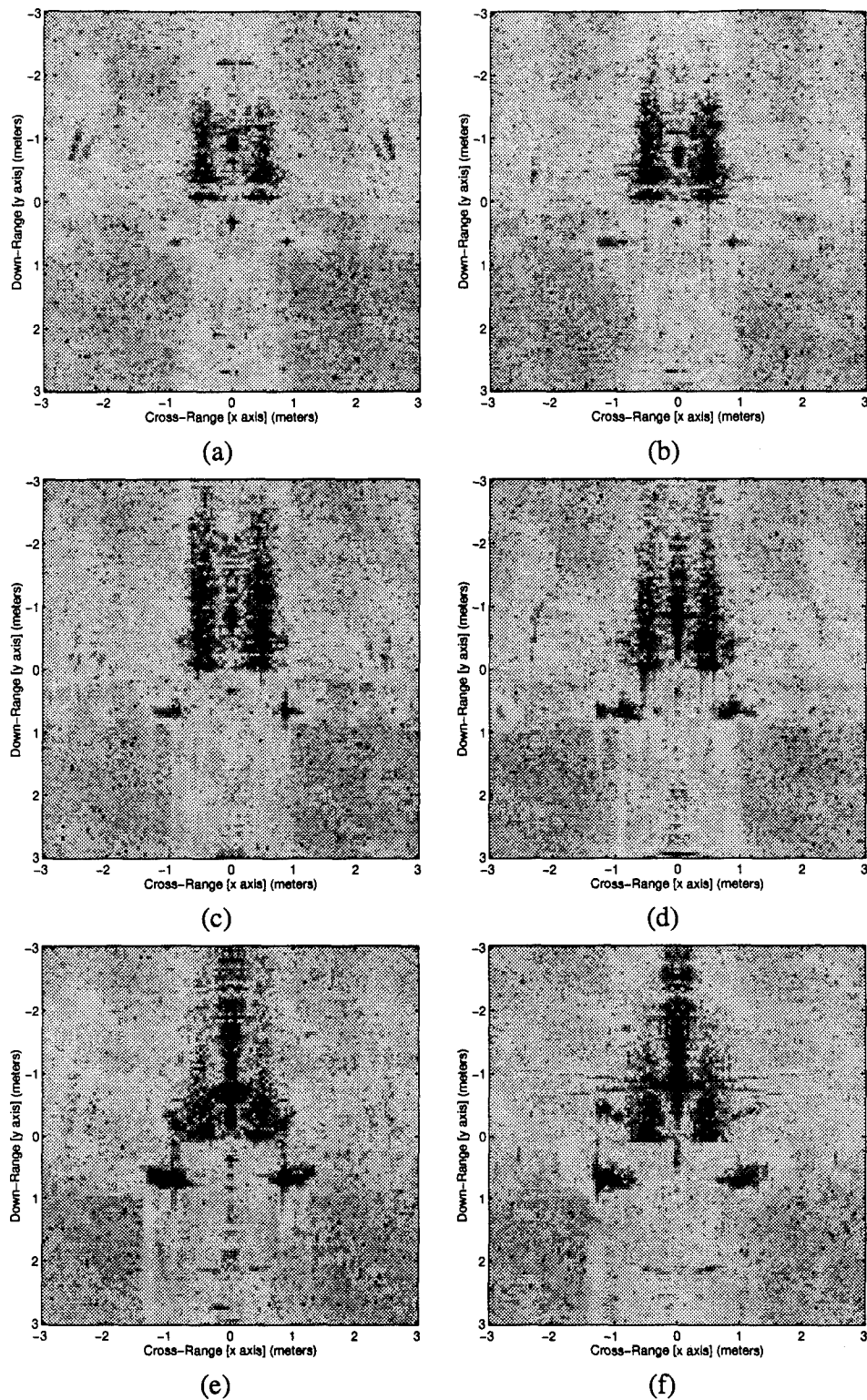
Figure 35. Nose Data: xy plane slices at (a) $z = 1.0816$ meters (b) $z = 0.9286$ meters (c) $z = 0.7755$ meters (d) $z = 0.6224$ meters (e) $z = 0.4694$ meters (f) $z = 0.3163$ meters.
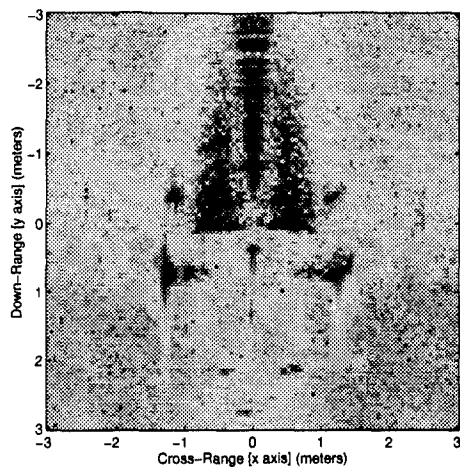
(a)
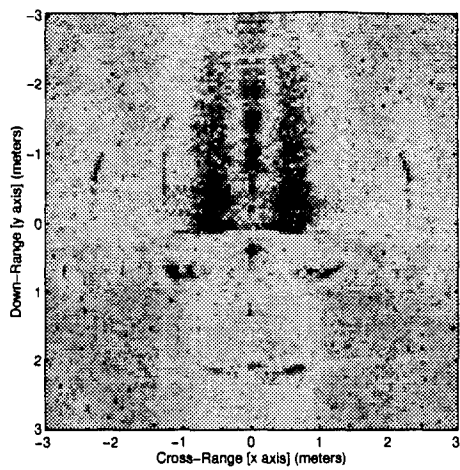
(b)
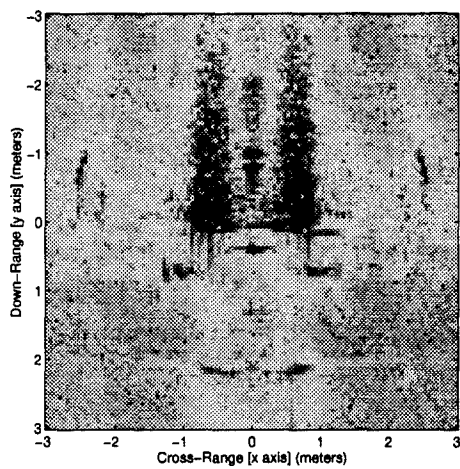
(c)
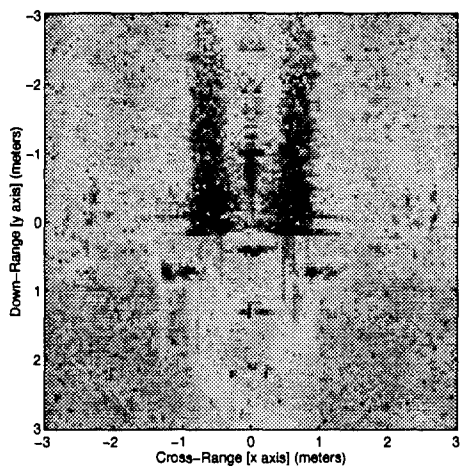
(d)
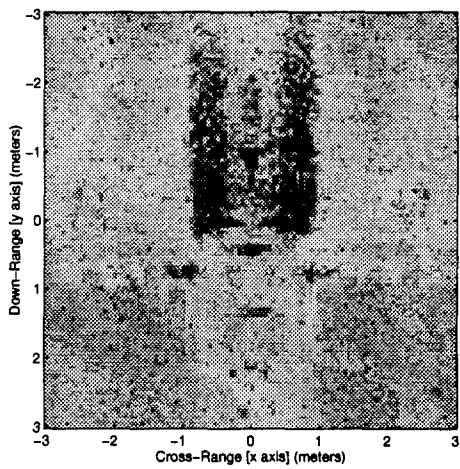
(e)

Figure 36.   Nose Data: xy plane slices at (a) $z = 0.1633$ meters (b) $z = 0.0102$ meters (c) $z = -0.1429$ meters (d) $z = -0.2959$ meters (e) $z = -0.4490$ meters.

xz slice at y=0.7311
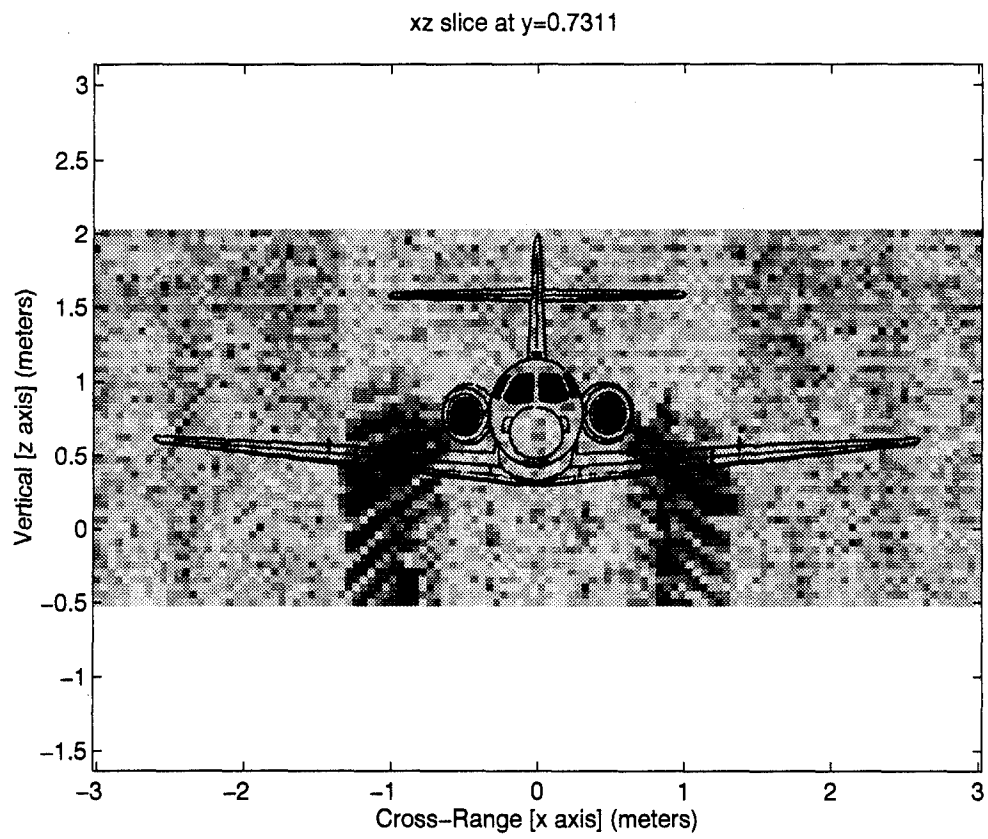
Figure 37. Nose Data: Slice in xz plane of landing lights scattering.

xz slice at y=0.2773
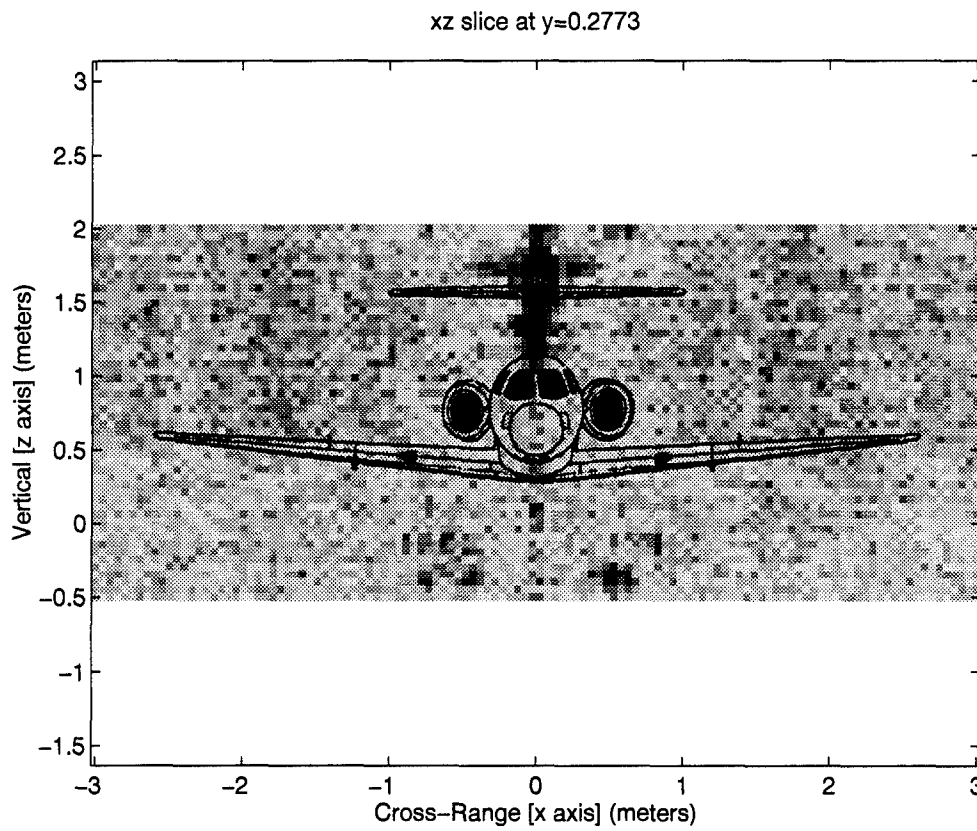
Figure 38. Nose Data: Slice in xz plane of APU intake scattering.

xz slice at y=-0.6303
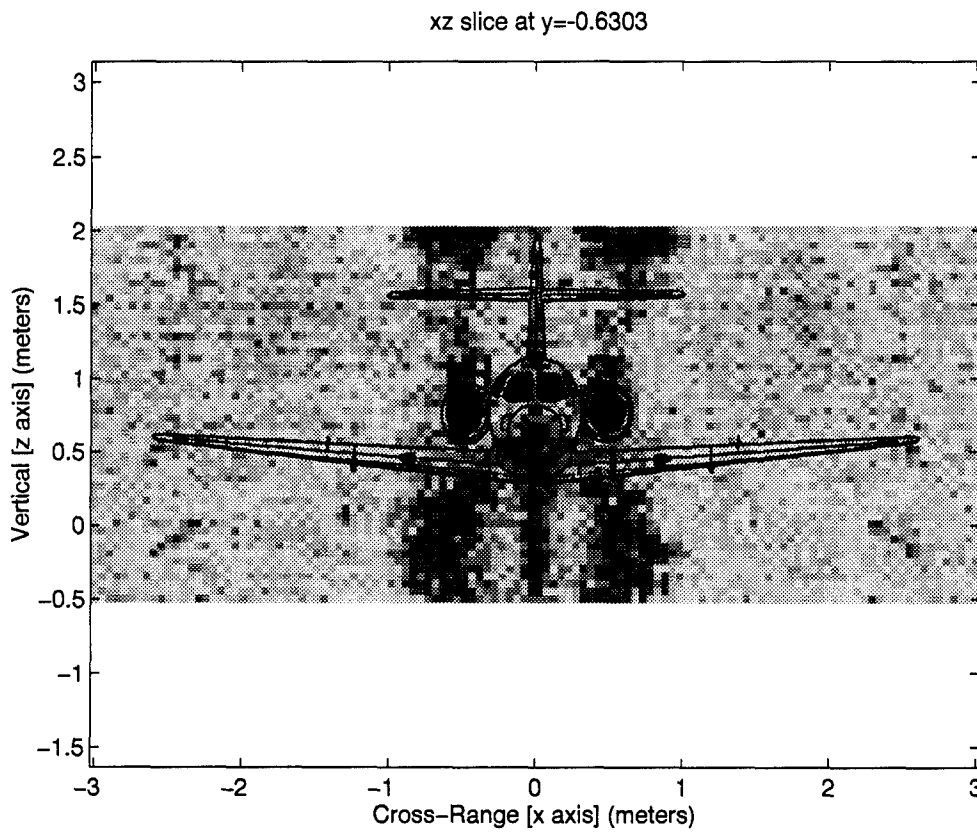
Figure 39. Nose Data: Slice in xz plane of engines scattering.

xy slice at z=0.4694
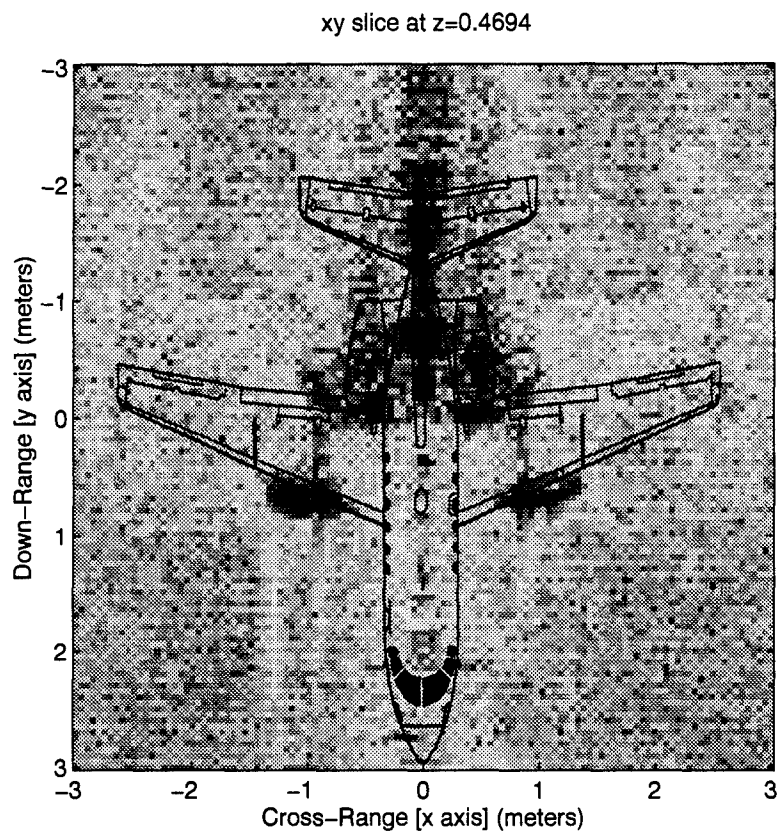
Figure 40. Nose Data: Slice in xy plane of landing lights scattering.

xy slice at z=0.7755
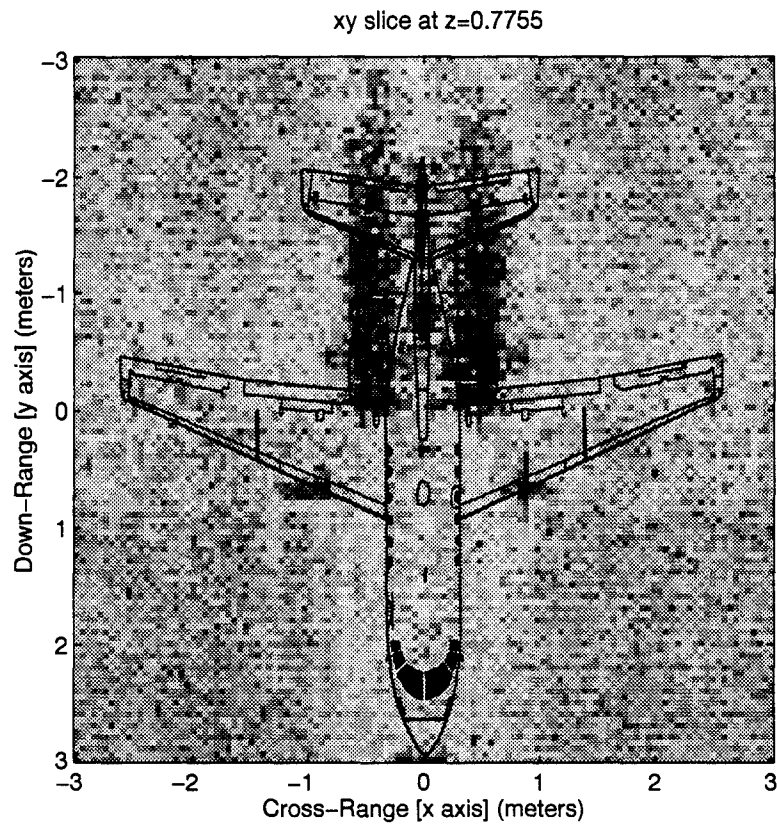
Figure 41. Nose Data:Slice in xy plane of engines scattering.

xy slice at z=1.2347
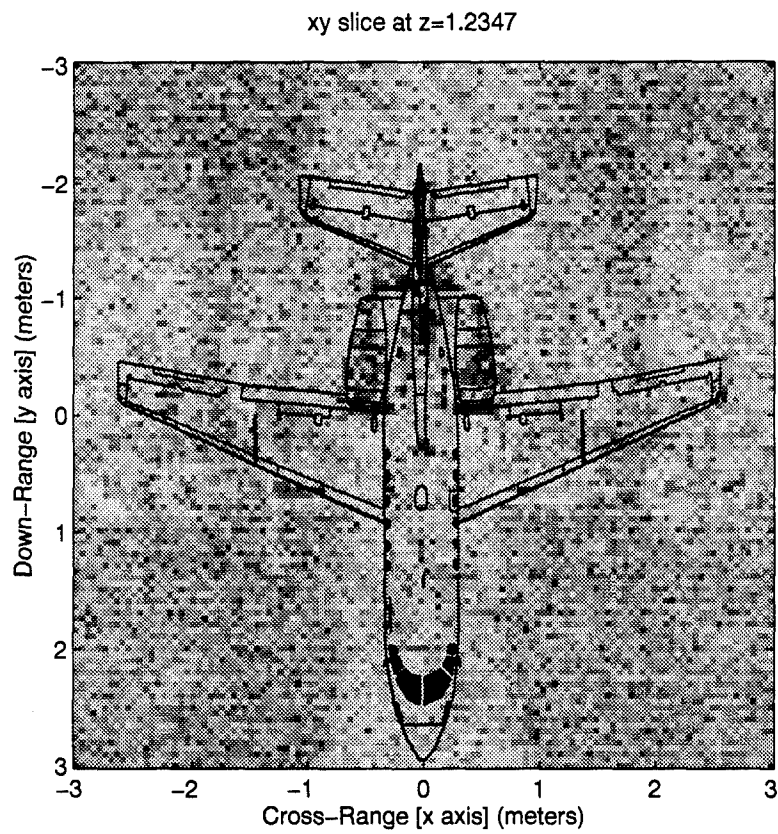
Figure 42. Nose Data: Slice in xy plane of APU intake scattering.

4.3 Wing Data

The wing data described in Figure 14 provides the most dramatic results. The HH polarization makes the pedestal less of a reflector. The 19° to 29° azimuth angles are normal to the leading edge of the right wing and leading edge of the right horizontal stabilizer. This angular range allows the wing and the horizontal stabilizer to be the major scatterers. Also, this makes it easy to see the vertical separation between the wing and the tail.

A volume consisting of 864,000 pixels was computed over the following dimensions,

$$-3.0 \text{ meters} \le x \le 3.0 \text{ meters} \quad \text{stepsize } \Delta x = 0.05 \text{ meters}$$
$$-3.0 \text{ meters} \le y \le 3.0 \text{ meters} \quad \text{stepsize } \Delta y = 0.05 \text{ meters}$$
$$-0.5 \text{ meters} \le z \le 2.5 \text{ meters} \quad \text{stepsize } \Delta z = 0.05 \text{ meters.}$$

Figure 43 is a top view of the iso-surface for this volume and shows reflections from the wing and horizontal stabilizer. Figure 44 shows the vertical separation of the wing and the horizontal stabilizer coincides with their physical location on the target. The reflections at the bottom of Figure 44 are caused by the pedestal.

Figures 45 through 51 are slices taken in the xz plane of the entire volume computed from the wing data. These slices are taken every 0.1513 meters going from front to back. Figures 52 through 55 are slices taken in the xy plane of the same volume. These slices are taken every 0.1525 meters from top to bottom. Figures 56 and 57 are expanded views of slices in the xy plane of the horizontal stabilizer and wing respectivly.

4.4 Conclusion

Images computed by utilizing the three-dimensional algorithm of Chapter 2 were presented in this chapter. The accuracy of this algorithm was verified by comparing iso-surface images as well as two-dimensional slices to the physical properties of the target. The images demonstrated that scattering primarily occurs at physical discontinuities on the target. In the case of the nose data, VV polarization was used causing surfaces with vertical edges, such as the pedistal, to be dominant scatterers. Since HH polarization was used for the wing

59
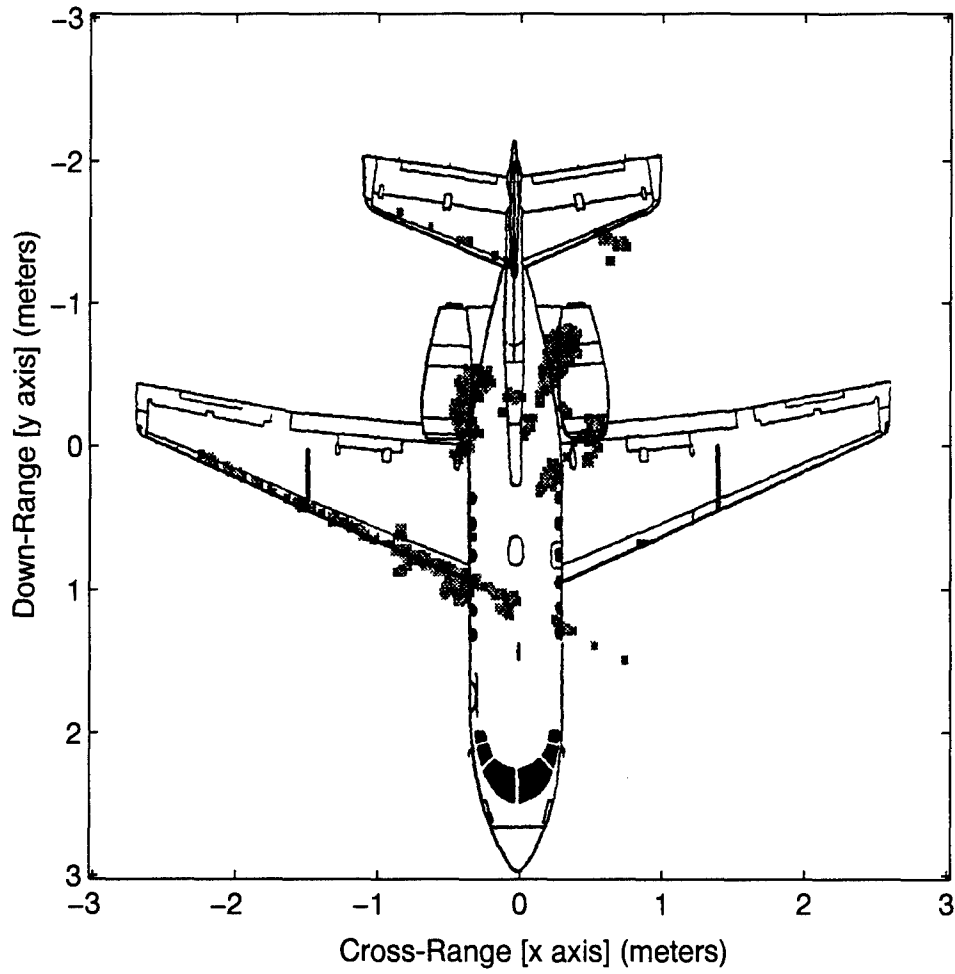
Figure 43. Top view of iso-surface from wing data.
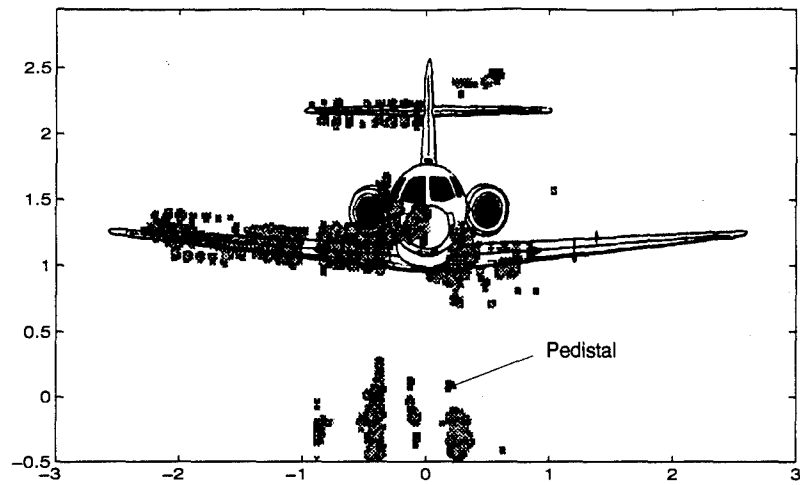
Figure 44. Front view of iso-surface from wing data.

data, surfaces with horizontal edges are the dominant scatterers. This combined with azimuth angles normal to the wing and horizontal stabilizer's leading edge cause these "edges" to be the dominant scatterers.
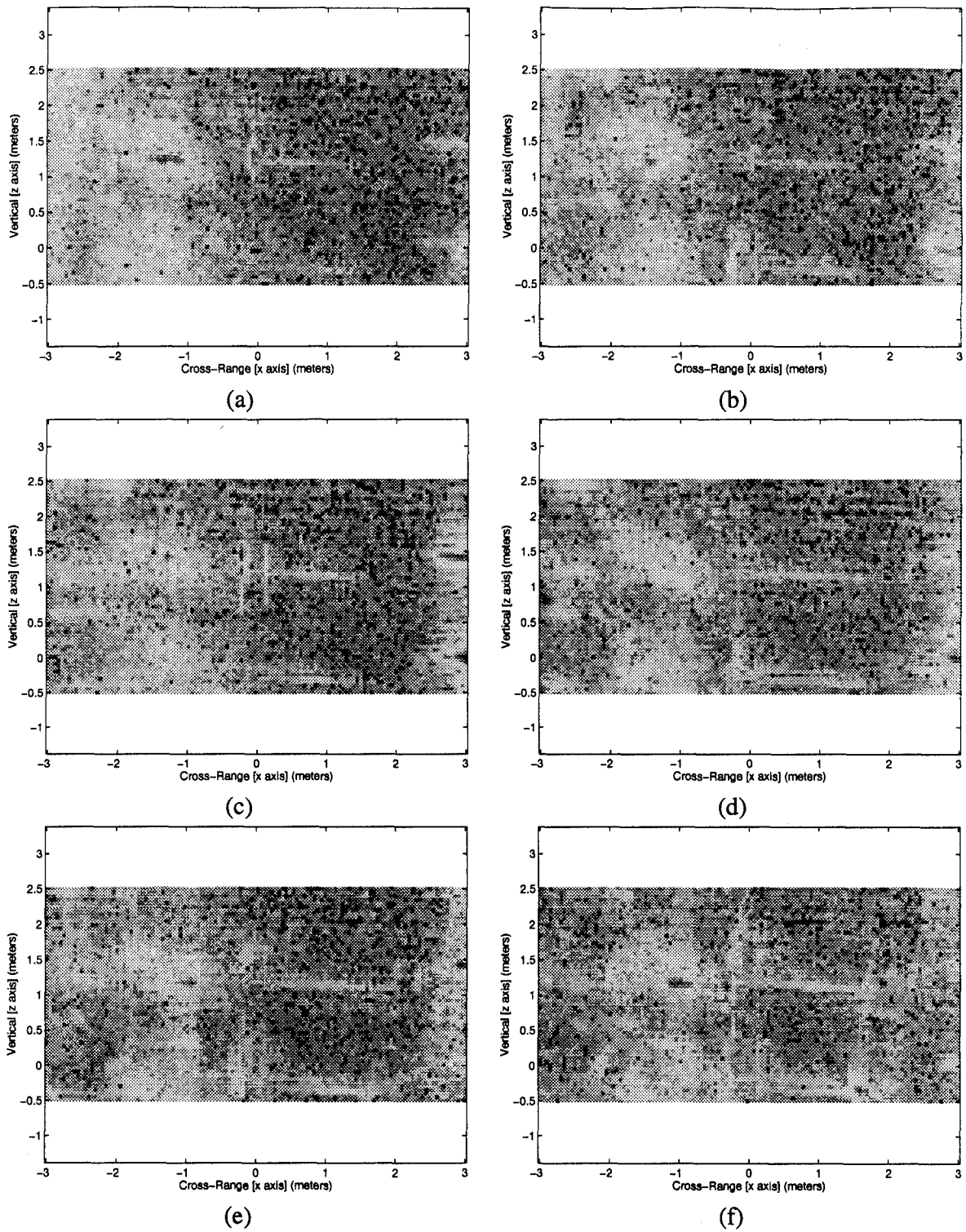
Figure 45.   Wing Data: xz plane slices at (a) $y = 3.0000$ meters (b) $y = 2.8487$ meters (c) $y = 2.6975$ meters (d) $y = 2.5462$ meters (e) $y = 2.3950$ meters (f) $y = 2.2437$ meters.

62
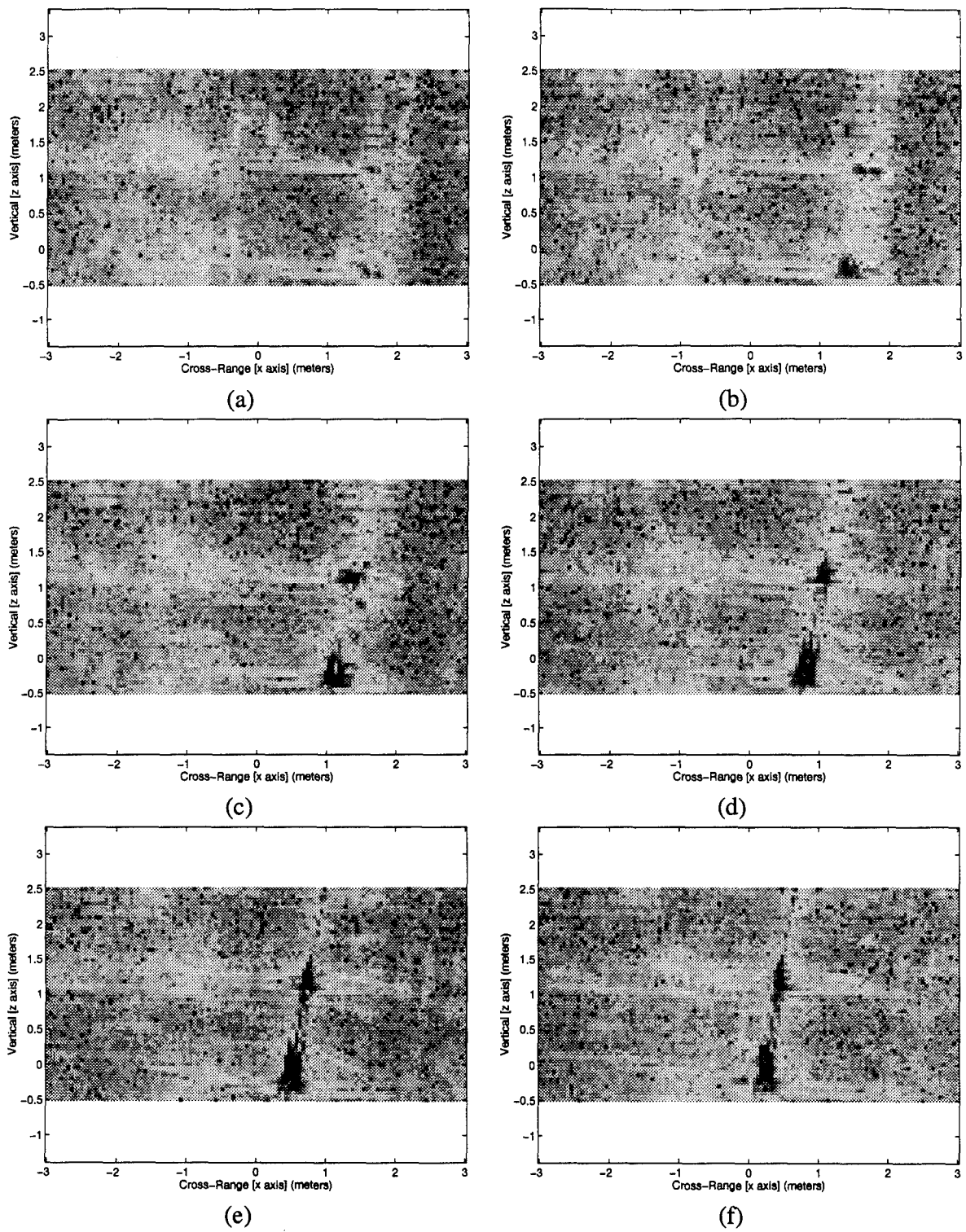
Figure 46.   Wing Data: xz plane slices at (a) $y = 2.0924$ meters (b) $y = 1.9412$ meters (c) $y = 1.7899$ meters (d) $y = 1.6387$ meters (e) $y = 1.4874$ meters (f) $y = 1.3361$ meters.
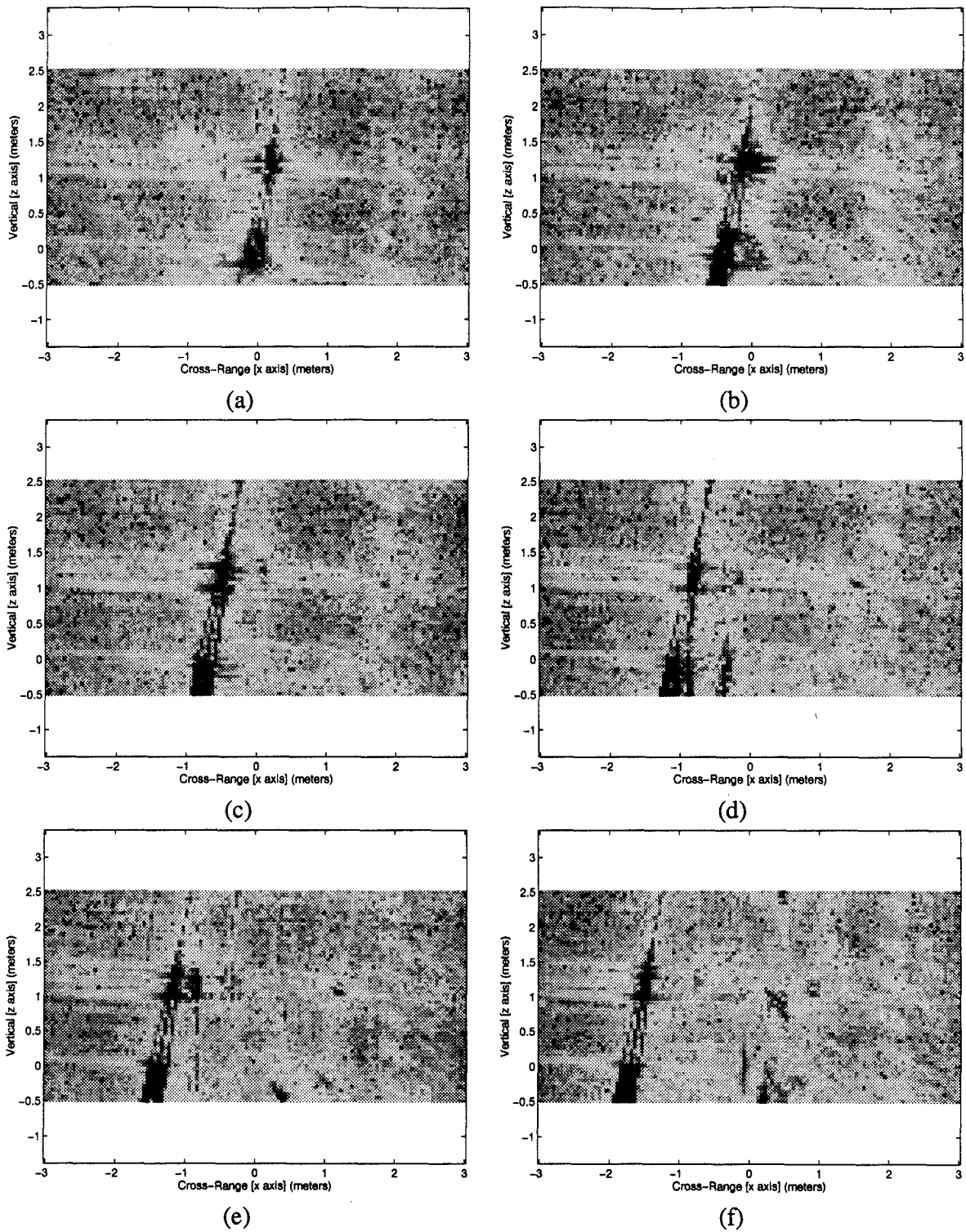
Figure 47. Wing Data: xz plane slices at (a) $y = 1.1849$ meters (b) $y = 1.0336$ meters (c) $y = 0.8824$ meters (d) $y = 0.7311$ meters (e) $y = 0.5798$ meters (f) $y = 0.4286$ meters.
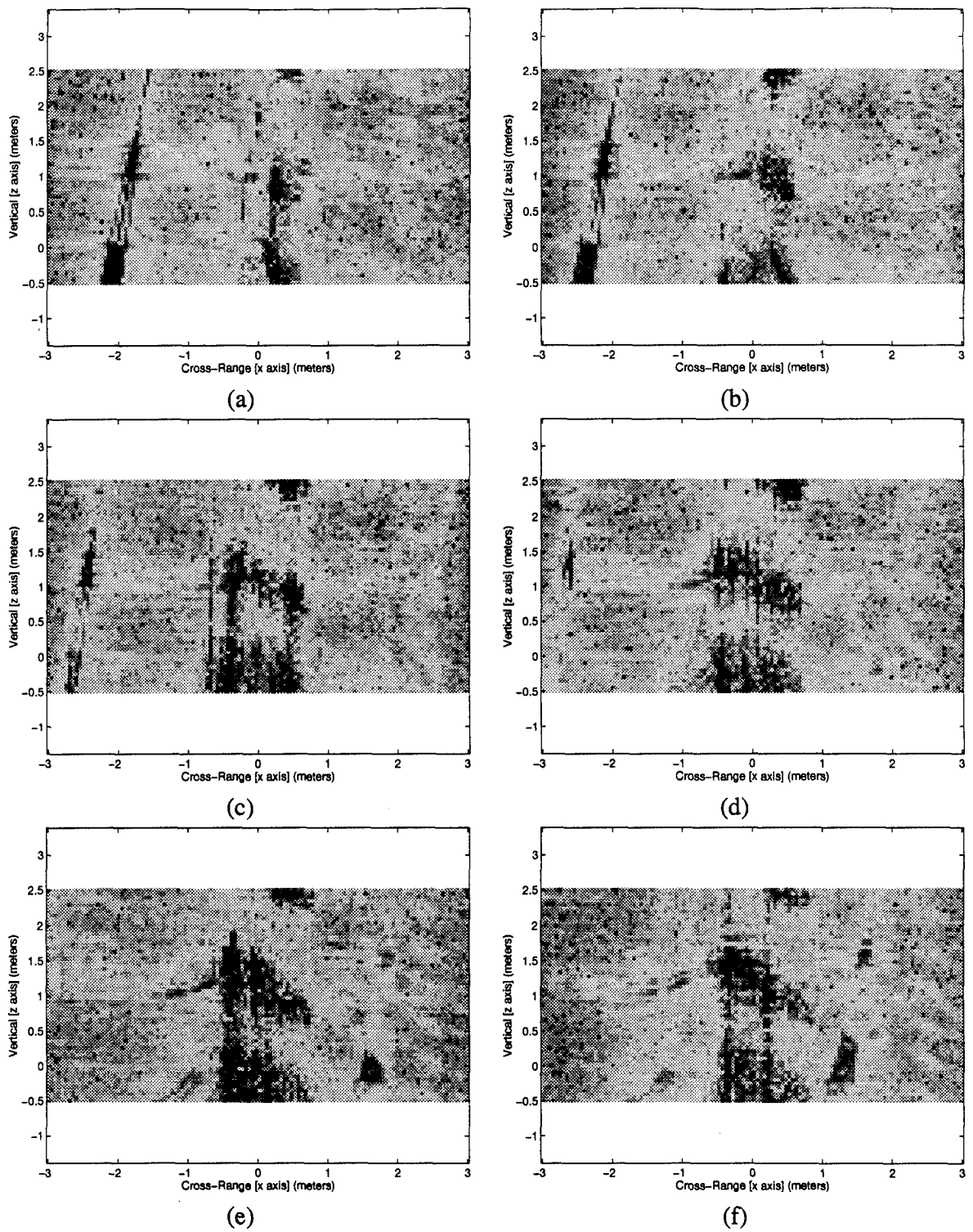
Figure 48. Wing Data: xz plane slices at (a) $y = 0.2773$ meters (b) $y = 0.1261$ meters (c) $y = -0.0252$ meters (d) $y = -0.1765$ meters (e) $y = -0.3277$ meters (f) $y = -0.4790$ meters.

65
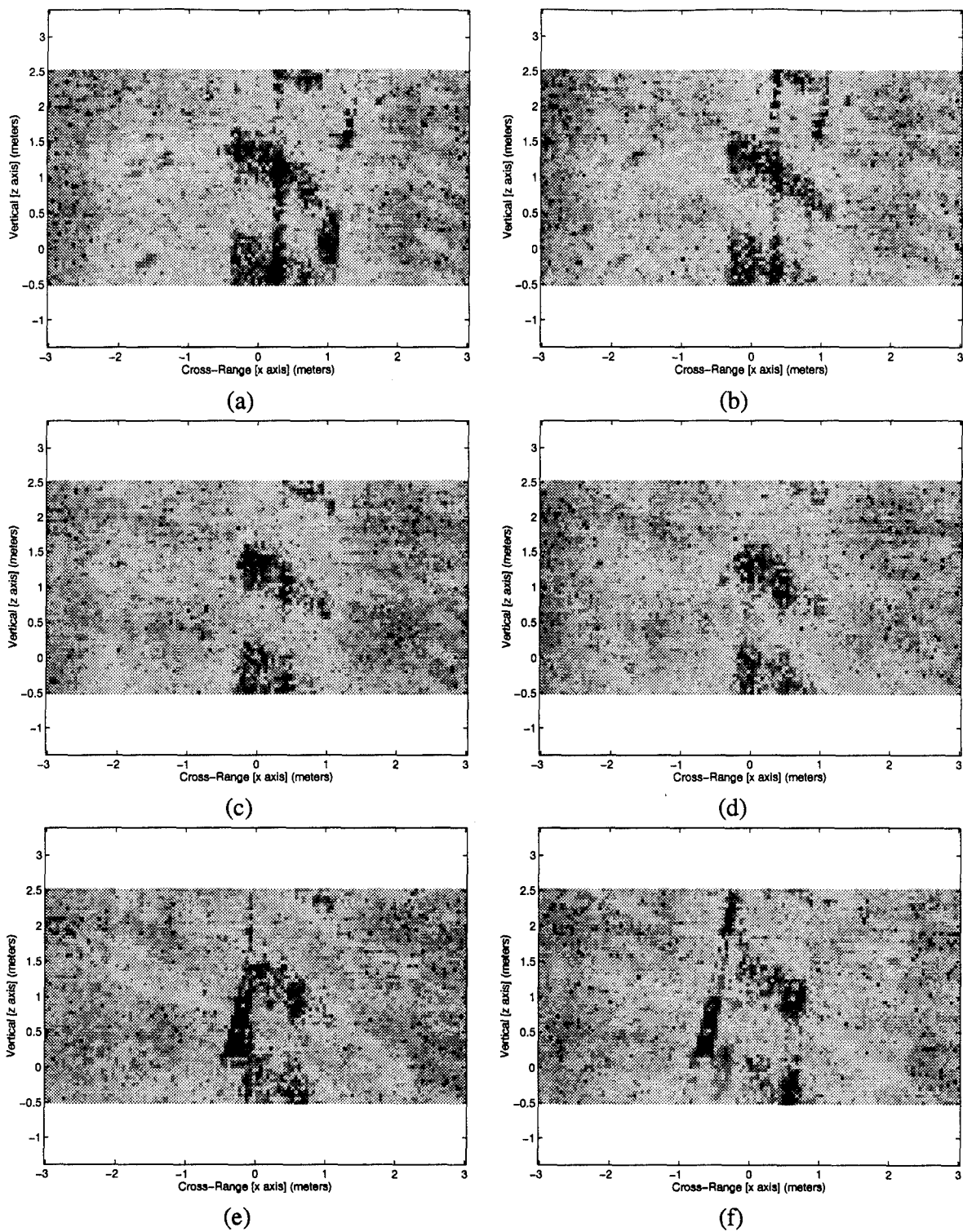
Figure 49.   Wing Data: xz plane slices at (a) $y = -0.6303$ meters (b) $y = -0.7815$ meters (c) $y = -0.9328$ meters (d) $y = -1.0840$ meters (e) $y = -1.2353$ meters (f) $y = -1.3866$ meters.
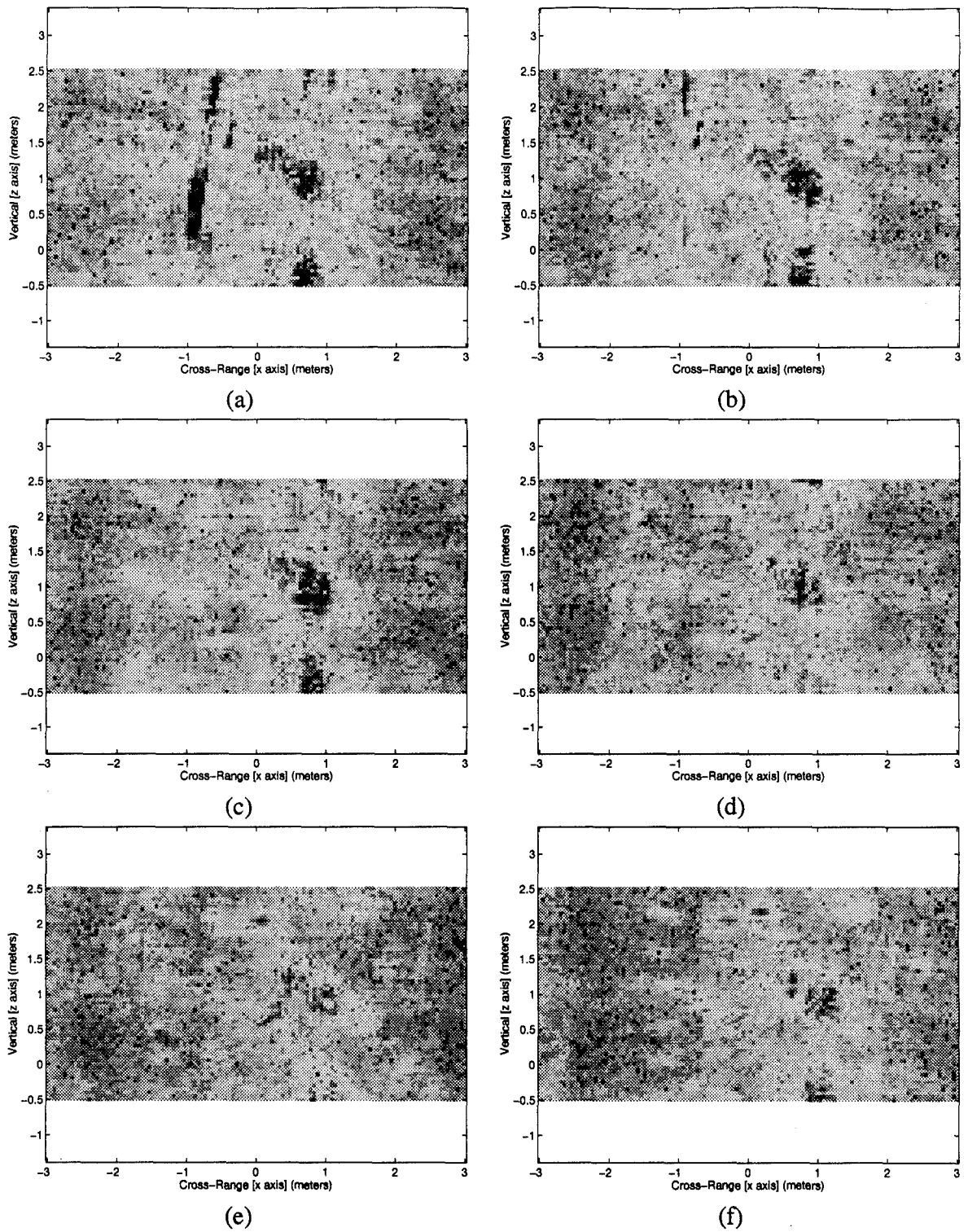
Figure 50. Wing Data: xz plane slices at (a) $y = -1.5378$ meters (b) $y = -1.6891$ meters (c) $y = -1.8403$ meters (d) $y = -1.9916$ meters (e) $y = -2.1429$ meters (f) $y = -2.2941$ meters.
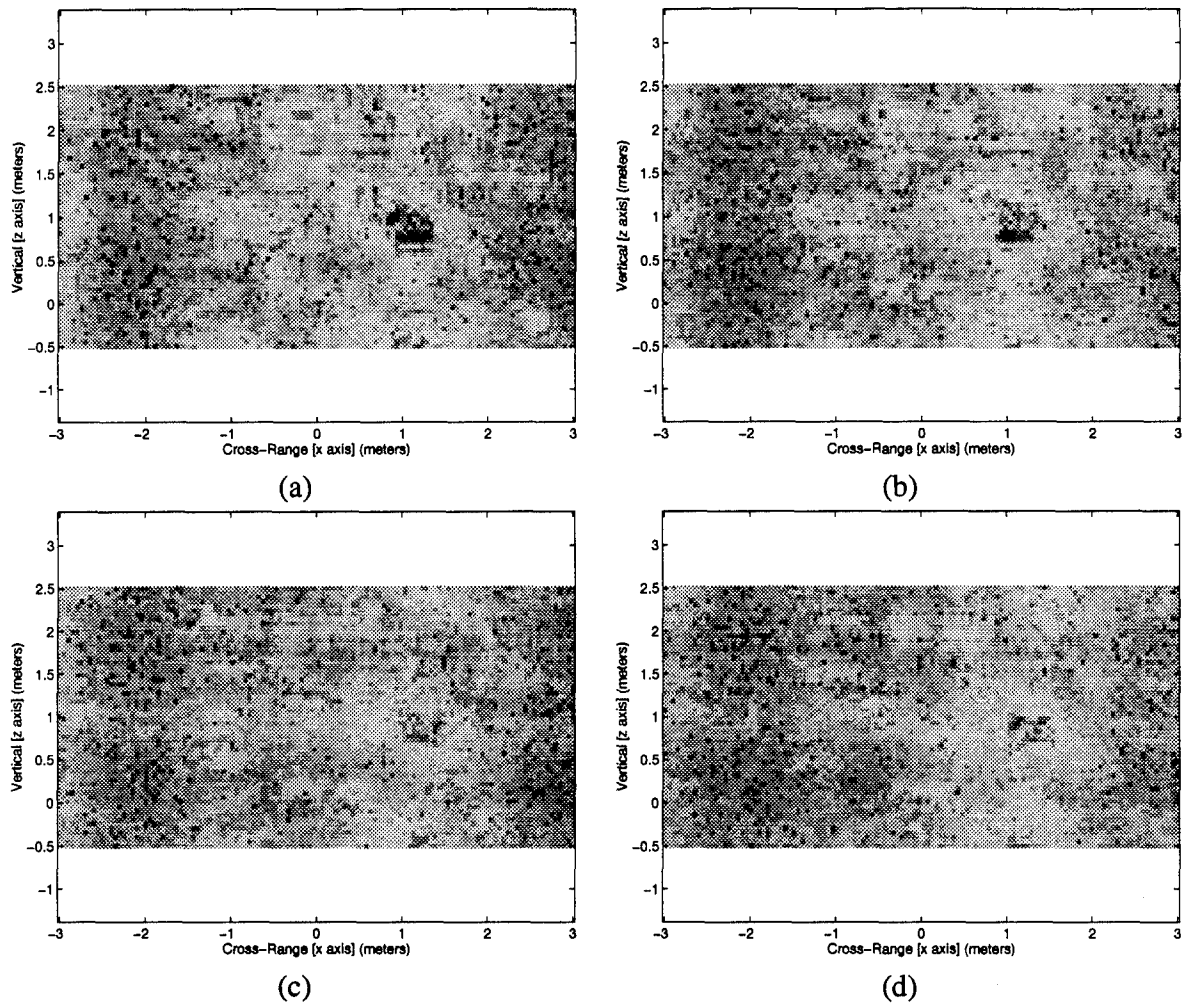
Figure 51.   Wing Data: xz plane slices at (a) $y = -2.4454$ meters (b) $y = -2.5966$ meters (c) $y = -2.7479$ meters (d) $y = -2.8992$ meters.
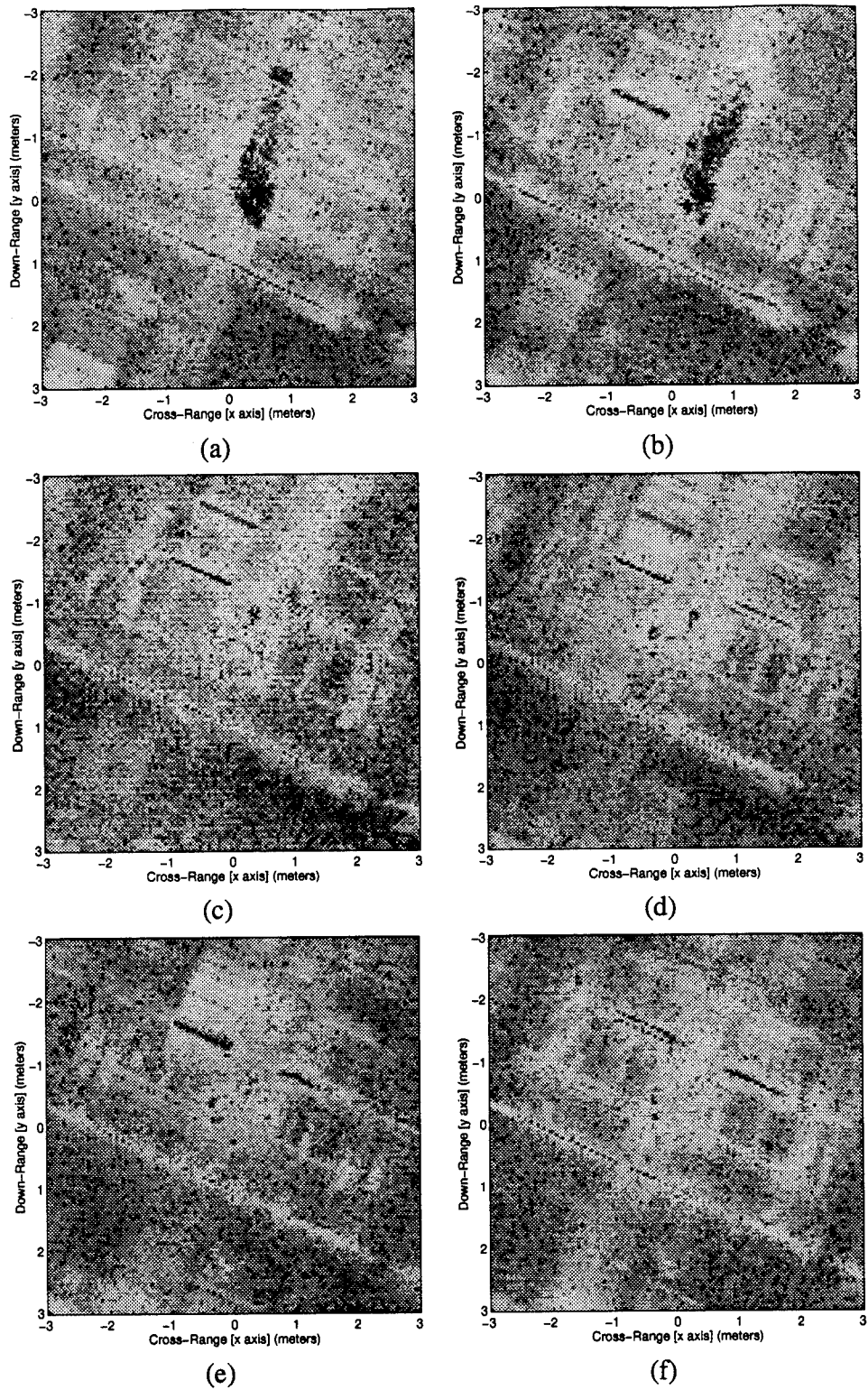
Figure 52. Wing Data: xy plane slices at (a) $z = 2.5000$ meters (b) $z = 2.3475$ meters (c) $z = 2.1949$ meters (d) $z = 2.0424$ meters (e) $z = 1.8898$ meters (f) $z = 1.7373$ meters.

69
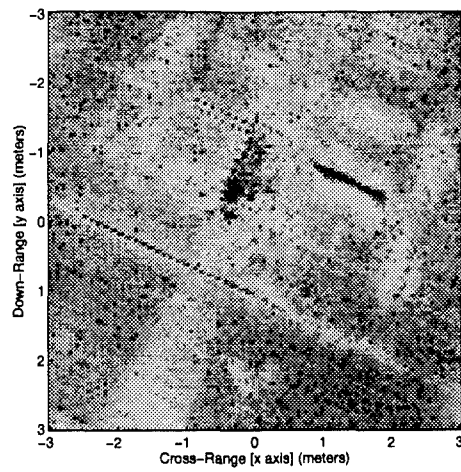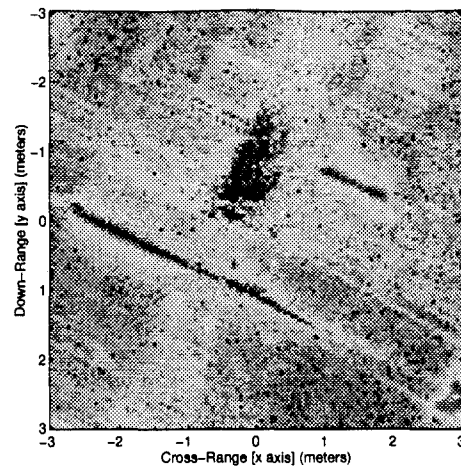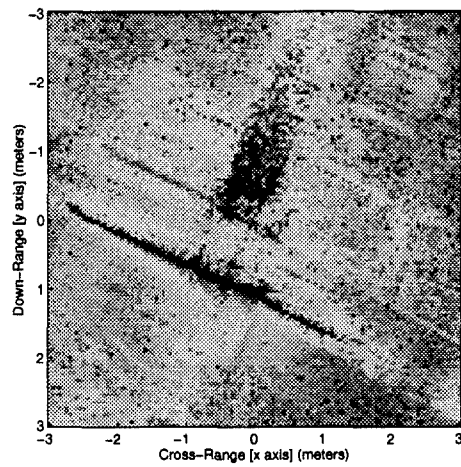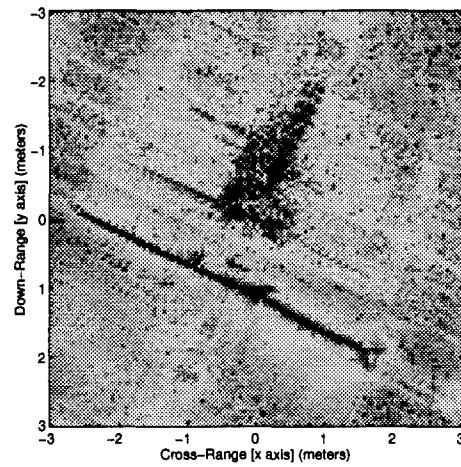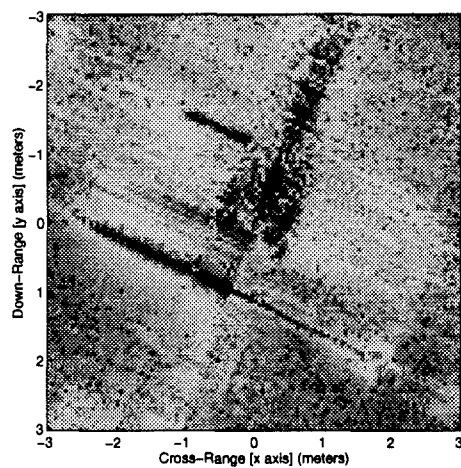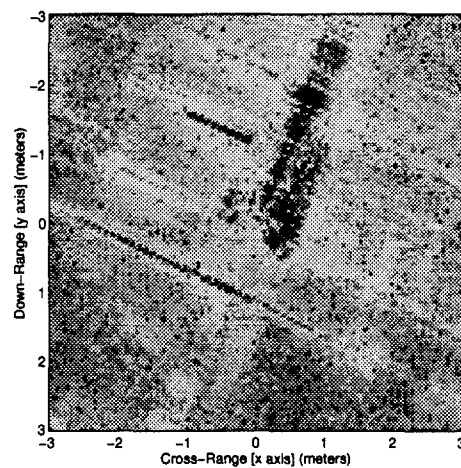
Figure 53. Wing Data: xy plane slices at (a) $z = 1.5847$ meters (b) $z = 1.4322$ meters (c) $z = 1.2797$ meters (d) $z = 1.1271$ meters (e) $z = 0.9746$ meters (f) $z = 0.8220$ meters.

70
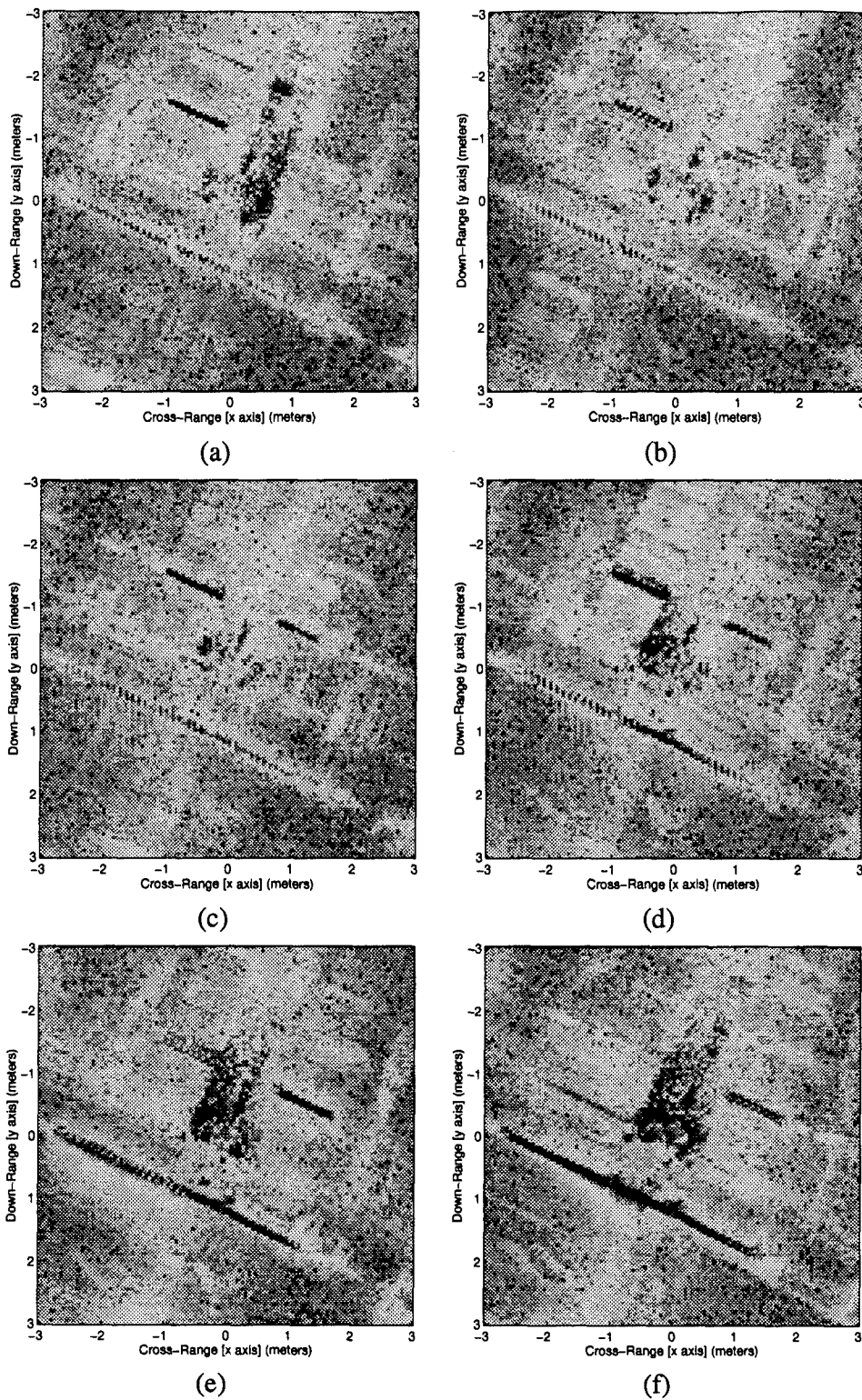
Figure 54. Wing Data: xy plane slices at (a) $z = 0.6695$ meters (b) $z = 0.5169$ meters (c) $z = 0.3644$ meters (d) $z = 0.2119$ meters (e) $z = 0.0593$ meters (f) $z = -0.0932$ meters.

71

(a)　　　　　　　　　　　　　(b)
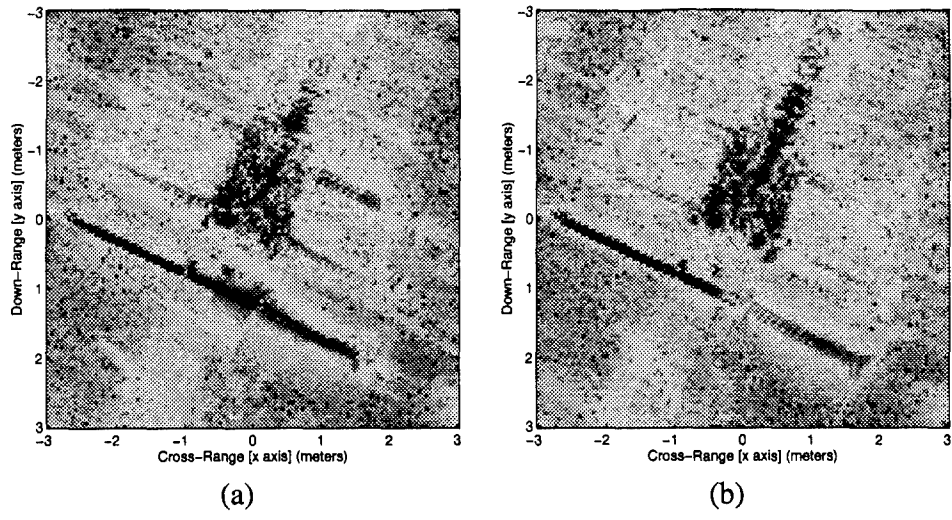
Figure 55. Wing Data: xy plane slices at (a) $z = -0.2458$ meters (b) $z = -0.3983$ meters.

xy slice at z=2.1949 meters
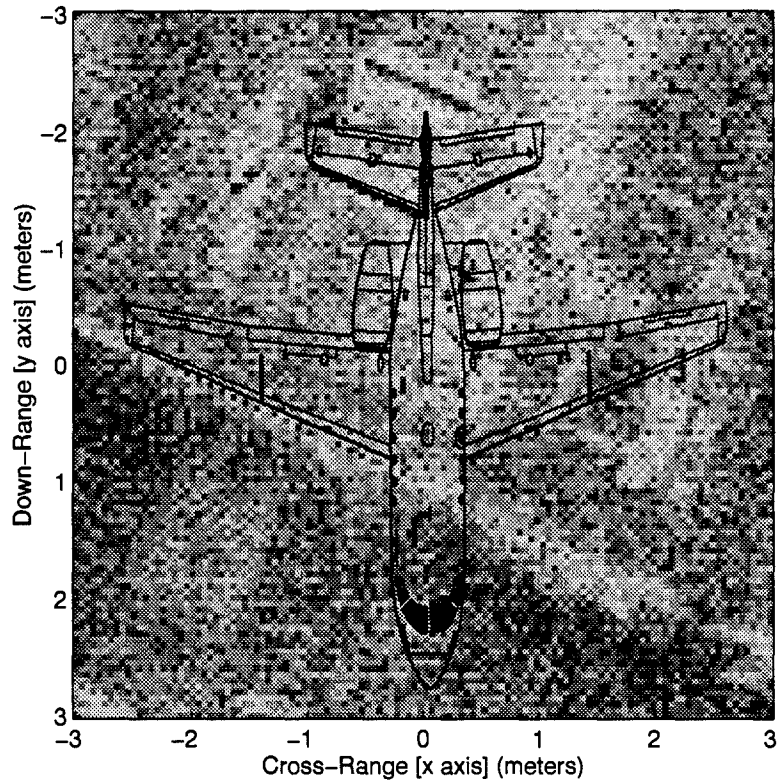
Figure 56. Wing Data:Slice in xy plane of horizontal stabilizer scattering.

72

xy slice at z=1.2797 meters
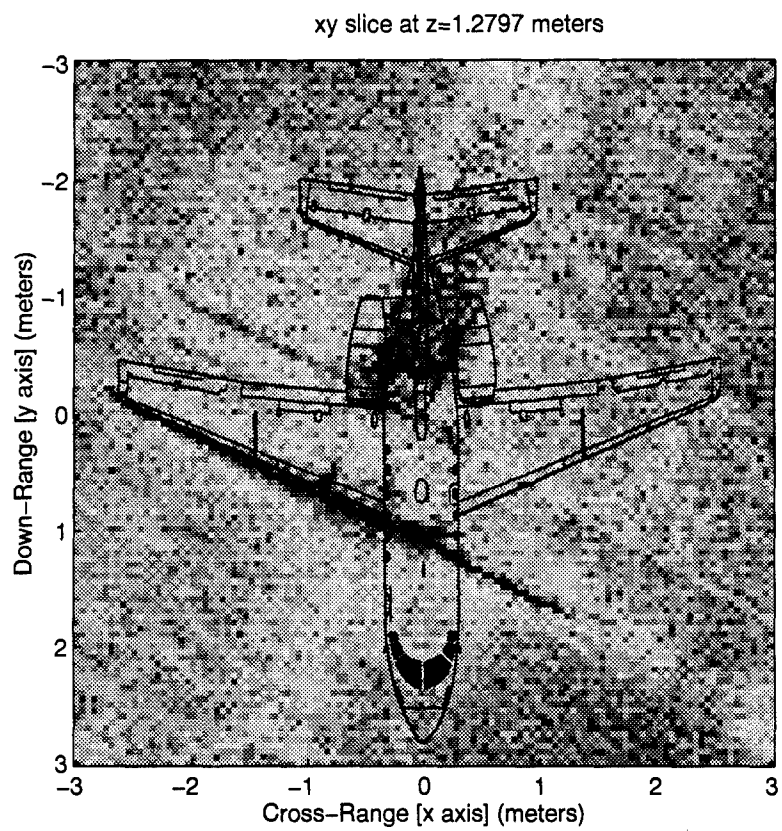
Figure 57. Wing Data: Slice in xy plane of wing scattering.

V. Conclusions

5.1 Summary of Work

In Chapter 2, basic radar imaging theory was presented from its basic principles through two-dimensional Filtered Back-Projection. With this basis in hand, three-dimensional Filtered Back-Projection was then developed and translated into a discrete algorithm. Chapter 3 presented the C-29 one-third scale model used to generate data for this research as well as two series of three-dimensional radar measurements taken by Wright Laboratory. The methodology used to convert these radar measurements into actual radar images was recounted while some of the obstacles confronted in this process were touched on. The results were presented in Chapter 4. Iso-surface images were presented from different view angles and two-dimensional slices were included of the major scattering features.

5.2 Discussion of Results

This research demonstrates the ability to produce accurate three-dimensional images given three-dimensional radar data. The major problem confronted in this research was the lack of memory available in terms of both hard drive space and RAM. This problem limited the amount of up sampling allowed when computing the projections and ultimately led to inferior resolution as well as spurious responses in the final image. Theoretically, sufficient resolution should have been available without upsampling the original data as shown in Equation 43. However, due to accumulated error caused by summing the numerous projections, large errors resulted in the final image. In order to reduce this effect, up sampling as well as the interpolation step described in Equation 40 was necessary (1). It was determined through trail and error that at the least, up sampling by a factor of 6 for the nose data and 7 for the wing data produced a minimumly acceptable image. Using a factor below those given above resulted in poor image quality as shown in Figure 15. Ideally, up sampling by a factor of 20, as was used in Anderson's two-dimensional research (1), would produce excellent image quality but would result in a dataset far to large to work with for three-dimensional imaging. However,

74

it is still obvious from the images shown in Chapter 4 that this three-dimensional algorithm produces accurate scatterer location in the z dimension. If sufficient memory were available to up sample at a higher rate much better resolution can be achieved in the resulting image. The most dramatic results were produced using the wing data. It is clear by viewing Figure 44 that a true three dimensional representation of the target was computed.

5.3   Recommendations for Future Research

Primarily, any future work in the area of three-dimensional imaging should be focused on reducing the memory requirements of computing an image. Inherently the "raw" three-dimensional radar data will require extremely large storage space. The aforementioned need to up sample the projection data causes a multitudinous increase in storage space requirements over this original data. It would be of great benefit to look into an alternative method of interpolation other than up sampling. One possibility is illustrated in Oppenheim and Shafer (9). The process of up sampling is equivalent to applying an ideal low-pass filter in the frequency domain or convolving with a sinc function in the time domain. The use of a convolution to determine the interpolated values eliminates the need to up sample. But care should be taken not hinder the computational speed of computing a pixel in the process. The fact that such a high number of pixels need to be computed to obtain a useful image, for example 864,000 pixels for the nose data in this research, even a small decrease in computational speed could cause a large increase in the time required to compute a volume of pixels.

Additional research can possibly be done in the area of artificially extending the bandwidth of the radar data through the use of parametric methods. This process would effectively remove any noise in the computed projections and possibly produce a clearer image in the end.

Appendix A. Computer Code

This appendix contains the computer code used to compute the images in this research. Section A.1 contains the code that computes the filtered projections and stores them according to elevation angle in Matlab .mat files. Section A.3 converts the .mat files to an 3-D unformatted fortran array. Section A.4 contains the code that actually computes the 3-D volume from the filtered projections.

A.1   projection.m

```
%
%               File: projection.m
%               Author: Jack D. Pullis
%               Purpose: Compute filtered projections on raw radar data and store
%                        according to elevation angle.
%
%
%
f= [26002300:20000:36002300]*10^3;

ph=[4.92:.08:6.04];

c=3e8;                        % speed of light
m=7;                          % oversample factor
df=abs(f(2)-f(1));            % calculate delta-f
dth=abs(th(2)-th(1));         % calculate delta-theta
dph=abs(ph(2)-ph(1));         % calculate delta-phi

for el=1:length(ph);

E=num2str((30-ph(el))*100);
file=['C29_3D_hhN.0',E];
fid=fopen(file);
buf=fread(fid,[2008,251],'float32');
fclose('all')
G=buf(7:2:2008,:)+j*buf(8:2:2008,:);
[M,V]=size(G);
M=501;
Ru=0.5*c/df;                  % calculate the unambiguous range
dr=Ru/(m*M);                  % calculate the range resolution
r=(0:m*M-1)*dr;               % form the downrange vector


filt=cos(ph(el)*(180/pi))*((f(:).^2)*ones(1,V)); % calculate imaging filter
corr=exp(j*4*pi*f(1)*r'/c)*ones(1,V);            % shift to baseband for IFFT
rc=corr.*ifft(G(1:2:1001,:).*filt,m*M);          % compute filtered projections

for ci=1:V;
rc(:,ci)=fftshift(rc(:,ci));
end

E2=num2str(ph(el));
file2=['/home/marconil/c29/C_29_3D_hhNel',E2]

eval(['save ' file2 ' rc'])    % store projections in elevation file
```

```
end




A.2   convert.f

c
c             file: convert.f
c            author: Jack D. Pullis
c           purpose: Convert .mat files containing filtered projections
c                    to a unformated fortran 3-D array then save it
c
c
c
c---------------------------------------------------------------------------
character*50 fil1,file1
complex*8  rc(3006,251,37)
complex*16 r(754506)
real*4 ph(34)
        integer*4 fp,matOpen,p
        integer mn, stat
        integer*4 matGetMatrix
        integer mxGetM, mxGetn, matClose
c---------------------------------------------------------------------------

fil1='/home/marconi1/c29/Binproj/datahn2.all'

open(unit=55,file=fil1,form='unformated',status='unknown')

ph(1)=3.00
do 20 I=2,37
ph(I)=ph(I-1)+.08
  20  continue                                            /


do 10 I=1,37

open(unit=52, status='scratch')
write(52,11) '/home/marconi1/c29/C_29_3D_hhNe1', ph(I)

rewind(unit=52)
read(52,12) file1
  11    format(A32,F4.2)
  12 format(A36)
close(52)

write(6,*) file1

        fp = matOpen(file1, 'r')

p = matGetMatrix(fp, 'rc')

        mn = mxGetM(p) * mxGetN(p)
        call mxCopyPtrToComplex16(mxGetPr(p), mxGetPi(p), r, mn)
        stat = matClose(fp)
        call mxFreeMatrix(p)

write(6,*) mn
do 30 K=1,251
do 40 J=1,3006

indx=indx+1
  rc(J,K,I)=r(indx)
```

```
   40 continue
   30 continue

indx=0

   10  continue

write(55) rc
close(55)

end



A.3   image3d.f

c
c              file: image3d.f
C             author: Jack D. Pullis
c            purpose: Compute 3-D Filtered Back-Projection volume from
c                     pre-stored projection file named data.all. The resulting
c                     data is stored in a Matlab .mat file under the name
c                     rdata.mat
c
c
c
c------------------------------------------------------------------------------
dimension ph(101),th(251),f(501),st(251)
dimension x(90),y(90),z(5),v(251),ct(521),sph(101),cph(101)
real *4 ph
integer mn, stat,inc,inc1,rl,inc2,Q,indx,13
        integer fp,matOpen,p,mxCreateFull
        complex *8 rc(3507,251,37),cum
complex *16 data(40500)
        integer  matClose
character*50 file1,file2

complex*8 rc1(3006,251,19),rc2(3006,251,18)
character*50 fil1,fil2,fil3


c------------------------------------------------------------------------------
c
c         Load Projection data
c
c------------------------------------------------------------------------------

fil1='/home/fish1/jsacchin/data.all'

open(unit=55,file=fil1,form='unformated',status='unknown')
read(55) rc1
close(55)


c------------------------------------------------------------------------------
c
c         Load parameter data
c
c------------------------------------------------------------------------------

c=3e8
open(unit=1,file='outtest.dat',status='old')
read(1,*) ph,th,f,x,y,z

ml=6
nth=251
```

```
   nph=101
M=501
nx=90
ny=90
nz=1
df=abs(f(2)-f(1))
dth=abs(th(2)-th(1))
dph=abs(ph(2)-ph(1))
Ru=0.5*c/df
dr=Ru/(m1*M)

do 20 I=1,nth
   radi=th(I)*(3.14/180)

  st(I)=sin(radi)
  ct(I)=cos(radi)

  20 continue

do 30 I=1,nph
  sph(I)=sin(ph(I)*(3.14/180))
  cph(I)=cos(ph(I)*(3.14/180))
  30 continue


c------------------------------------------------------------------------
c
c           Compute each pixel
c
c------------------------------------------------------------------------

do 40 zi=1,nz
  do 50 xi=1,nx
do 60 yi=1,ny
cum=(0.0 , 0.0)
inc=0
  do 70 l=1,73,2
     inc=inc+1
     zscal=sph(l)

     do 75 l2=1,nth
     xscal=st(l2)*cph(l)
     yscal=ct(l2)*cph(l)


    v(l2)=x(xi)*xscal+y(yi)*yscal+z(zi)*zscal
  75      continue


     do 76 l3=1,nth

     rp=v(l3)/dr+1+(M*m1)/2
     rl=int(rp)

cum=cum+(rl+1-rp)*rc(rl,l3,inc)+(rp-rl)*rc(rl+1,l3,inc)

  76      continue


  70  continue
data(yi+((xi-1)*ny)+(zi-1)*ny*nx)=cum
   60 continue
  write(6,*) xi,zi
  50 continue
  40 continue
```

79

```
fp = matOpen('rdata.mat', 'w')

p = mxCreateFull(nx*ny, nz, 1)
call mxCopyComplex16ToPtr(data, mxGetPr(p), mxGetPi(p), nz*nx*ny)
call mxSetName(p, 'R')
stat = matPutMatrix(fp, p)
stat = matClose(fp)
call mxFreeMatrix(p)

end
```

Bibliography

1. Anderson, B. P. and J. J. Sacchini. "A Comparison of Stepped Continuous-Wave Radar Imaging Algorithms." *Proceedings of the IEEE 1994 Nataional Aerospace and Electronics Conference.* 303–308. May 1994.

2. Censor, Y. "Finite Series-Expansion Reconstruction Methods," *Proceedings of the IEEE, 71*(3):409–419 (March 1983).

3. Delaney, A. H. and Y. Bresler. "A Fast Iterative Tomographic Reconstruction Algorithm." *Proceedings of the IEEE 1995 International Conference of Acoustics, Speech, and Signal Processing.* 2295–2298. May 1995.

4. Dudgeon, D. E. and R. M. Mersereau. *Multidimensional Digital Signal Processing.* Prentice-Hall Signal Processing Series, Prentice-Hall, Inc, 1984.

5. Forsythe, George E., et al. *Computer Methods for Mathematical Computation.* Prentice-Hall Series in Automatic Computation, Englewood Cliffs, NJ 07637: Prentice-Hall, Inc, 1977.

6. Kay, S. M. *Modern Spectral Estimation.* Englewood Cliffs, NJ: Prentice-Hall, 1988.

7. Lewitt, R. M. "Reconstruction Algorithms: Transform Methods," *Proceedings of the IEEE, 71*(3):390–408 (March 1983).

8. Mensa, D. L. *High Resolution Radar Cross Section Imaging.* Artech House, 1991.

9. Oppenheim, A. V. and R. W. Schafer. *Discrete-Time Signal Processing.* Englewood Cliffs, NJ: Prentice Hall, 1989.

10. Research Systems, Inc. *IDL Basics,* November 1992.

11. Sacchini, J. J., et al. "Two-Dimensional Prony Modeling and Parameter Estimation," *IEEE Transactions on Signal Processing, 41*(11):283–291 (November 1993).

Captain Jack D. Pullis ██

He graduated from DePaul Diocesian High School in 1984 and entered undergraduate studies at Stevens Institute of Technology in Hoboken, New Jersey. In May 1988, he Graduated from Stevens with a Bachelor of Engineering Degree in Electrical Engineering and was commissioned as a Second Lieutenant in the USAF. His first assignment was at Columbus AFB, MS for pilot training. In August 1990, he was assigned to Pope AFB, NC where he performed in numerous world-wide operations as a C-130 pilot. In May 1994, he entered the School of Engineering, Air Force Institute of Technology.

1. AGENCY USE ONLY (Leave blank)	2. REPORT DATE December 1995	3. REPORT TYPE AND DATES COVERED Master's Thesis

4. TITLE AND SUBTITLE	5. FUNDING NUMBERS
Three Dimensional Inverse Synthetic Aperture Radar Imaging	

6. AUTHOR(S)

Jack D. Pullis
Captain, USAF

7. PERFORMING ORGANIZATION NAME(S) AND ADDRESS(ES) Air Force Institute of Technology, WPAFB OH 45433-6583	8. PERFORMING ORGANIZATION REPORT NUMBER AFIT/GE/ENG/95D-21

9. SPONSORING / MONITORING AGENCY NAME(S) AND ADDRESS(ES) Capt. Richard Jernasick Radar Target Scatter Division 6585 Test Group/RX Holloman AFB, NM 88330-5000	10. SPONSORING / MONITORING AGENCY REPORT NUMBER

11. SUPPLEMENTARY NOTES

12a. DISTRIBUTION / AVAILABILITY STATEMENT Approved for public release; Distribution Unlimited	12b. DISTRIBUTION CODE

13. ABSTRACT (Maximum 200 words)

This research investigates the generation, display, and interpretation of three-dimensional (3-D) Synthetic Aperture Radar images. Three-dimensional assumes that the data collected consists of one temporal dimension and two orthogonal angular dimensions. From this data, a three dimensional reflectivity map, or 3-D image, of a target can be constructed. This thesis effort develops and applies a three-dimensional imaging algorithm on actual radar data measured on an $\frac{1}{3}$ scale model of a C-29 aircraft. Two-dimensional slices of the three-dimensional image as well as three-dimensional isosurfaces are compared to the physical properties of the target. The results demonstrate the ability to produce three-dimensional images given three-dimensional radar data.

14. SUBJECT TERMS SAR, Imaging, Three-Dimensional Imaging, Filtered Back-Projection	15. NUMBER OF PAGES 94
	16. PRICE CODE

17. SECURITY CLASSIFICATION OF REPORT UNCLASSIFIED	18. SECURITY CLASSIFICATION OF THIS PAGE UNCLASSIFIED	19. SECURITY CLASSIFICATION OF ABSTRACT UNCLASSIFIED	20. LIMITATION OF ABSTRACT UL